

A SIMPLE AND ACCURATE NETWORK FOR HYDROGEN AND CARBON CHEMISTRY IN THE INTERSTELLAR MEDIUM

MUNAN GONG¹, EVE C. OSTRIKER¹ AND MARK G. WOLFIRE²

Published in ApJ

ABSTRACT

Chemistry plays an important role in the interstellar medium (ISM), regulating the heating and cooling of the gas and determining abundances of molecular species that trace gas properties in observations. Although solving the time-dependent equations is necessary for accurate abundances and temperature in the dynamic ISM, a full chemical network is too computationally expensive to incorporate in numerical simulations. In this paper, we propose a new simplified chemical network for hydrogen and carbon chemistry in the atomic and molecular ISM. We compare results from our chemical network in detail with results from a full photodissociation region (PDR) code, and also with the Nelson & Langer (1999) (NL99) network previously adopted in the simulation literature. We show that our chemical network gives similar results to the PDR code in the equilibrium abundances of all species over a wide range of densities, temperature, and metallicities, whereas the NL99 network shows significant disagreement. Applying our network in 1D models, we find that the CO-dominated regime delimits the coldest gas and that the corresponding temperature tracks the cosmic-ray ionization rate in molecular clouds. We provide a simple fit for the locus of CO-dominated regions as a function of gas density and column. We also compare with observations of diffuse and translucent clouds. We find that the CO, CH_x and OH_x abundances are consistent with equilibrium predictions for densities $n = 100\text{--}1000\text{ cm}^{-3}$, but the predicted equilibrium C abundance is higher than observations, signaling the potential importance of non-equilibrium/dynamical effects.

1. INTRODUCTION

Chemistry plays a key role in the interstellar medium (ISM) and star formation. In the ISM, a range of chemical species acts as agents for heating and cooling of the gas, regulating the gas temperature. Specific atomic and molecular species provide observational tracers for the gas physical properties, such as density and temperature. One of the most important molecules in the ISM is carbon monoxide (CO). CO is a main coolant for most of the molecular ISM via its rotational transitions (Goldsmith & Langer 1978; Neufeld & Kaufman 1993; Neufeld et al. 1995; Omukai et al. 2010), and also widely used as an observational tracer for molecular hydrogen (H₂) and star forming regions in both our Milky Way and other galaxies (e.g., Bolatto et al. 2008; Leroy et al. 2008; Roman-Duval et al. 2010; Saintonge et al. 2011a; Kenicutt & Evans 2012; Tacconi et al. 2013; Bolatto et al. 2013; Dobbs et al. 2014; Heyer & Dame 2015). Cooling by CO enables gas to reach low temperatures at which it collapses gravitationally to form stars. In return, feedback from star formation affects the chemical state of the ISM, as far-ultraviolet (FUV) radiation from massive stars dissociates and ionizes the gas. In particular, photodissociation of CO produces C, and ionization of C produces C⁺, with their fine structure lines among the most important coolants of atomic gas (Wolfire et al. 1995, 2003). The turbulence generated by supernova explosions leads to mixing of the gas composition and also changes the gas density distribution.

Traditionally, steady-state 1D photodissociation region (PDR) models with complex chemical networks have been used intensively to understand the detailed chemical structure of the ISM (e.g., Kaufman et al. 1999; Le Petit et al. 2006; Röllig et al. 2007; Wolfire et al. 2008, 2010; Hollenbach et al. 2012). Although much progress has been made using PDR models, solving the time-dependent equations is necessary for accurate abundances and temperature in the dynamic ISM. Typical star forming giant molecular clouds (GMCs) are not in chemical equilibrium (Leung et al. 1984; Papadopoulos et al. 2004), and are pervaded by supersonic turbulence that creates complex internal structure on dynamical timescales comparable to chemical timescales (Mac Low & Klessen 2004; Glover et al. 2010). In recent years, efforts have therefore been increasing to incorporate time-dependent chemistry within both local (Walch et al. 2015; Girichidis et al. 2016) and global (Richings & Schaye 2016a,b) galactic hydrodynamic and magnetohydrodynamic numerical simulations of the ISM. However, the full chemical network used in PDR models is too computationally expensive to incorporate in large numerical simulations. Modeling the chemical evolution of a group of N_{spec} species requires solving coupled ordinary differential equations (ODEs) of N_{spec} dimensions. Because the chemical timescales in the reaction set have extreme variation, the set of ODEs is usually very stiff and has to be solved implicitly, which results in a computational cost scaling as N_{spec}^3 .

For this reason, various authors have proposed approximations to simplify the chemical network for gas in star-forming regions (Nelson & Langer 1997, 1999; Keto & Caselli 2008; Glover et al. 2010; Richings et al. 2014). The general approach is to reduce the number of species,

¹Department of Astrophysical Sciences, Princeton University, Princeton, New Jersey 08544, USA; munan@princeton.edu, eco@astro.princeton.edu

²Department of Astronomy, University of Maryland, College Park, MD 20742-2421, USA; mwolfire@astro.umd.edu

retaining only hydrogen and the most important species for cooling and observation, such as C^+ , C , and CO . The number of reactions can also be reduced by capturing just the most important formation and destruction pathways for these species. Glover & Clark (2012a) compared a number of simplified networks by looking at the C^+ , C , CO , and temperature distributions in 3D simulations of turbulent molecular clouds. They found that all of the models they explored give similar results for density and temperature distributions, suggesting the gas thermodynamics is not very sensitive to the detailed chemistry. The CO distribution, however, is very different in various networks. They concluded that the simplified network of Nelson & Langer (1999, hereafter NL99) reproduces the CO abundance in more complicated models of Glover et al. (2010), and therefore recommend the NL99 network for simulating CO formation.

However, there are several limitations to the work of Glover & Clark (2012a). They did not carry out a detailed comparison between the different networks and more complex PDR models. Moreover, the comparisons they made are only under limited physical conditions. Notably, they used a cosmic-ray ionization rate $\xi_H = 10^{-17} \text{ s}^{-1} \text{ H}^{-1}$, which is an order of magnitude lower than the recent estimates from observations of Milky Way molecular clouds, $\xi_H \approx 2 \times 10^{-16} \text{ s}^{-1} \text{ H}^{-1}$ (Indriolo et al. 2007; Hollenbach et al. 2012). We show that when using the realistic cosmic-ray ionization rate, the NL99 network significantly underproduces CO compared to observations (see Section 3).

In this paper, we propose a new lightweight and accurate chemical network for following carbon and hydrogen chemistry in simulations of the atomic and molecular ISM. In Section 2, we describe our chemical network (which is an extension of NL99), related heating and cooling processes, and numerical methods. Then we carry out detailed comparison with both a PDR code and the original NL99 network in Section 3. Finally, in Section 4, we apply our network to simple 1D cloud models, and show the results from these applications in comparison to observations.

2. THE CHEMICAL MODEL

2.1. Chemical Reaction Network

2.1.1. General Framework

The chemical network in this paper is listed in in Tables 1 and 2, and described in detail in Appendix A. Our chemical network is based on the NL99 network in Nelson & Langer (1999) and Glover & Clark (2012a), with significant modification and extension. Eighteen species are considered: H , H_2 , H^+ , H_2^+ , H_3^+ , He , He^+ , O , O^+ , C , C^+ , CO , HCO^+ , Si , Si^+ , e , CH_x and OH_x . Following NL99, CH_x (including CH , CH_2 , CH^+ , CH_2^+ , CH_3^+) and OH_x (including OH , H_2O , OH^+ , H_2O^+ , H_3O^+) are pseudo-species, and their treatment is described in Appendix A.2 and A.3. Among the 18 species in our network, 12 of them are independently calculated, and 6 of them, H , He , C , O , Si and e , are derived from conservation of total hydrogen, helium, carbon, oxygen, and silicon nuclei, and the conservation of total charge.³ The

gas-phase abundances of total helium nuclei are $x_{He,tot} = n_{He,tot}/n = 0.1$. The gas-phase abundance of total carbon, oxygen, and silicon nuclei are assumed to be proportional to the gas metallicity relative to the solar neighborhood Z_g , and we adopt the values $x_{C,tot} = 1.6 \times 10^{-4} Z_g$ (Sofia et al. 2004), $x_{O,tot} = 3.2 \times 10^{-4} Z_g$ (Savage & Sembach 1996), and $x_{Si,tot} = 1.7 \times 10^{-6} Z_g$ (Cardelli et al. 1994). We do not explicitly follow the evolution of dust grains, but instead assume that the grain-assisted reaction rates scale with the dust abundance relative to the solar neighborhood Z_d . We assume the gas metallicity Z_g and dust abundance Z_d vary simultaneously, and use a single parameter for metallicity relative to the solar neighborhood,

$$Z = Z_g = Z_d. \quad (1)$$

We have updated all reaction rates in the original NL99 network, according to the most recent values in the UMIST (McElroy et al. 2013) and KIDA (Wakelam et al. 2010) catalogs, and other references in Tables 1 and 2. Notably, we have a higher rate of $C^+ + OH \rightarrow CO^+ + H$, and a higher rate of $C^+ + e \rightarrow C$ by including both radiative and dielectronic recombination. These higher rates lower the electron abundance and aid the formation of OH_x and HCO^+ , resulting in more efficient CO formation.

We have also modified and extended the NL99 network, as described in detail in Appendix A.1. One important extension is the addition of grain-assisted recombination of C^+ and He^+ . Although Glover & Clark (2012a) concluded these grain reactions do not affect CO formation at the low cosmic-ray ionization rate $\xi_H = 10^{-17} \text{ s}^{-1} \text{ H}^{-1}$, we found that with the updated cosmic-ray ionization rate $\xi_H = 2 \times 10^{-16} \text{ s}^{-1} \text{ H}^{-1}$ (Indriolo et al. 2007, 2015), these reactions are critical for CO formation at moderate densities $n \lesssim 1000 \text{ cm}^{-3}$. This is because electrons formed by cosmic-ray ionization inhibit CO formation, while He^+ ions formed by cosmic rays destroy CO (Bisbas et al. 2015). Grain-assisted recombination reduces the abundance of e and He^+ . With these extensions, we have 50 reactions in total, including collisional reactions, grain-assisted recombination and H_2 formation, photodissociation by FUV radiation, and cosmic-ray ionization.

2.1.2. Photochemistry

The photodissociation reactions induced by FUV depend on the radiation field strength. We assume that the incident radiation field scales with the standard interstellar radiation field determined by Draine (1978), using the parameter χ as the field strength relative to $J_{FUV} = 2.7 \times 10^{-3} \text{ erg cm}^{-2} \text{ s}^{-1}$ ($G_0 = 1.7$ in Habing (1968) units). The photochemistry reaction rates appropriate for this radiation field are listed in Table 2.

In optically thick regions, the radiation is attenuated by dust and by molecular line shielding. In a plane-parallel slab geometry with beamed incident radiation

equations, and found the results are the same. When calculating the abundance of H , C , O , and e from conservation laws, we assume all CH_x and OH_x are in the form of CH and OH . Because the abundance of CH_x and OH_x is usually very small compared to the hydrogen in H or H_2 , carbon in C , C^+ or CO , oxygen in O , and electrons provided by H^+ or C^+ , this assumption has no significant effect on the chemical network.

³ We have compared the approach of using conservation laws with directly calculating the abundance of all species from rate

field from one direction, the photodissociation rates of optically thick regions R_{thick} can be related to the rates in optically thin regions R_{thin} by

$$R_{\text{thick}} = \chi R_{\text{thin}} f_{\text{shield}} = \chi R_{\text{thin}} f_{\text{dust}} f_s, \quad (2)$$

where $f_{\text{dust}} = \exp(-\gamma A_V)$ is the dust-shielding factor and f_s is the self-shielding of C, CO and H_2 (see text below). The values of the parameter γ appropriate for the different reactions are listed in Table 2. The visual extinction A_V is calculated as

$$A_V = \frac{N Z_d}{1.87 \times 10^{21} \text{cm}^{-2}}, \quad (3)$$

where $N = N_{\text{H}} + 2N_{\text{H}_2}$ is the total hydrogen column density along the line of sight. This corresponds to $R_V \equiv A_V/E(B-V) = 3.1$ and $N/E(B-V) = 5.8 \times 10^{21} \text{cm}^{-2}$, appropriate for the diffuse ISM (Bohlin et al. 1978). In clouds with slab geometry and isotropic radiation field impinging from one side (Section 4), f_{shield} is an average value calculated from different incident angles. For more general, non-slab geometry, photo rates at a given location would be calculated by angle averages of Equation (2), as both χ and f_{shield} vary with direction.

For photoelectric heating on dust (see Section 2.2), the heating rate depend on the radiation field strength between 6 – 13.6 eV which affects the charge states of grains. For radiation in the FUV important for the photoelectric effect, we use a constant dust cross-section $\sigma_{\text{d,PE}} = 10^{-21} Z_d \text{cm}^2 \text{H}^{-1} = 1.87 A_V/N$ to calculate the attenuation by dust,

$$\chi_{\text{PE}}(N) = \chi f_{\text{dust,PE}} = \chi \exp(-\sigma_{\text{d,PE}} N); \quad (4)$$

our adopted cross-section is close to the value $1.8 A_V/N$ used in previous PDR models.

In addition to dust shielding, we also include the H_2 self-shielding, CO self-shielding, C self-shielding, and shielding by H_2 of CO and C. The photodissociation rate of H_2 can be written as

$$R_{\text{thick,H}_2} = \chi R_{\text{thin,H}_2} f_{\text{dust}} f_{s,\text{H}_2}(N_{\text{H}_2}). \quad (5)$$

We use the results in Draine & Bertoldi (1996) for H_2 self-shielding:

$$f_{s,\text{H}_2}(N_{\text{H}_2}) = \frac{0.965}{(1 + x/b_5)^2} \quad (6)$$

$$+ \frac{0.035}{(1 + x)^{0.5}} \exp[-8.5 \times 10^{-4} (1 + x)^{0.5}], \quad (7)$$

where $x \equiv N_{\text{H}_2}/(5 \times 10^{14} \text{cm}^{-2})$ and $b_5 = b/(\text{km/s})$ for b the velocity dispersion. In regions where $2x(\text{H}_2) = 2n(\text{H}_2)/n \gtrsim 0.1$, the self-shielding of H_2 is in the wings of the line profile, and the H_2 fraction is not sensitive to the choice of b_5 . Here we use a constant value $b_5 = 3$.

Similarly, the photodissociation rate of CO can be written as

$$R_{\text{thick,CO}} = \chi R_{\text{thin,CO}} f_{\text{dust}} f_{s,\text{CO}}(N_{\text{CO}}, N_{\text{H}_2}). \quad (8)$$

The shielding factor $f_{s,\text{CO}}(N_{\text{CO}}, N_{\text{H}_2})$ is interpolated from Table 5 in Visser et al. (2009) for a given column density of CO and H_2 . This accounts for both the CO self-shielding and the shielding of CO by H_2 . In Visser et al. (2009) Table 5, the velocity dispersion of CO is

assumed to be $b(\text{CO}) = 0.3 \text{km/s}^4$, the excitation temperature $T_{\text{ex}}(\text{CO}) = 5 \text{K}$ and $N(^{12}\text{CO})/N(^{13}\text{CO}) = 69$.

Lastly, the photodissociation rate of C is

$$R_{\text{thick,C}} = \chi R_{\text{thin,C}} f_{\text{dust}} f_{s,\text{C}}(N_{\text{C}}, N_{\text{H}_2}). \quad (9)$$

We adopt the treatment in Tielens & Hollenbach (1985). The shielding factor $f_{s,\text{C}}(N_{\text{C}}, N_{\text{H}_2}) = \exp(-\tau_{\text{C}}) f_{s,\text{C}}(\text{H}_2)$, where $\tau_{\text{C}} = 1.6 \times 10^{-17} N_{\text{C}}/\text{cm}^{-2}$, $f_{s,\text{C}}(\text{H}_2) = \exp(-r_{\text{H}_2})/(1 + r_{\text{H}_2})$, and $r_{\text{H}_2} = 2.8 \times 10^{-22} N_{\text{H}_2}/\text{cm}^{-2}$.

2.2. Heating and Cooling Processes

The heating and cooling processes included in our models are listed in Table 3, and described in detail in Appendix B. Here we describe the general processes we considered. The time rate of change of the gas thermal energy per H nucleus $e_{\text{g,sp}}$ is given by

$$\frac{de_{\text{g,sp}}}{dt} = \Gamma_{\text{tot}} - \Lambda_{\text{tot}}. \quad (10)$$

The total heating rate per H nucleus is

$$\Gamma_{\text{tot}} = \Gamma_{\text{PE}} + \Gamma_{\text{CR}} + \Gamma_{\text{H}_2\text{gr}} + \Gamma_{\text{H}_2\text{pump}} + \Gamma_{\text{H}_2\text{diss}}, \quad (11)$$

where Γ_{PE} is the heating from the photoelectric effect on dust, Γ_{CR} the cosmic-ray heating, $\Gamma_{\text{H}_2\text{gr}}$ the heating from H_2 formation on dust grains, $\Gamma_{\text{H}_2\text{pump}}$ the heating from H_2 UV pumping, and $\Gamma_{\text{H}_2\text{diss}}$ the heating from H_2 photodissociation. For typical environments in the cold atomic and molecular ISM, the photoelectric heating dominates at $A_V \lesssim 1$ and the cosmic-ray heating dominates at $A_V \gtrsim 1$.

The total cooling rate per H nucleus is

$$\Lambda_{\text{tot}} = \Lambda_{\text{line}} + \Lambda_{\text{dust}} + \Lambda_{\text{rec}} + \Lambda_{\text{H}_2\text{coll}} + \Lambda_{\text{Hion}}, \quad (12)$$

where Λ_{line} is the line cooling by atomic and molecular species, Λ_{dust} the cooling from gas-grain collisions, Λ_{rec} the cooling by electron recombination on dust grain, $\Lambda_{\text{H}_2\text{coll}}$ the cooling by collisional dissociation of H_2 , and Λ_{Hion} the cooling by collisional ionization of H. The line cooling dominates in typical atomic and diffuse molecular ISM where the gas densities are not high enough for dust cooling to be important ($n \lesssim 10^6 \text{cm}^{-3}$). We include line cooling of O, C, C^+ fine structure lines, the $\text{Ly}\alpha$ line of H, CO rotational lines, and the H_2 vibration and rotational lines.

The gas temperature is related to the gas energy by (Krumholz 2014)

$$T = \frac{e_{\text{g,sp}}}{c_{v,\text{H}}}. \quad (13)$$

The specific heat at constant volume $c_{v,\text{H}} = \frac{1}{2} k_B f$, where $k_B = 1.381 \times 10^{-16} \text{erg K}^{-1}$ is the Boltzmann constant and $f = \sum f_s x_s$ is the degree of freedom in all species per H nucleus. For H, He, He^+ , H^+ , and e, $f_s = 3$ from translational degrees of freedom. For H_2 , the excitation temperature for rotational and vibrational levels are $\theta_{\text{rot}} = 170.6 \text{K}$ and $\theta_{\text{vib}} = 5984 \text{K}$ (Tomida et al. 2013). Assuming a fixed ortho-to-para ratio of H_2 , the rotational and vibrational heat capacities of H_2 are very small at typical molecular cloud temperatures $T \lesssim 50 \text{K}$.

⁴ We have also tried to use the $b(\text{CO}) = 3 \text{km/s}$ results in Visser et al. (2009), and found that $f_{s,\text{CO}}$ changes within $\sim 50\%$, and the CO fraction is not sensitive to $b(\text{CO})$.

Therefore, we ignore the contribution of rotational and vibrational levels of H_2 to the specific heat, and simply use

$$c_{v,\text{H}} = \frac{3}{2}k_B(x_{\text{H}} + x_{\text{H}_2} + x_{\text{H}^+} + x_{\text{He}} + x_{\text{He}^+} + x_{\text{e}}) \quad (14)$$

$$= \frac{3}{2}k_B[(1 - x_{\text{H}_2}) + x_{\text{He,tot}} + x_{\text{e}}]. \quad (15)$$

2.3. Numerical Method

We consider a simple one-dimensional slab model with uniform density n , and FUV radiation incident from one side of the slab, similar to typical 1D PDR (photodissociation region) models. The incident radiation field is expected to be relatively isotropic over 2π steradians. In Section 3, we use the approach of Wolfire et al. (2010) in order to compare with their PDR code: the isotropic radiation field is approximated by assuming a unidirectional flux incident at an angle of 60° to the normal of the slab surface. Thus, with the incident radiation field strength χ , the field strength at the perpendicular column density N from the slab surface will be $\chi_{\text{eff}} = (\chi/2)f_{\text{shield}}(2N)$, where the factor $1/2$ in χ comes from the one-sided slab and the factor 2 in N comes from the angle of 60° . In Section 4, we directly calculate the isotropic radiation field strength by averaging over the incident angles.

In each model, we divide a slab into 10^3 logarithmically spaced grid zones in the range of $N = 10^{17}/Z - 10^{22}/Z \text{ cm}^{-2}$. In each zone, walking inward from the lowest N to the highest N in order, we calculate the equilibrium chemistry and temperature. This is because the chemical states of all exterior zones are needed to calculate the radiation field shielding factor for the next zone.

The evolution of abundances of chemical species $x_s = n_s/n$ is determined by a set of chemical reactions:

$$\begin{aligned} \frac{dx_s}{dt} = & \sum_{i,j} (\pm k_{2\text{body},s}^{ij} n x_i x_j) + \sum_i (\pm k_{\text{gr},s}^i n x_i) \\ & + \sum_i (\pm k_{\text{cr},s}^i x_i) + \sum_i (\pm k_{\gamma,s}^i x_i). \end{aligned} \quad (16)$$

Here $k_{2\text{body},s}^{ij}$, $k_{\text{gr},s}^i$, $k_{\text{cr},s}^i$, and $k_{\gamma,s}^i$ are the rates for the two-body, grain surface, cosmic-ray and photodissociation reactions listed in Tables 1 and 2 that have species s either as a reactant or product. x_i and x_j are the abundance of the corresponding reactant species, and the sign is negative if x_s is a reactant of the chemical reaction and positive if x_s is a product. The chemical reactions in Equation (16) and the energy evolution in Equation (10) give a coupled ODE (ordinary differential equation) system of 13 variables (12 independently calculated species and 1 energy equation). The derived species (H, He, C, O, Si, and e) are not directly calculated from Equation 16, but from the conservation of atomic nuclei and charge. To efficiently solve this set of stiff ODEs, we use the open-source CVODE package (Cohen et al. 1996), which adopts a method of implicit backward differentiation formulas.

3. CODE TEST AND COMPARISON

In this section, we test the agreement between the greatly simplified chemical network in this paper and a PDR code with much more sophisticated chemistry and radiation transfer. We also compare with the widely used original NL99 network and point out the importance of our modifications.

The PDR code used here is derived from the Tielens & Hollenbach (1985) PDR code, which has been in continuous use, and updated and maintained since its original inception. The model has been used extensively to analyze observations in a diverse set of environments including the diffuse ISM (e.g., Wolfire et al. 2003, 2008; Sonnentrucker et al. 2015), low-mass molecular clouds (Lee et al. 2014; Burton et al. 2015), Galactic GMCs (Wolfire et al. 2010), intense Galactic PDRs (Sheffer et al. 2011), and extragalactic PDRs (e.g., Kaufman et al. 2006; Stacey et al. 2010). Recent updates to the chemistry, heating, and cooling rates are given in Wolfire et al. (2010), Hollenbach et al. (2012) and Neufeld & Wolfire (2016). The code calculates the thermal balance temperature and steady-state abundances of 74 species using 322 reactions. The dominant gas-phase species are H, He, C, O, H_2 , O_2 , OH, CO, H_2O , e^- , H^+ , He^+ , C^+ , O^+ , OH^+ , CO^+ , H_2O^+ , HCO^+ , H_3O^+ , H_2^+ , H_3^+ , CH^+ , CH_2^+ , CH_3^+ , CH, CH_2 , CH_3 , CH_4 , Mg, Mg^+ , Si, Si^+ , SiH_2^+ , SiH, SiO, Fe, Fe^+ , S, S^+ , SiO^+ , SO^+ , HOSi^+ , H_2^* , H^- , PAH $^-$, PAH, and PAH $^+$. Also included are fluorine and chlorine chemistry as in Neufeld & Wolfire (2009). Freeze-out of atoms and molecules on grains (such as CO and H_2O) and grain surface reactions such as OH and H_2O formation are included as in Hollenbach et al. (2009, 2012) but are turned off for most of the comparisons in this paper. The effects of grain surface reactions on chemistry are discussed in Appendix C.5. For comparison to the results presented in this paper, we use a modified version of the code in which the geometry is plane parallel and the density is constant. In addition, we use the photoionization, photodissociation, and cosmic-ray induced photodissociation rates from Heays et al. (2017), consistent with Tables 1 and 2 in this paper. We use the approximation in Wolfire et al. (2010) for an isotropically incident radiation field assuming a single ray incident at 60° to the normal and use the H_2 self-shielding treatment as in Tielens & Hollenbach (1985).

The NL99 network we compare with is similar to that used in Glover & Clark (2012a). It is based on two main parts: the CO chemistry in NL99, and the hydrogen chemistry in Glover & Mac Low (2007). In order to make a meaningful comparison of the difference between the CO chemistry in this paper and the NL99 network, we updated all the reaction rates in the NL99 network to the values in this paper (see Tables 1 and 2), and adopted the same gas-phase atomic abundances of carbon and oxygen. We have also added the H_3^+ destruction channel $\text{H}_3^+ + \text{e} \rightarrow 3\text{H}$ in addition to the reaction $\text{H}_3^+ + \text{e} \rightarrow \text{H}_2 + \text{H}$ in Nelson & Langer (1999), to have the hydrogen chemistry consistent with that used in Glover et al. (2010) and this work.⁵

We run slab models described in Section 2.3 with den-

⁵ Caution needs to be taken here: if the H_3^+ destruction channel $\text{H}_3^+ + \text{e} \rightarrow 3\text{H}$ is not included, the artificially elevated H_3^+ abundance would cause CO to form much more efficiently than it should.

sities $n = 50 - 1000 \text{ cm}^{-3}$, and ambient radiation field $\chi = 1$. We compare the results based on the NL99 network (as described above) with those from our chemical network. We similarly run the PDR code, and compare results, using the same configurations of density and incident radiation field. Here we focus on the comparison of the chemistry network and fix the temperature at $T = 20 \text{ K}$ and metallicity $Z = 1$. We have also made comparisons with the PDR code at $Z = 0.1$, and by solving the chemistry and temperature simultaneously. The detailed results are shown in Appendix C.3 and C.2. The treatment of grain-assisted recombinations in the PDR code is based on the results in Wolfire et al. (2008), and is slightly different from the rate in Weingartner & Draine (2001a) that we adopted. Thus, for the purpose of comparison, we multiply the rates of reactions 2-5 in Table 2 by a factor of 0.6 in our models to match the rates in the PDR code. For further discussions of the grain-assisted recombination rates, see Appendix C.4. We use the recent measurement of the primary cosmic-ray ionization rate per hydrogen $\xi_{\text{H}} = 2 \times 10^{-16} \text{ s}^{-1} \text{ H}^{-1}$ (Indriolo et al. 2007) if not specified otherwise. We also run some fixed temperature models with the low cosmic-ray ionization rate $\xi_{\text{H}} = 10^{-17} \text{ s}^{-1} \text{ H}^{-1}$, in order to compare with results from the previous literature that adopted this rate (e.g. Glover & Clark 2012a).

In our models, from the edge of the slab to the inside, the FUV radiation field is attenuated by both dust and molecular lines. As N and A_V increases, the abundance of molecular hydrogen increases due to H_2 self-shielding, while the atomic hydrogen abundance decreases. The C^+ abundance decreases due to dust shielding, with most carbon in C at intermediate A_V . Above $A_V \sim 1$, cosmic-ray ionization of H_2 creates H_3^+ , which reacts with C and O to form CH_x and OH_x molecules. CH_x and OH_x molecules further mediate the formation of CO.

Figure 1 illustrates the locations of the H to H_2 , C^+ to C, and C to CO transitions in the N - n plane. In panel (a) of Figure 1, we show that there is a very good agreement on the location of the C^+ to C transition between our chemical network and the PDR code (yellow solid and dashed lines). There are some differences in the location of C to CO transitions (magenta solid and dashed lines), but the detailed abundance and column of CO agrees within a factor of ~ 2 at a given A_V (see Figures 2 and 4, and discussions below). The NL99 network, however, yields both C^+ to C and C to CO transitions at a significant higher A_V (yellow and magenta dotted lines). Especially at $n \lesssim 500 \text{ cm}^{-3}$, the CO abundance in the NL99 network remains very low up to $A_V = 5$. This is inconsistent with observations of CO in diffuse molecular clouds with $n \lesssim 200 \text{ cm}^{-3}$, and $A_V \lesssim 1$ (Magnani et al. 1985; Burgh et al. 2007; Sheffer et al. 2008; Goldsmith 2013). The failure of the NL99 network here is mainly due to two reasons. Firstly and most importantly, the NL99 network does not include C^+ recombination on dust grains. Because the rate of C^+ recombination on dust grains is higher than the direct recombination with free electrons, the C^+ to C transition is pushed to higher A_V , and the C^+ abundance at $A_V = 1 - 5$ regions is elevated. This impedes CO formation: the electrons from C^+ destroy H_3^+ , which is an important reactant for the first step of CO formation. Second, the

NL99 network does not include He^+ recombination on dust grains, which is the main destruction channel for He^+ at solar metallicity. In well-shielded regions, the reaction $\text{He}^+ + \text{CO} \rightarrow \text{C}^+ + \text{O} + \text{He}$ is the main channel for CO destruction. Therefore, the elevated He^+ abundance also suppresses CO in the NL99 network (see also Figure 2 for H_3^+ and He^+ abundances). Without recombination of C^+ and He^+ on grains, the transition of C to CO in the NL99 network occurs at a quite high density, $n > 500 \text{ cm}^{-3}$.

The H to H_2 transition is the same in our network and the NL99 network, and shows very good agreement with the PDR code. The same H to H_2 transition in our network and the NL99 network is simply because the hydrogen chemistry in both networks are identical, and H_2 formation is largely unaffected by other species. Our results also show very good agreement with the analytic formula for the H to H_2 transition in Bialy & Sternberg (2016) (see their Equation (39)).

Panel (b) in Figure 1 shows an interesting comparison using the low cosmic-ray ionization rate $\xi_{\text{H}} = 10^{-17} \text{ s}^{-1} \text{ H}^{-1}$. With a low cosmic-ray rate, the location of the C to CO transition is similar in the NL99 network and our network. This is because with the low cosmic-ray rate, CO destruction by He^+ is less efficient due to the lower abundance of He^+ created by cosmic rays, and the CO abundance is now mainly limited by photodissociation. The dependence of the photodissociation rate on dust shielding determines the A_V at which CO forms. Although CO abundances are similar at $\xi_{\text{H}} = 10^{-17} \text{ s}^{-1} \text{ H}^{-1}$, there are significant differences in the abundances of other species such as C^+ between the NL99 network and our network (see Figure 3). Thus, the apparent similarity in the CO transition at the low cosmic-ray rate is deceptive. Using the low cosmic-ray ionization rate, Glover & Clark (2012a) compared the NL99 network with the larger Glover et al. (2010) network, considering the CO distribution in turbulent clouds. They reached the conclusion that the NL99 network is sufficiently accurate for simulating CO formation. However, here we show that with a more realistic cosmic-ray ionization rate, the NL99 network significantly underestimates the CO abundance, and the grain assisted recombinations of C^+ and He^+ are very important for obtaining correct CO abundances.

Figures 2 and 4 plot the abundances of different species as a function of A_V and N for the three networks at $\xi_{\text{H}} = 2 \times 10^{-16} \text{ s}^{-1} \text{ H}^{-1}$. Figure 2 shows the abundance comparisons for $\xi_{\text{H}} = 10^{-17} \text{ s}^{-1} \text{ H}^{-1}$. Overall, there is a very good agreement between our chemical network and the PDR code for C^+ , C, CO, and H_3^+ , which are the main observable species in our network. It is remarkable that our network also reproduces the column densities N_i at a given A_V of all other species with errors less than a factor of ~ 2 , even for the largely simplified pseudo-species OH_x and CH_x . This indicates that our simplified network successfully captures the main chemical pathways of these species. There are also some differences to be pointed out: Compared to the PDR code, the CO abundance is lower at $n = 100 \text{ cm}^{-3}$ and $A_V \gtrsim 2$, and higher at $A_V \sim 1$ in our network. This is partly due to the difference in the grain-assisted recombination rates, as discussed in Appendix C.4, and partly due to the ap-

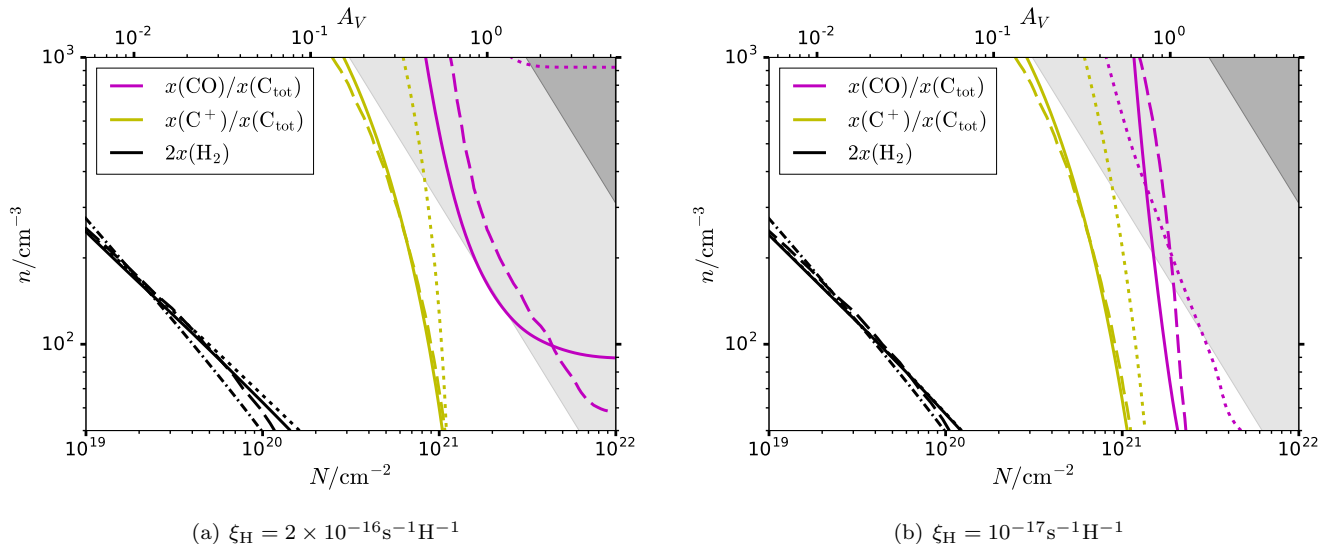


Figure 1. Contours showing locations of H to H₂, C⁺ to C, and C to CO transitions in the N - n plane. The magenta, yellow, and black lines are contours where $x_{\text{CO}}/x_{\text{C}_{\text{tot}}}$, $x_{\text{C}^+}/x_{\text{C}_{\text{tot}}}$, and $2x_{\text{H}_2}$ are respectively equal to 0.5. The solid, dashed and dotted lines are the results of the chemistry network in this paper, the PDR code, and the NL99 network, respectively. The black dashed-dotted line plots the analytic formula in Bialy & Sternberg (2016) for the H to H₂ transition. The left panel (a) is using cosmic-ray ionization rate $\xi_{\text{H}} = 2 \times 10^{-16} \text{s}^{-1} \text{H}^{-1}$ (Indriolo et al. 2007), and the right panel (b) is using the old low cosmic-ray ionization rate $\xi_{\text{H}} = 10^{-17} \text{s}^{-1} \text{H}^{-1}$. The gas temperature is fixed at $T = 20\text{K}$. The regions where the H₂ formation timescale is comparable to or shorter than the typical turbulence crossing timescale are shaded dark gray for $t_{\text{H}_2}/t_{\text{dyn}} < 1$ and light gray for $t_{\text{H}_2}/t_{\text{dyn}} < 10$ (see Equation (18)).

proximation of using pseudo-species OH_x, which does not capture all the details of OH_x formation and destruction. For similar reasons that lead to the difference in the CO abundance, there are also discrepancies in the abundances of other species such as C, He⁺, OH_x, and CH_x at $n = 100 \text{cm}^{-3}$ and $A_V \gtrsim 2$. However, since the differences mainly occur in a limited range of A_V , the differences in column density in Figure 4 are small.

The NL99 network, however, fails to reproduce the equilibrium abundances in the PDR code. The CO abundance is too low as a result of the high C⁺ and He⁺ abundances, as discussed above. The NL99 network also leads to a much higher CH_x abundance, due to the absence of the important destruction channel of CH reacting with H. Therefore, we conclude that our new chemical network is preferred over the NL99 network. With one additional species (O⁺) and nineteen additional reactions, we find that the increase in computational cost is about 50%.

To cross-check with other PDR codes, we have also run a comparison with the publicly available *PyPDR*⁶ code provided by Simon Bruderer. *PyPDR* has been shown to agree well with the PDR bench mark in Röllig et al. (2007), and therefore is a good point of comparison with the existing model literature. However, *PyPDR* does not include grain-assisted recombination of ions, which is important for CO formation as discussed above. Appendix C.6 shows that our chemical network (without grain assisted recombinations) agrees very well with the *PyPDR* code, which further validated our results.

4. SAMPLE APPLICATIONS

Observations of a wide range of galaxies show a correlation between the surface density of the star forma-

tion rate (SFR) and the surface density of molecular gas (e.g. Bigiel et al. 2008, 2011; Saintonge et al. 2011b; Genzel et al. 2010; Jameson et al. 2015). Although in some models it has been proposed that star formation is associated with gas that is shielded enough for H₂ to form (Krumholz et al. 2009), any relationship with H₂ would have to be coincidental rather than causal, because H₂ is not an active coolant in cold gas. In principle, H₂ might be important because it is a prerequisite for CO formation, and CO is the dominant coolant in the environment of star formation, at least when the metallicity is not extremely low (Glover & Clark 2012c). However, the cooling provided by C⁺ can also bring gas to quite low temperatures, so that it is able to collapse gravitationally at small scales (Glover & Clark 2012b). Thus, the association of star formation with the molecular phase may simply be because both chemical and dynamical timescales are shorter at higher density, and the shielding that limits photodissociation also limits photoheating (see also Krumholz et al. 2011).

Regardless of the reason for the correlation between molecular gas and star formation, quantifying the relationship between gas and star formation empirically requires tracers of all gas phases. Atomic gas is easily identified with the 21 cm transition, but H₂ is difficult to observe directly due to the high excitation temperature of its rotational levels. CO is often used as a tracer of H₂, but CO is known to be difficult to detect in metal-poor galaxies, and even when detected, the star formation rate per CO luminosity is much higher than that in the Milky Way-like galaxies (e.g. Taylor et al. 1998; Leroy et al. 2007; Schruba et al. 2011, 2012; Hunt et al. 2015). Moreover, CO is not necessarily a linear tracer of H₂ (Bolatto et al. 2013).

Here, we use simple slab models to explore the cor-

⁶ http://www.mpe.mpg.de/~simonbr/research_pypdr/index.html

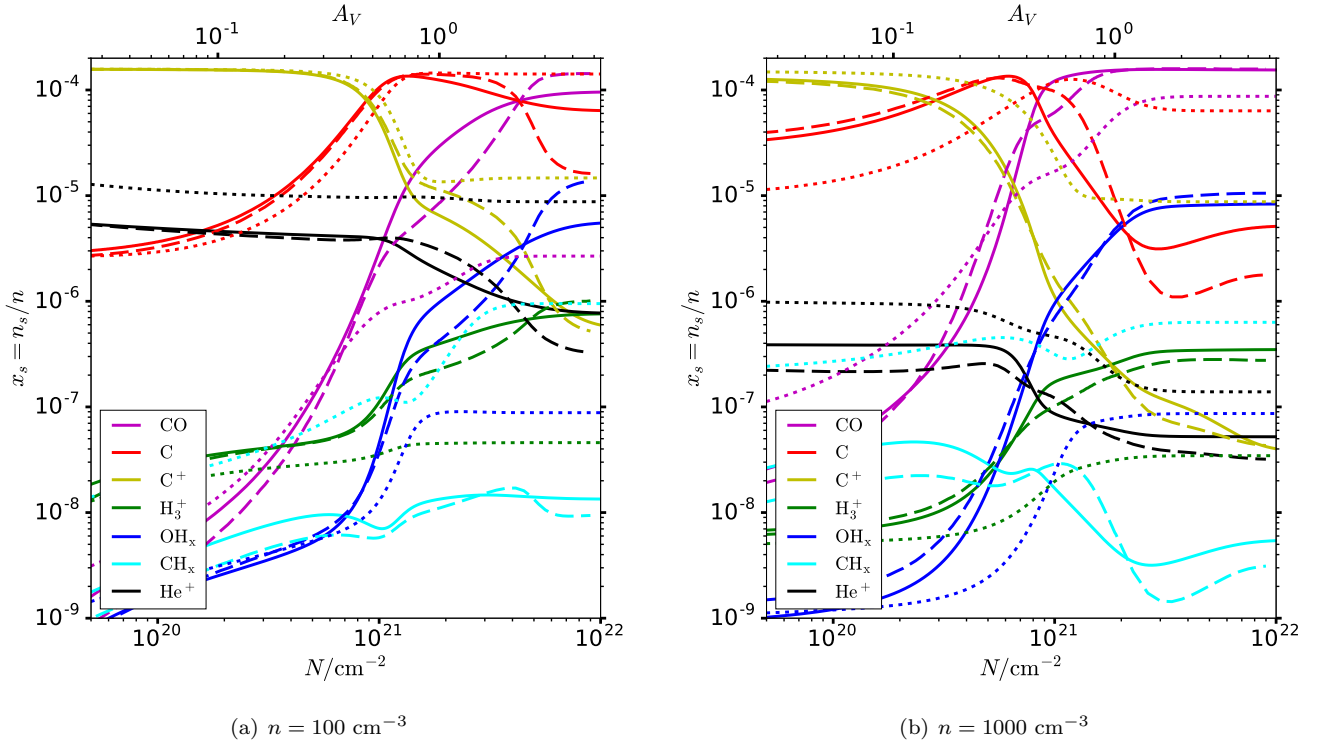


Figure 2. Abundances of different species as a function of A_V and N at densities $n = 100\text{cm}^{-3}$ in panel (a) and $n = 1000\text{cm}^{-3}$ in panel (b). The cosmic-ray ionization rate here is $\xi_H = 2 \times 10^{-16}\text{s}^{-1}\text{H}^{-1}$, corresponding to panel (a) of Figure 1. Gas temperature is fixed at $T = 20$ K. See also Figures 12 and 14 in Appendix C for abundances of all species at densities between $n = 50 - 1000\text{cm}^{-3}$. The abundances of different species $x_i = n_i/n$ are plotted in different colors: CO (magenta), C (red), C $^+$ (yellow), H $_3^+$ (green), OH $_x$ (blue), CH $_x$ (cyan), and He $^+$ (black). As in Figure 1, the solid, dashed and dotted lines respectively represent results of the chemistry network in this paper, the PDR code, and the NL99 network. Note that the NL99 network substantially underestimates the CO abundance at $n = 100\text{cm}^{-3}$, and overestimates the C $^+$ abundance (estimates of other species also fail in parts of parameter space). Overall, our network shows good agreement with the PDR code results.

relations between chemical state (especially $x(\text{CO})$ and $x(\text{H}_2)$) and temperature, while also exploring the dependence of both properties on n , N , χ , ξ_H and Z . We also explore the mean abundances of various species on average cloud density and column, and compare with observations.

4.1. CO as a Tracer of H $_2$ and Cold Gas

Following Krumholz et al. (2011), we investigate how well CO and H $_2$ trace cold gas in the ISM with different metallicities. Krumholz et al. (2011) used semi-analytic models to estimate the H $_2$ and CO abundances and separately computed the equilibrium temperature for gas cooled either by C $^+$ or by CO. Here, we instead use our chemical network and self-consistent cooling to solve for the equilibrium chemical composition and temperature of the gas. We run one-dimensional slab models described in Section 2.3 at a range of densities $n = 10^1 - 10^4\text{cm}^{-3}$, and compute the chemical and temperature state of the gas in the A_V - n plane. We also run models with different metallicities, incident radiation field, and cosmic-ray ionization rate to study the dependence of gas properties on these parameters.

It should be noted that in the realistic ISM, the timescales of cooling and chemical reactions are different, and the dynamical timescales set by turbulence may be shorter than these. Thus, the equilibrium chemi-

cal and thermal state does not necessarily apply in the real ISM. This is particularly an issue for H $_2$, because the formation time is $t_{\text{H}_2} \approx 10^7 \text{ yr } Z_d^{-1} \left(\frac{n}{100\text{cm}^{-3}}\right)^{-1}$ at $T = 100\text{K}$ (see line 24 in Table 1), whereas typical dynamical timescales in dense gas are (see Equation (B8))

$$t_{\text{dyn}} = L/v_{\text{turb}}(L) \sim 1\text{Myr } (L/\text{pc})^{1/2}. \quad (17)$$

For transient clouds produced by turbulent compression, even if the mean shielding column is sufficient for the equilibrium H $_2$ abundance to be high, the H $_2$ formation timescale may be longer than the cloud lifetime. For example, the criterion $t_{\text{H}_2} < t_{\text{dyn}}$ is equivalent to

$$Z_d^2 \left(\frac{n}{100 \text{ cm}^{-3}}\right) \left(\frac{N}{10^{21} \text{ cm}^{-2}}\right) > 31, \text{ or} \quad (18)$$

$$Z_d A_V \left(\frac{n}{100 \text{ cm}^{-3}}\right) > 17$$

which is well above the equilibrium H/H $_2$ transition in Figure 1.

In high column density self-gravitating clouds with supersonic turbulence, the mass-weighted density $\langle n \rangle_M$ is proportional to N^2 , $\langle n \rangle_M \propto N^2$ (See Equation (D11), where the second term dominates over the first term).

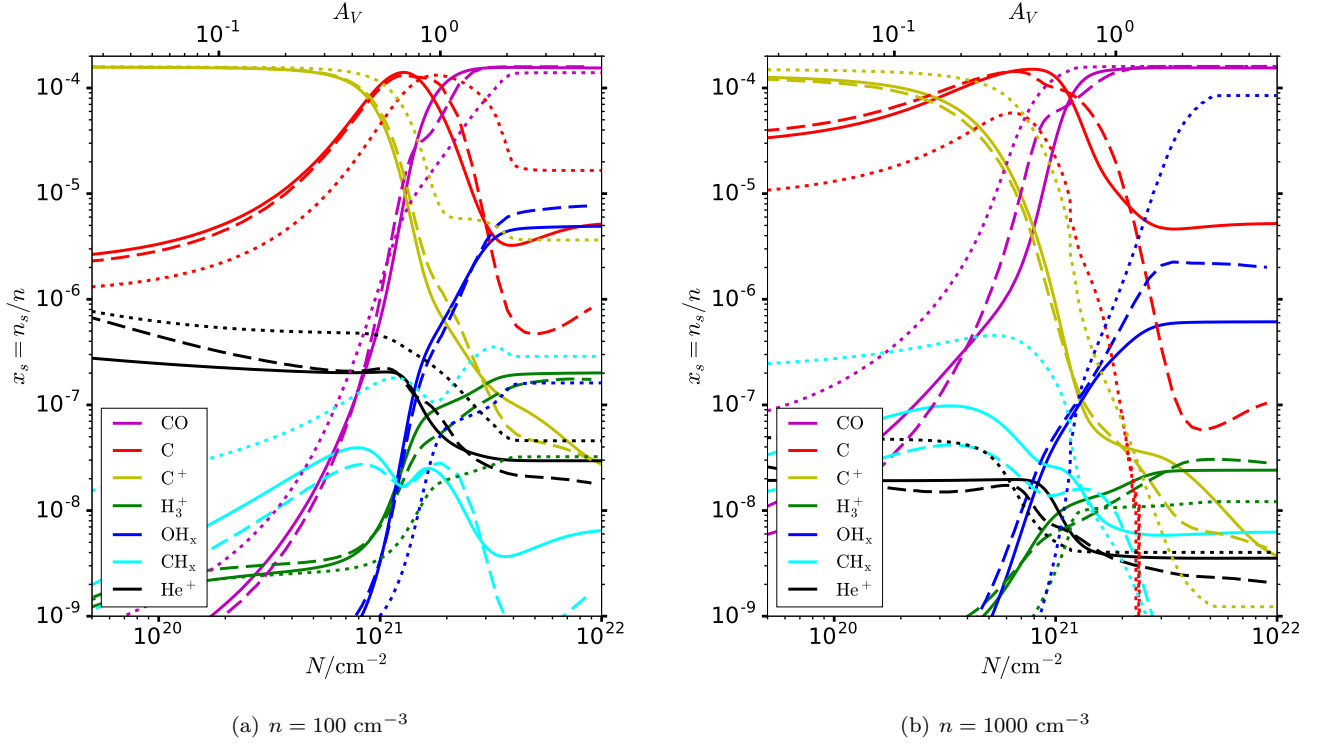


Figure 3. Similar to Figure 2, except with the low cosmic-ray ionization rate $\xi_{\text{H}} = 10^{-17} \text{s}^{-1} \text{H}^{-1}$, as in panel (b) of Figure 1. At a low cosmic-ray rate, the NL99 network results are more similar to ours, although in certain parts of parameter space there are still large discrepancies.

Combining this with Equation (18), gives

$$\begin{aligned} N &\gtrsim 4.3 \times 10^{21} Z_d^{-2/3} \text{ cm}^{-2}, \text{ or} \\ A_V &\gtrsim 2.3 Z_d^{-2/3} \end{aligned} \quad (19)$$

for $t_{\text{H}_2} < t_{\text{dyn}}$. Equation (19) suggests that for a molecular cloud with $A_V \gtrsim 1$, although molecular hydrogen is difficult to form at an average density $n \sim 100 \text{ cm}^{-3}$ (Equation (18)), turbulence can compress most of the gas to reach to a higher density regime and enable the cloud to become molecular in a shorter timescale.

For gravitationally bound clouds that live longer than several flow-crossing times, the dynamical cycling of gas to the unshielded surface may limit the molecular abundance. The timescale for a fluid element in the cloud to travel through the unshielded region is $t_{\text{sh}} = L_{\text{shield}}/v_{\text{turb}}(L_{\text{cloud}})$, where L_{shield} is the length scale for H_2 to be self-shielded against the FUV radiation. Using Equation (52) in Sternberg et al. (2014), and the H_2 formation rate on dust (see line 1 in Table 2), the

shielding length⁷

$$L_{\text{shield}} = \frac{N}{n} \approx 1 \text{ pc} \chi \left(\frac{n}{100 \text{ cm}^{-3}} \right)^{-2}, \quad (20)$$

where n is the average (volume-weighted) density of the cloud. Adopting $v_{\text{turb}}(L) \sim 1 \text{ km/s} (L/\text{pc})^{1/2}$, this yields:

$$t_{\text{sh}} = 0.2 \text{ Myr} \chi \left(\frac{n}{100 \text{ cm}^{-3}} \right)^{-2} \left(\frac{L_{\text{cloud}}}{10 \text{ pc}} \right)^{-1/2}. \quad (21)$$

The timescale for H_2 photodissociation is $t_{\text{diss}, \text{H}_2} = 1/k_{\text{diss}, \text{H}_2} = 6 \times 10^2 \text{ yr}$ (the photodissociation rate $k_{\text{diss}, \text{H}_2} = 5.6 \times 10^{-11} \text{ s}^{-1}$, see line 19 in Table 2). Setting $t_{\text{sh}} < t_{\text{diss}, \text{H}_2}$ gives

$$\frac{1}{\chi} \left(\frac{n}{100 \text{ cm}^{-3}} \right)^2 \left(\frac{L_{\text{cloud}}}{10 \text{ pc}} \right)^{1/2} > 3 \times 10^2; \quad (22)$$

when this condition is satisfied, molecules can avoid being destroyed by photodissociation over the timescale

⁷ This uses the approximation of $\ln(\alpha G/2 + 1) \approx \alpha G/2$ (see Equation (40) in Sternberg et al. (2014)). For the CNM in pressure equilibrium (Equation (23)), $\alpha G/2 \approx 1.3$, which makes the approximation good up to a factor of ~ 3 . At $\alpha G/2 \approx 1$, most of the H column is built up in atomic regions (see Figure 7 in Sternberg et al. (2014)), and therefore we calculate the shielding length by $L_{\text{shield}} = N/n$. Note, however, in the limit of $\alpha G/2 \gg 1$, i.e., for low density gas or highly illuminated PDR such as observed in Bialy et al. (2015), the dependence changes to $N \sim 2/\sigma_g \sim 10^{21} \text{ cm}^{-2}$, independent of αG , giving $L_{\text{shield}} \sim 3 \text{ pc} [n/(100 \text{ cm}^{-3})]^{-1}$.

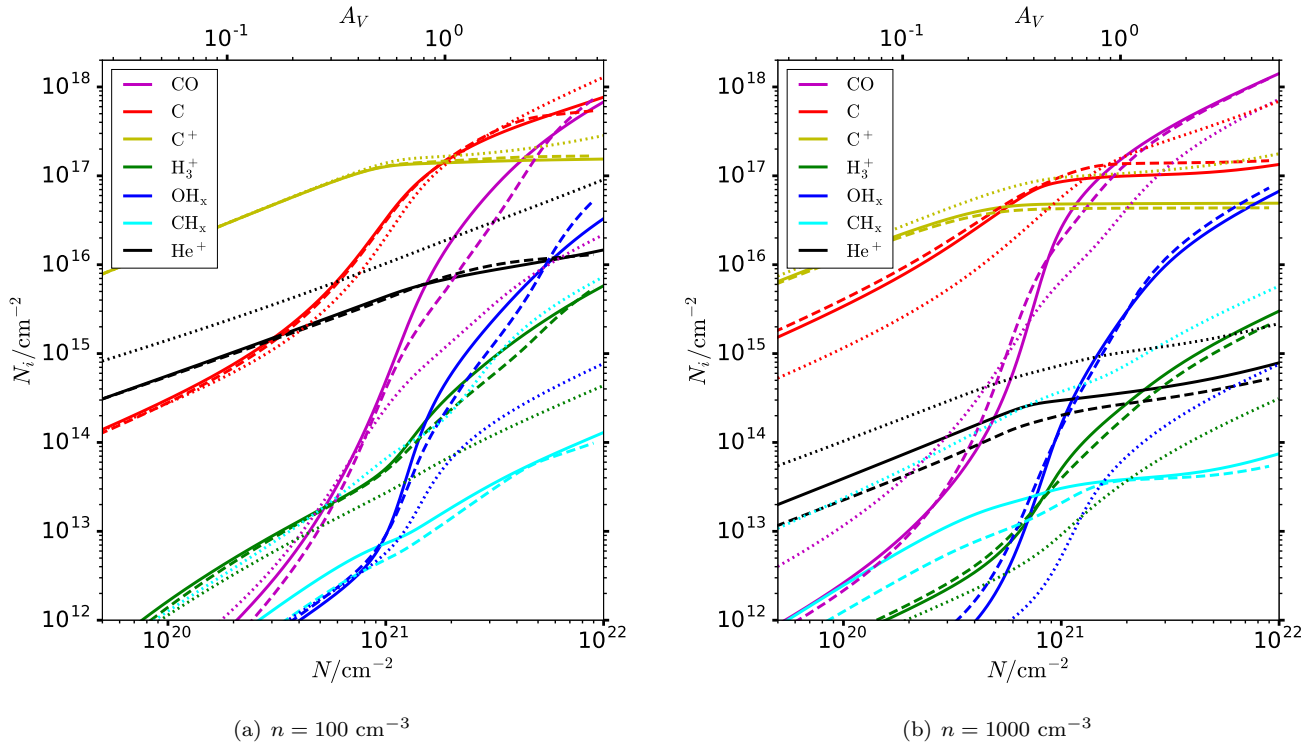


Figure 4. Integrated column density of different species N_i as a function of N_H and A_V , for our network, the PDR code, and the NL99 network. The colors and symbols are the same as in Figures 2. The cosmic-ray ionization rate here is $\xi_H = 2 \times 10^{-16} \text{s}^{-1} \text{H}^{-1}$. See also Figures 13 and 15 in Appendix C for all species at densities $n = 50 - 1000 \text{cm}^{-3}$.

to cross the unshielded surface of the cloud. For example, a cloud of size 10 pc will require its density $n > 1.7 \times 10^3 \text{cm}^{-3}$ to be fully molecular. Equation (22) shows that even in gravitationally bound clouds, the cycling of gas from the cloud interior to the surface can also limit the H_2 abundance in low density regimes. If the H_2 abundance is reduced by exposure to UV, other chemical pathways will also be strongly affected. Therefore, to fully investigate how well CO traces molecular gas, numerical simulations with time-dependent chemistry are needed. Still, we show that our simple models can provide insight into this important but complicated problem.

Figure 5 shows the equilibrium gas temperature in color scale, in comparison to the contours of equilibrium H_2 , CO, and C^+ abundances. Across a wide range of metallicities $Z = 0.2 - 1$, Figure 5 shows that gas that is mostly molecular is also at $T \lesssim 40\text{K}$. However, it is important to note that the coincidence of high H_2 abundance and low temperature is not causal. For gas in the range of Figure 5, most of the cooling is provided by C^+ , C, and CO. Even if we artificially turn off the formation of H_2 and CO, the gas can still be cooled to $T \sim 20\text{K}$ with C and C^+ cooling. We discuss this further in Section 4.3. At low metallicity, the minimum density required for gas to become molecular increases. This is because H_2 forms less efficiently when the dust abundance drops. At low enough n , the equilibrium $x(\text{H}_2)$ is low even in very shielded regions. This is due to the destruction of H_2 by cosmic rays. The gas temperature is similar at $A_V \lesssim 1$ across $Z = 0.2 - 1$, because both the photoelectric heat-

ing and gas cooling are proportional to Z . At $A_V \gtrsim 1$, and also in low density and low metallicity regions, the cosmic-ray heating dominates, which is independent of metallicity. This leads to an increase of the gas temperature in these regions at low metallicity due to decreased gas cooling.

At solar metallicity ($Z = 1$), Figure 5 shows that the region of high CO abundance (where CO line cooling dominates) traces the lowest temperature $T \lesssim 20\text{K}$ gas very well⁸. At very low metallicities, there is less dust shielding and collisional reactions between metal species occur at a reduced rate, leading to less efficient CO formation, and CO traces the temperature less well.

4.2. Dependence on χ , ξ_H , and Z

Figure 6 (a) shows that an increase of χ pushes the H_2 -dominated region to higher A_V , and that even H_2 dominated gas can be at $T > 100\text{K}$ if χ is large enough. Increasing the cosmic-ray rate requires higher density for the gas to become H_2 -dominated, because cosmic rays can dissociate H_2 (Figure 6 (b)).

An increase (decrease) of χ moves the boundary of CO-dominated gas to higher (lower) A_V , because CO only forms in dust-shielded regions (Figure 6 (a)). Similarly, an increase (decrease) of ξ_H pushes the minimum density for CO up (down), because He^+ and C^+ formed in cosmic-ray reactions are harmful for CO formation (Figure 6 (b)). However, in both Figure 6 (a) and Fig-

⁸ However, there is a subtlety in this: even if we artificially force CO not to form, C would have cooled the gas to similarly low temperatures (see Section 4.3).

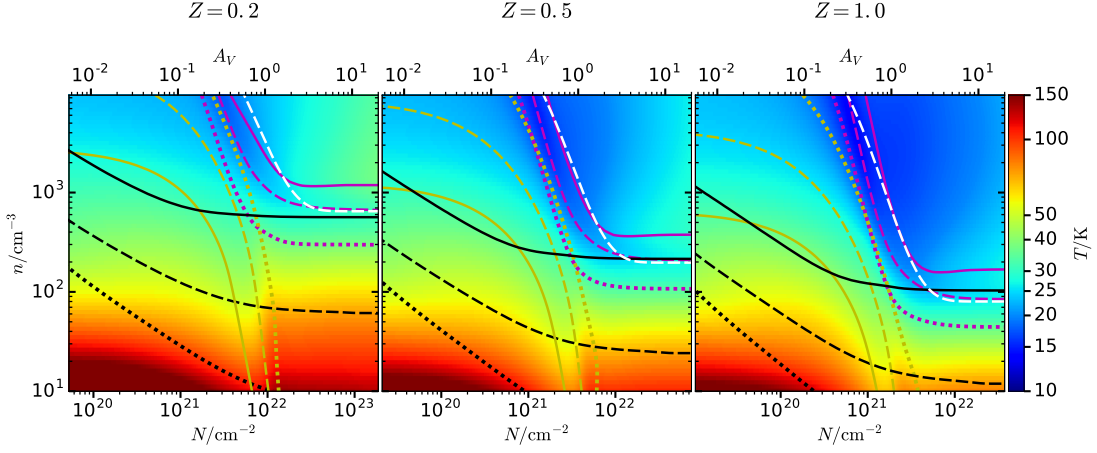


Figure 5. Equilibrium temperature of the gas as a function of A_V (or N) and density n . The black, yellow, and magenta lines are contours of the equilibrium values for $2x(\text{H}_2)$, $x(\text{C}^+)/x_{\text{C,tot}}$ and $x(\text{CO})/x_{\text{C,tot}}$ equal to 0.1 (dotted), 0.5 (dashed), and 0.9 (solid). The white dashed line shows the fit for the $x(\text{CO})/x_{\text{C,tot}} = 0.5$ contour (magenta dashed line) in Equation (25). From left to right, the gas metallicities and dust abundances are set to be $Z = 0.2, 0.5,$ and 1.0 . The incident normalized radiation field $\chi = 1$, and cosmic-ray ionization rate $\xi_{\text{H}} = 2 \times 10^{-16} \text{s}^{-1} \text{H}^{-1}$.

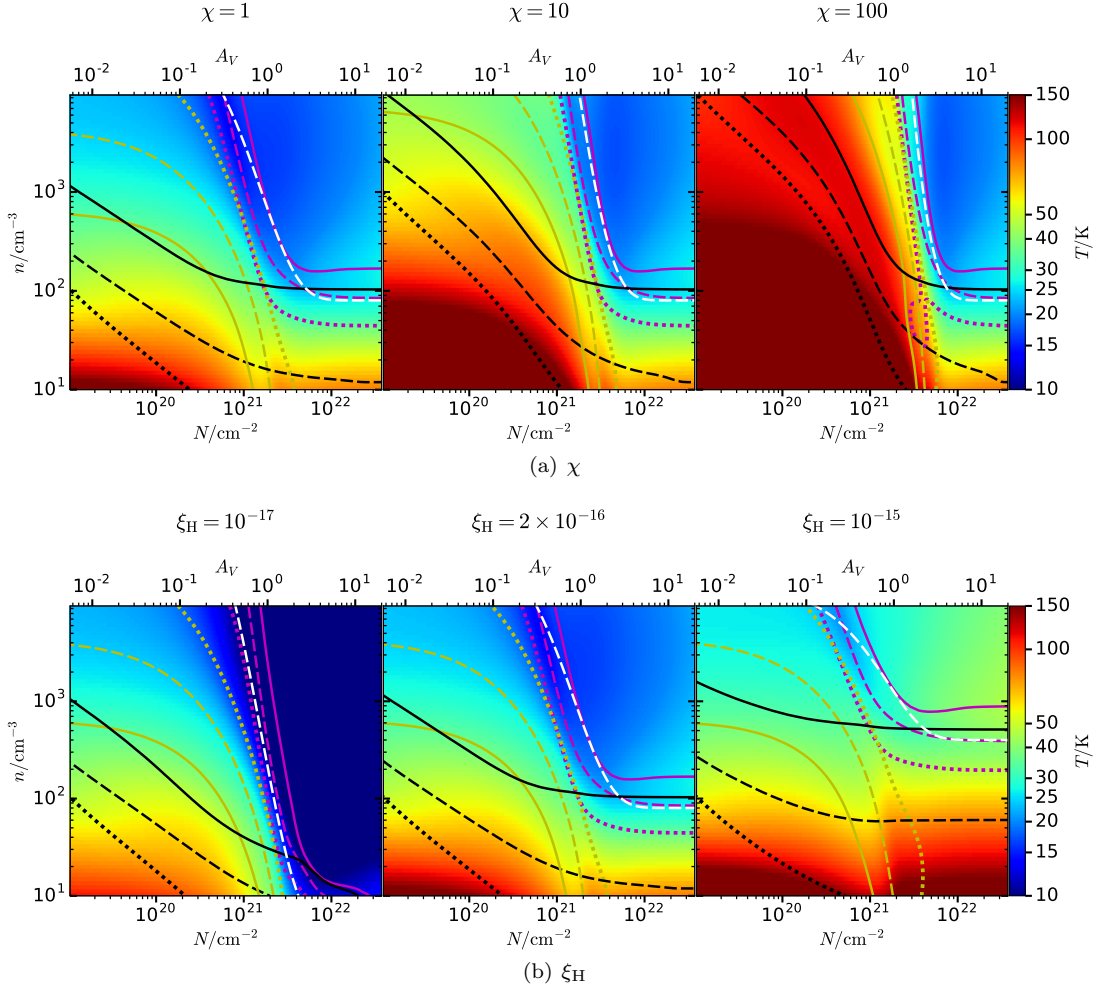


Figure 6. Gas temperature as a function of A_V (or N) and n with solar metallicity $Z = 1$. Panel (a) varies the incident FUV radiation field strength $\chi = 1, 10,$ and 100 while keeping the cosmic-ray ionization rate $\xi_{\text{H}} = 2 \times 10^{-16} \text{s}^{-1} \text{H}^{-1}$. Panel (b) varies the cosmic-ray ionization rate $\xi_{\text{H}} = 10^{-17}, 2 \times 10^{-16},$ and $10^{-15} \text{s}^{-1} \text{H}^{-1}$, while keeping $\chi = 1$. The contours of the H_2 , CO , and C^+ abundances, and the fit of the $x(\text{CO})/x_{\text{C,tot}} = 0.5$ contour, are also plotted, similar to Figure 5.

ure 6 (b), the contours defining the CO-dominated region also clearly delimit the low temperature ($T \lesssim 20\text{K}$) gas, except at the highest levels of ξ_{H} . The temperature of the bulk of the gas in the CO-dominated regime depends on ξ_{H} but not on χ . This is because when $x(\text{CO})/x_{\text{C,tot}} \approx 1$, the heating and cooling are respectively dominated by cosmic-ray ionization and CO rotational transitions. The temperature is obtained by balancing Equation (B1) (with Equation (B3)) with Equation (B5). We suggest that the temperature of CO, especially the optically thin isotopes, can be an indicator to probe the cosmic-ray ionization rate in dense molecular gas. Observations of star forming regions near the galactic center indicate that CO gas there is indeed warmer than that in the galactic disk (Güsten & Philipp 2004; Ao et al. 2013; Bally & Hi-GAL Team 2014). The higher cosmic ray production rate due to higher SFR in the galactic center may explain the elevated temperature of the CO gas there. However, if only the ^{12}CO ($J = 1 - 0$) line is observed, because it is usually optically thick, the luminosity of the line is determined mostly by the temperature at the cloud surface, where photoelectric heating can dominate over cosmic-ray heating. Therefore, as pointed out by Wolfire et al. (1993), the luminosity of the CO ($J = 1 - 0$) line is mostly determined by the strength of UV radiation, instead of the cosmic-ray ionization rate.

In galactic disks where the warm and cold atomic gas are in pressure equilibrium, the typical density of the cold neutral medium (CNM) is related to the strength of the ambient radiation field approximately by $n_{\text{CNM}} \propto \chi$ (Wolfire et al. 2003; Ostriker et al. 2010):

$$\frac{n_{\text{CNM}}}{\chi} \approx 23. \quad (23)$$

Krumholz et al. (2009) adopted a similar relation for the density of cold atomic/molecular complexes. Assuming the ambient radiation field strength is proportional to the SFR, then $\chi \propto \Sigma_{\text{SFR}}$, where Σ_{SFR} is the average rate of star formation per unit area in the galactic disk. In equilibrium, Σ_{SFR} is expected to be proportional to the weight of the ISM, which in general depends on both the gas surface density Σ_{gas} and the stellar density (Ostriker et al. 2010; Kim et al. 2011, 2013). In starburst regions where the gas dominates gravity, $\Sigma_{\text{SFR}} \propto \Sigma_{\text{gas}}^2$ (Ostriker & Shetty 2011). Assuming that $\xi_{\text{H}} \propto \Sigma_{\text{SFR}}/\Sigma_{\text{gas}}$ (Ostriker et al. 2010), and $\Sigma_{\text{SFR}}/\Sigma_{\text{gas}} \propto \Sigma_{\text{gas}} \propto \sqrt{\chi}$, we consider the case in which

$$\xi_{\text{H}} = 10^{-16} \sqrt{\chi} \text{ s}^{-1} \text{H}^{-1}. \quad (24)$$

Using $\chi \propto n$ and $\xi_{\text{H}} \propto \sqrt{\chi}$ based on Equations (23) and (24), Figure 7 plots the temperature of the gas in the n - N plane. Comparing to Figure 5, Figure 7 shows clearly that it is very difficult to form CO in metal-poor gas under typical diffuse-ISM conditions, implying gas densities must be enhanced by turbulence or gravity to be well above typical values in the CNM for CO to be present. However, at $Z = 1$, most of the carbon is in CO at $A_V \gtrsim 2$ and $n \gtrsim 100 \text{ cm}^{-3}$. Thus, in regions of galaxies where A_V and n are high enough, gas need not to be in gravitationally bound clouds to be molecular or to emit strongly in CO (see also Elmegreen 1993). This implies that CO emission in the galactic center and star-

burst galaxies may arise largely from diffuse gas. Indeed, observations of CO lines in luminous infrared galaxies by Papadopoulos et al. (2012) found that most of the CO emission can come from warm and diffuse gas in these starburst environments. Figure 7 also shows that in metal-poor galaxies, C could be the most important tracer for shielded gas, as also noted by Glover & Clark (2016). However, the gas that is traced by C is not necessarily primarily molecular H_2 .

We have also found a simple fit for the contour of $x(\text{CO})/x_{\text{C,tot}} = 0.5$ in the plane of $n - A_V$, given values of incident FUV radiation field, cosmic-ray ionization rate, and metallicity:

$$\frac{n_{\text{crit,CO}}}{\text{cm}^{-3}} = \left(4 \times 10^3 Z \xi_{\text{H},16}^{-2}\right)^{\chi_{\text{CO}}^{1/3}} \left(\frac{50 \xi_{\text{H},16}}{Z^{1.4}}\right), \quad (25)$$

where $n_{\text{crit,CO}}$ is the critical value above which $x(\text{CO})/x_{\text{C,tot}} > 0.5$; $\xi_{\text{H},16} = \xi_{\text{H}}/(10^{-16} \text{ s}^{-1} \text{H}^{-1})$; $\chi_{\text{CO}} = \chi \exp(-\gamma_{\text{CO}} A_V)$ is the effective radiation field for CO photodissociation accounting for dust attenuation, and $\gamma_{\text{CO}} = 3.53$ is the dust-shielding factor of CO given in Table 2. Figures 5-7 and 9 shows the fit in Equation (25) (white dashed line) against the true contour of $x(\text{CO})/x_{\text{C,tot}} = 0.5$ (magenta dashed line), demonstrating the good agreement between the two. We note that this fit is only tested here to be applicable in the range of $n \approx 10 - 10^4 \text{ cm}^{-3}$, $\xi_{\text{H}} \approx 10^{-17} - 10^{-15} \text{ s}^{-1} \text{H}^{-1}$, and $Z = 0.2 - 1$.

4.3. Are Molecules Necessary for Low Temperatures?

How sensitive is the gas temperature to the detailed chemistry? Glover & Clark (2012b) showed that in simulations of turbulent clouds, as long as the gas is shielded, atomic gas can reach similarly low temperatures as in molecular gas. Glover & Clark (2012a) also found that the gas temperature in dense clouds can be very similar even if the CO and C abundances produced by different chemical networks vary by more than an order of magnitude.

To directly look into this question, we artificially force the gas into different chemical states by setting the formation rates of CO, C, and H_2 to zero (successively). Figure 8 shows that the equilibrium gas temperatures are very similar with completely different chemical states. C and C^+ can cool the gas just as well as CO.⁹ H_2 only affects the temperature slightly by changing the specific heat of the gas. This confirms the conclusions in Glover & Clark (2012b): any correlation between molecular gas and low temperatures is likely to be coincidental instead of causal. Molecular gas traces low temperatures simply because molecules form in dense and shielded regions that are more efficient at cooling and less exposed to heating.

4.4. Molecular Gas and Star Formation?

Krumholz et al. (2011) argued that H_2 traces star formation because H_2 forms in the same regions where

⁹ Note that we assume the C and C^+ cooling is optically thin, whereas the optical depth effect is taken into account in CO cooling. This is why C and C^+ cool the dense gas to lower temperatures than CO in Figure 8. In reality, C and C^+ will also be optically thick at high columns.

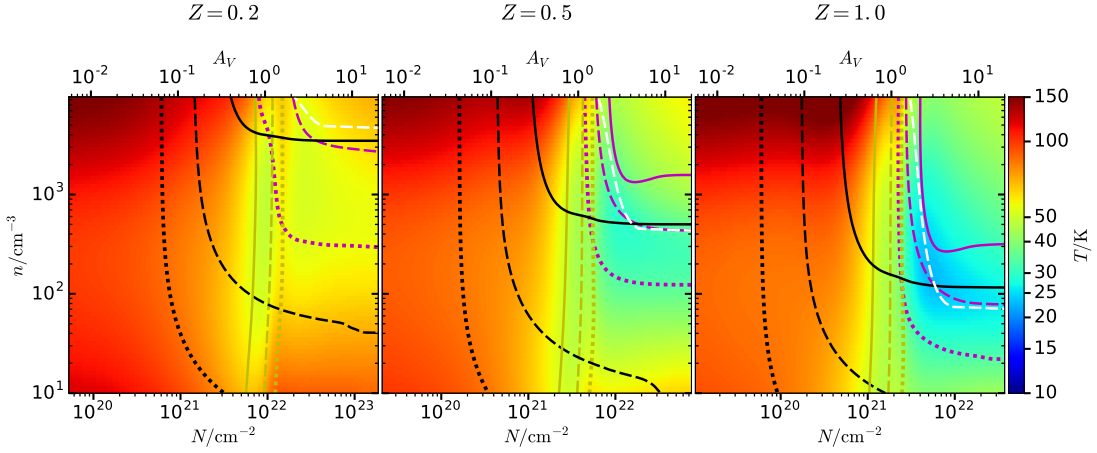


Figure 7. Temperature of the gas as a function of A_V (or N) and density n , similar to Figure 5. The incident radiation field and cosmic-ray ionization rate are set by Equations (23) and (24). The contours represent the abundances of H_2 (black), CO (magenta), and C^+ (yellow), and the fit of the $x(CO)/x_{C,tot}=0.5$ contour (white dashed), similar to Figures 5 and 6.

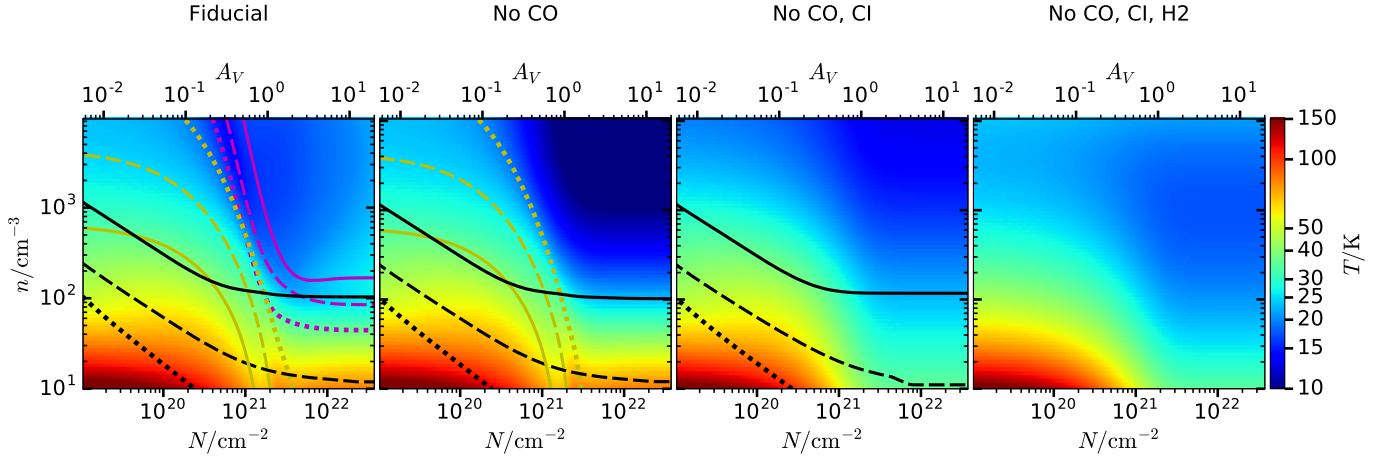


Figure 8. Comparison of equilibrium gas temperature with different chemical compositions. The leftmost panel is the same as the $Z = 1$ case in Figure 5, showing the fiducial model with our chemistry network. The other panels show cases where the formation rates of some species (CO , C , and/or H_2) are artificially set to zero, so the gas is forced to be in a state free of these molecules or atoms. The contours show the transition of H to H_2 (black), C^+ to C (yellow), and C to CO (magenta), similar to Figure 5.

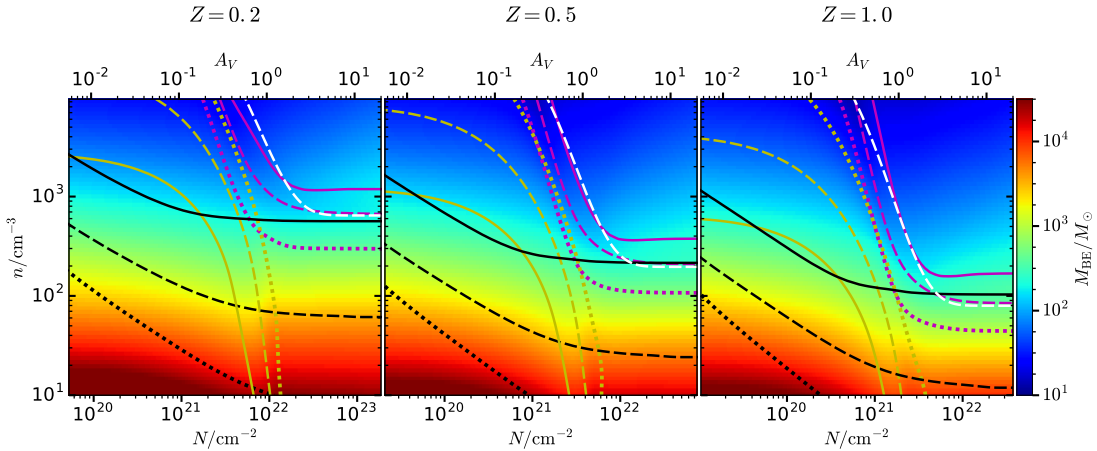


Figure 9. Similar to Figure 5, but for Bonnor–Ebert mass of the gas as a function of A_V (or N) and density n .

the gas is more gravitationally unstable, or, quantitatively speaking, where the critical Bonnor–Ebert mass

$$M_{\text{BE}} = 1.2c_s^3 \left(\frac{\pi^3}{G^3\rho} \right)^{1/2} = 1.2 \left(\frac{\pi^3 k^3 T^3}{G^3 n \mu^4} \right)^{1/2} \quad (\text{Bonnor 1956; Ebert 1955})$$

becomes low. In Figure 9, we show the critical Bonnor–Ebert mass as a function of gas density and column similar to Krumholz et al. (2011), with the improvement that chemistry and temperature are calculated self-consistently. As noted by Krumholz et al. (2011), the contours of the 50% and 90% H₂ abundances are somewhat similar to those of the Bonnor–Ebert mass of the gas. However, we note that the Bonnor–Ebert mass near these contours is $M_{\text{BE}} = 10^2 - 10^3 M_{\odot}$, much larger than the mass of individual stars. In some regions, the Bonnor–Ebert mass is even larger than the available mass in the clouds: for example, at $n = 1000 \text{ cm}^{-3}$ and $A_V = 1$, the total mass of the cloud $M \sim R^3 n m_{\text{H}} \sim (N/n)^3 n m_{\text{H}} \sim 5 M_{\odot}$, and is much smaller than the local Bonnor–Ebert mass $M_{\text{BE}} \sim 100 M_{\odot}$. This suggests that the correlation of H₂ with star formation is not a sufficient pre-condition, but a fairly non-specific coincidence. To reach Bonnor–Ebert masses comparable to those of individual stars, much higher densities are needed than the densities required for high equilibrium H₂ abundance.¹⁰

4.5. Comparison with Observations of Diffuse and Translucent Clouds

The ultimate test for any chemistry model is the comparison with observations. The one-sided equilibrium slab models that we have used to test our network are extremely simple and cannot be expected to agree in detail with the chemical state in the real ISM, which is characterized by complex time-dependent dynamics and morphological structure, both the result of turbulence. Nevertheless, for illustrative purposes it is useful to compare the abundances obtained with our network (for idealized slab geometry) with the observed ISM abundances. To do so, we compiled observations of H₂, CO, C, C⁺, CH_x, and OH_x abundances in the literature derived from UV and optical absorption spectra along different sight lines: H₂, C, and C⁺ observations compiled by Wolfire et al. (2008)¹¹; H₂ and CO observations in Rachford et al. (2002) and Sheffer et al. (2008); H₂ observations in Rachford et al. (2009); H₂, C, and CO observations in Burgh et al. (2010) (hereafter BFJ2010); CH_x¹² abundance in Sheffer et al. (2008) and Crenny & Federman (2004) (hereafter CF2004); and OH_x¹³ abundance in Weselak et al. (2009, 2010). The UV spectroscopy data in these observations mainly come from the *Far Ultraviolet Spectroscopic Explorer (FUSE)*, the Space Telescope Imaging Spectrograph (STIS) on board the *Hubble Space Telescope*, the *UVES* spectrograph at *European Southern Observatory (ESO)* and the *Copernicus* survey. The

¹⁰ Also, as noted above, a small $t_{\text{dyn}}/t_{\text{H}_2}$ or $t_{\text{diss}}/t_{\text{sh}}$ may limit the H₂ abundance at low A_V and n . Non-equilibrium H₂ abundances may be high only in the upper-right corner of each panel, where $M_{\text{BE}} < 100 M_{\odot}$.

¹¹ In Wolfire et al. (2008), most of the C⁺ values are upper limits. Here we only include the true measurements.

¹² CH_x = CH + CH⁺ for Sheffer et al. (2008) and Crenny & Federman (2004).

¹³ OH_x = OH + OH⁺ for Weselak et al. (2009), and OH_x = OH for Weselak et al. (2010).

optical spectra data used to derive CH and CH⁺ abundances in Sheffer et al. (2008) are obtained at the McDonald and European Southern Observatories. For most sightlines, the total column N is derived from reddening data using $N/E(B - V) = 5.8 \times 10^{21} \text{ H cm}^{-2} \text{ mag}^{-1}$ (Bohlin et al. 1978; Rachford et al. 2009), except for sight lines that have H abundances directly observed by Ly α absorption in Bohlin et al. (1978) (included in the compilation of observations by Wolfire et al. (2008)).

We construct a simple one-sided slab model with thermal and chemical equilibrium, as described in Section 4.1, to compare with the observational data. The fiducial model has $\chi = 1$, $\xi_{\text{H}} = 2 \times 10^{-16} \text{ s}^{-1} \text{ H}^{-1}$, and constant densities of $n = 10, 100, \text{ and } 1000 \text{ cm}^{-3}$. We also explore the effects of varying different parameters such as χ , ξ_{H} , the efficiency of grain-assisted recombination, and gas-phase carbon abundance.

Figure 10 shows the comparison between the observations and our slab cloud model in column densities of H₂, CO, C, C⁺ and CH_x and OH_x. For the H to H₂ transition in the left panel, low density $n \sim 10 \text{ cm}^{-2}$ is required to match equilibrium H₂ abundances with observations. This is consistent with the analysis by Bialy et al. (2015, 2017) on the H to H₂ transition layers in the Perseus molecular cloud and star forming region W43.¹⁴

Comparing the right panel with the left, there is much less dispersion in the observed C, CO, and CH_x abundances when plotted against the H₂ column density N_{H_2} instead of the total column N or A_V . This is likely due to foreground or background contaminations: low density atomic ISM is much more “diffuse” in spatial distribution than the relatively “clumpy” molecular ISM. Therefore, the low density atomic clouds may contribute a significant fraction of the total column/visual extinction in a given sight line, without contributing much to the total column of chemical species such as H₂, C, CO, CH_x and OH_x, which mainly form in higher density regions.

In spite of the extreme idealizations adopted, there is generally a good agreement between our model and the observations in Figure 10, especially in the right panel (when plotted against N_{H_2}): we can successfully reproduce the range of observed abundances of CO, CH_x and OH_x with densities between 100 cm^{-3} and 1000 cm^{-3} . It is especially remarkable that CO and CH_x abundances agree over one or two orders of magnitude of N_{H_2} .

However, there is one significant discrepancy between the simple model and observations: the predicted C abundance is too high at a given A_V or N_{H_2} by about an order of magnitude (see Figure 10). This is more clearly shown in the left panel of Figure 11 when plotted with the ratio of CO/C (see also Figure 4 in BFJ2010). To investigate the dependence of CO/C on model parameters, we vary the incident radiation field strength χ , cosmic-ray ionization rate ξ_{H} , the efficiency of grain-assisted recombination of ions, and the gas-phase carbon abundance. The summary of our results is shown in the left panel of

¹⁴ $n \sim 10 \text{ cm}^{-2}$ is in fact lower than densities believed to be in the CNM ($n \sim 40 \text{ cm}^{-2}$ based on pressures from Jenkins & Tripp (2011) and temperatures from Heiles & Troland (2003)). If densities are indeed higher than $n \sim 10 \text{ cm}^{-2}$, this means that the observed abundances are below equilibrium, potentially due to dynamical effects (as discussed previously in Section 4.1).

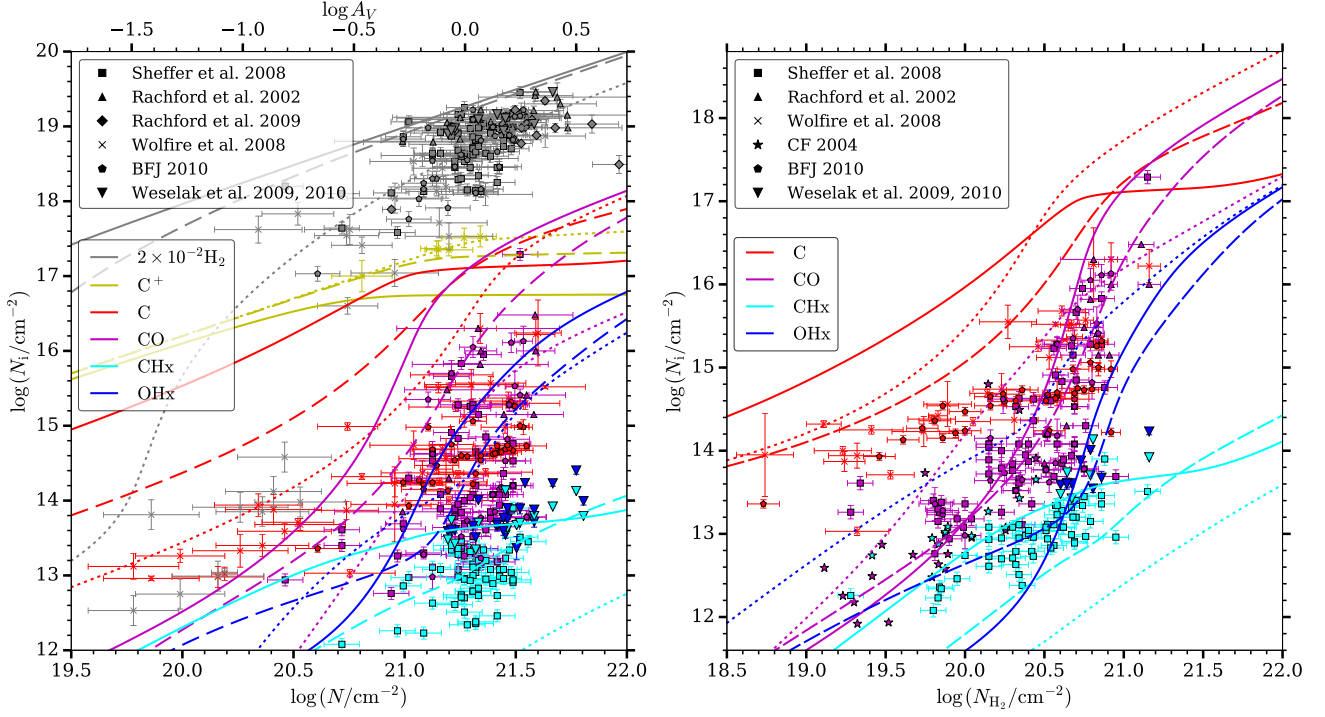


Figure 10. Comparison between observations and our one-sided slab model. The *left* panel plots the column density N_i of chemical species at a given cloud A_V (or N). The lines show the results from our slab model with $n = 10 \text{ cm}^{-3}$ (dotted), $n = 100 \text{ cm}^{-3}$ (dashed), and $n = 1000 \text{ cm}^{-3}$ (solid). Different markers plot the observed abundances from the literature. Different colors represent different species, as shown in the legends. The *right* panel is similar to the left panel, but with the H_2 column density on the x-axis instead.

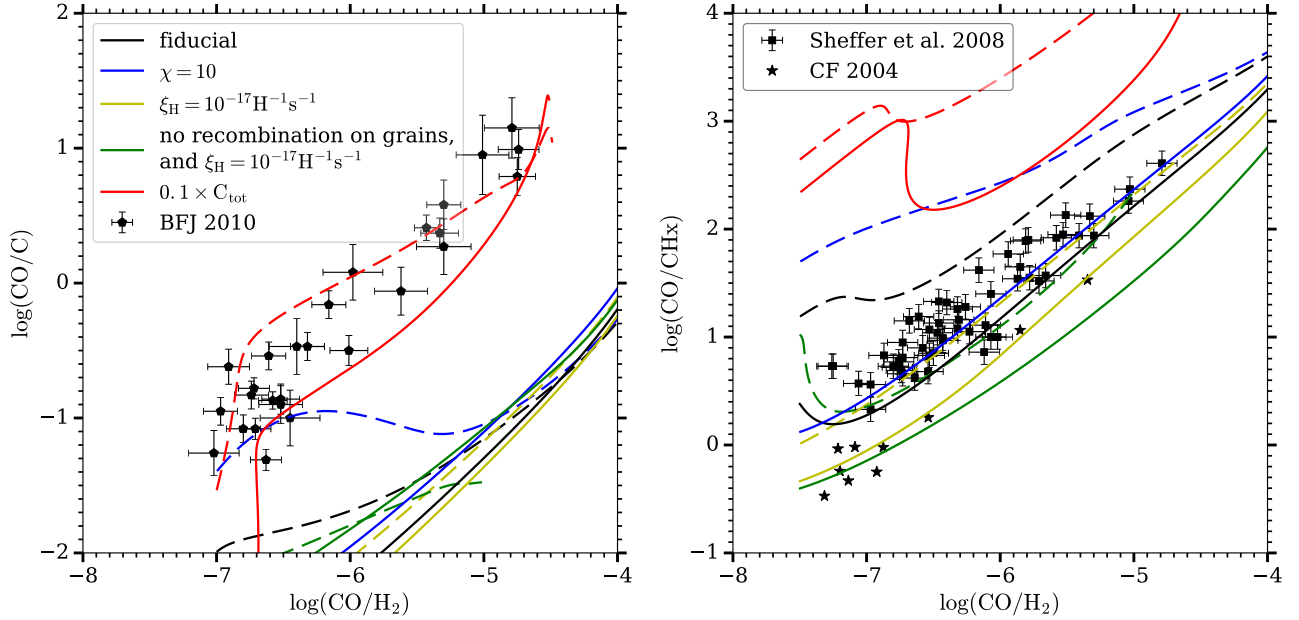


Figure 11. *Left panel:* abundances of CO/C vs. CO/H_2 . The observational data are taken from BFJ2010, and lines of different colors show the results from different slab models (see legend), with $n = 100 \text{ cm}^{-3}$ (dashed), and $n = 1000 \text{ cm}^{-3}$ (solid). *Right panel:* similar to the left panel, but for CO/CH_x on the y-axis. The observed abundance is taken from Sheffer et al. (2008) and CF2004. See also Figure 26 for a more detailed comparison between observations and our model with no grain-assisted recombination, and the depletion of carbon abundance.

Figure 11. Variations in χ and ξ_{H} tend to change the C and CO abundances in the same direction, giving very a similar CO/C ratio to that of the fiducial model. Excluding the grain-assisted recombination of ions does not solve the problem either: it does lower the C abundance at a given A_V , but at the same time, the CO abundance is much lower as well, and the CO/C ratio is still too low (see also the left panel of Figure 26).

Note that our conclusion is different from the conclusion of Liszt (2011), which stated that the absence of grain-assisted recombination can reproduce the high CO/C observed in BFJ2010. We believe this is because Liszt (2011) assumed a constant $x_{\text{HCO}^+} \sim 3 \times 10^{-9}$ in their chemistry model. Without grain-assisted recombination, the HCO^+ abundance is much lower at $x_{\text{HCO}^+} \lesssim 10^{-10}$, leading to much less efficient CO formation than calculated in Liszt (2011)¹⁵.

The only variation of our models that can reproduce the observed CO/C ratio is the one with gas-phase carbon abundance depleted by an order of magnitude relative to the fiducial model, i.e. $C_{\text{tot}}/\text{H} = 0.1(C_{\text{tot}}/\text{H})_{\text{fiducial}} = 1.6 \times 10^{-5}$. This is also found in BFJ2010 (their Figure 4). However, although carbon depletion can be caused by formation of grains such as polycyclic aromatic hydrocarbons (PAHs), a depletion factor as extreme as 0.1 is unlikely. Even the most carbon-depleted sight lines observed in Sofia et al. (2011) and Parvathi et al. (2012) have $C_{\text{tot}}/\text{H} > 6 \times 10^{-5}$ (derived from C^+ absorption measurements), and many of these sight lines are the same as in Burgh et al. (2010). Moreover, as shown in the right panel of Figure 11, the ratio of CO/CH_x in the model with carbon depletion is an order of magnitude higher than the observed values, whereas other models reproduce CO/CH_x consistent with observations. Therefore, we conclude that the depletion of gas-phase carbon is unlikely to be the solution for this problem.

Overpredicting C abundance is also an issue among other PDR models. For example, BFJ2010 compared their observations with the chemistry model by van Dishoeck & Black (1988), and found very similar results. Glover et al. (2010) also predicted $\text{CO}/\text{C} \ll 1$ for $A_V < 2$ clouds with their extensive chemical network (see their Figures 1 and 2). Bensch et al. (2003) observed C and CO emission in the translucent cloud MCLD 123.5+24.9, and also found $\text{CO}/\text{C} \gtrsim 1$. They used the PDR code by Stoerzer et al. (1996) to model their observations, and found that their models also tend to produce a CO/C ratio that is too low, unless they assume a cloud structure of high density ($n \sim 10^4 \text{ cm}^{-3}$) clumps embedded in a low density medium.

It is worth emphasizing that observations compiled here are all for $A_V \lesssim 1$ diffuse and translucent clouds, for which UV or optical absorption observations may be used. For these clouds, most carbon (> 90%) is still in the form of C^+ . The physical properties of these clouds are very different from GMCs and smaller dark molecu-

lar clouds, which typically has $A_V \gg 1$ and most carbon is in the form of CO.

There are some potential solutions to the mismatch of C abundance between equilibrium PDR models and observations. (1) Non-equilibrium chemistry. As previously noted, the photoionization and photodissociation timescales are generally short compared to collisional reactions or grain-assisted reactions (see Tables 1 and 2). Dynamical effects such as limited cloud lifetime and turbulent cycling of gas from a cloud’s interior to its surface can lower the abundances of species formed in low-shielding regions such as C. Furthermore, C tends to form in less dense and shielded regions than CO, and can be more subject to these dynamical effects, which may bring its abundance far from equilibrium. (2) Improvement of chemical networks and reaction rates. It is possible that the chemical pathways to form C and CO in translucent clouds are not well understood, causing discrepancy between chemical models and observations. For example, the composition of dust grains and the rates for grain surface reactions are still uncertain. In addition, turbulent dissipation (Godard et al. 2014) might convert the dominant reservoir of carbon (in C^+) to CO without much production of C. In the future, 3D realistic ISM simulations with time-dependent chemistry will give us more insight into the role of non-equilibrium chemistry.

5. SUMMARY

In this paper, we propose a new lightweight and accurate chemical network for hydrogen and carbon chemistry in the atomic and molecular ISM. Our network is based on the NL99 network in Nelson & Langer (1999) and Glover & Clark (2012a), with significant modifications and extensions. We use 1D uniform slab models to compare our chemical network in detail with results from a full PDR code and also with the original NL99 network.

Our chemical network shows very good agreement with the much more sophisticated PDR code in the equilibrium abundances of all species. This agreement holds in a wide range of densities, visual extinctions, temperature, and metallicities, implying that our simplified network indeed captures the main chemical pathways. The NL99 network, however, performs poorly when comparing to the PDR code in detail. In particular, it significantly underproduces CO at $n \sim 100 - 500 \text{ cm}^{-3}$ when using the realistic cosmic-ray ionization rate $\xi_{\text{H}} = 2 \times 10^{-16} \text{ s}^{-1} \text{ H}^{-1}$ (Indriolo et al. 2007; Hollenbach et al. 2012) in our galaxy. The NL99 network also fails to reproduce the abundances of other species such as C^+ . With only one additional species and 19 additional reactions, our network has a comparable computational cost to the original NL99 network and proves to be much more accurate. Therefore, we conclude that our new network is preferred over the NL99 network for time-dependent numerical simulations of hydrogen and carbon chemistry, such as CO formation.

We apply our network to 1D models and obtain the equilibrium temperature and chemistry in a range of physical conditions, varying the density, incident radiation field strength, cosmic-ray ionization rate, and metallicity. We find that at metallicity $Z = 1$, the CO-dominated regime delimits the coldest gas and that the corresponding temperature tracks the cosmic-ray ioniza-

¹⁵ This is because without grain-assisted recombination, the electron abundance is higher. Electrons destroy H_3^+ , which forms OH_x and subsequently HCO^+ . CO is mainly formed by $\text{HCO}^+ + e \rightarrow \text{CO} + \text{H}$. To be consistent with Liszt (2011), We also use a low cosmic-ray ionization rate $\xi_{\text{H}} = 10^{-17} \text{ s}^{-1} \text{ H}^{-1}$, for the case without grain-assisted recombination.

tion rate in molecular clouds. We note, however, that it is primarily high density and high shielding that leads to low temperatures, rather than the CO abundance itself. In metal-poor gas with $Z \lesssim 0.2$, CO is difficult to form under typical diffuse-ISM conditions and may only be found in regions where gas density is significantly enhanced by turbulence or gravity. We provide a simple fit for the locus of CO-dominated regions as a function of gas density, column, metallicity, and cosmic-ray ionization rate.

We also compiled observations of chemical species in diffuse and translucent clouds, and compared these with our chemistry model predictions, under the assumption of equilibrium. We are able to reproduce the observed CO, CH_x and OH_x abundances with density n between 100 cm^{-3} and 1000 cm^{-3} . However, the predicted C abundances are higher than the observed values by an order of magnitude. Previous equilibrium models have identified a similar difficulty matching C abundances, suggesting that time dependence or other more complex effects may be important. To fully understand the distribution of observed species in the ISM, detailed 3D simulations with realistic gas dynamics and non-equilibrium chemistry are required. We plan to pursue this in the future.

6. ACKNOWLEDGMENTS

The work of Munan Gong and Eve C. Ostriker was supported in part by NSF grant AST-1312006 and NASA grant NNX14AB49G. Mark G. Wolfire was supported in part by NSF grant AST-1411827. We thank the referee for helping us to improve the overall quality of this paper. We also thank Simon Glover and Edward B. Jenkins for many helpful suggestions and discussions. We thank Shmuel Bialy, Amiel Sternberg, Thomas Bisbas, and Daniel W. Savin for providing suggestions and updated rate information.

APPENDIX

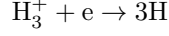
A. DESCRIPTION OF THE CHEMICAL NETWORK

A summary of the chemical network is listed in Tables 1 and 2.

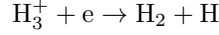
A.1. *Extension of the NL99 Network*

We have added or modified the following reactions to the NL99 network:

1. H_3^+ destruction channel

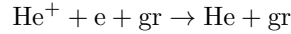
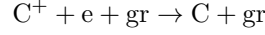


in addition to



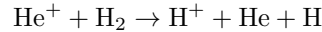
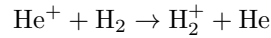
in the original NL99 network, to be more consistent with the hydrogen network adopted in Glover et al. (2010) and Indriolo et al. (2007).

2. Grain-assisted recombination of C^+ and He^+ :



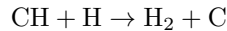
These two grain surface reactions are the main channels for C^+ and He^+ recombination at solar metallicity. Glover & Clark (2012a) considered these two reactions, and concluded that they made very little difference in determining where CO would form. However, we found that using the updated cosmic-ray ionization rate $\xi_{\text{H}} = 2 \times 10^{-16} \text{s}^{-1} \text{H}^{-1}$, instead of their rate $\xi_{\text{H}} = 10^{-17} \text{s}^{-1} \text{H}^{-1}$, these reactions, especially the recombination of C^+ on dust grains, are essential for CO formation at moderate densities $n \lesssim 1000 \text{cm}^{-3}$. This is because electrons from cosmic-ray ionization of H and C inhibit CO formation, while He^+ formed by cosmic rays destroys CO.

3. Cosmic-ray ionization of H and H_2 by secondary electrons. The measurement of cosmic-ray ionization rate $\xi_{\text{H}} = 2.0 \times 10^{-16} \text{s}^{-1} \text{H}^{-1}$ in Indriolo et al. (2007) (ξ_p in their paper) only accounts for the initial (primary) cosmic-ray ionization. The secondary electrons created by the first ionization event can again ionize H and H_2 . The secondary ionization rate depends on factors such as electron abundance (Dalgarno et al. 1999). Here we apply a simple approach motivated by Glassgold & Langer (1974), which has the total ionization rate of H 1.5 times the primary rate in atomic regions and 1.15 times in molecular regions. In regions mixed with atomic and molecular gas, we simply scale the total rate with H and H_2 abundance as shown in reactions 6 and 7 in Table 2. The cosmic-ray ionization rate of H_2 is simply twice that of H.
4. Removed photodissociation of HCO^+ . We find that the destruction of HCO^+ is dominated by the reaction $\text{HCO}^+ + e \rightarrow \text{CO} + \text{H}$, and the photodissociation of HCO^+ has very little effect on the whole chemistry network.
5. He^+ destruction in the H_2 region:



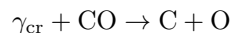
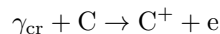
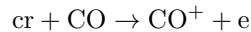
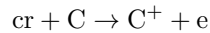
The rates of these two reactions are similar to the rate of direct recombination of He^+ with electrons, and can be higher than the grain surface recombination of He^+ abundance at low metallicities.

6. CH destruction:



This is one of the main destruction channels of CH in shielded regions.

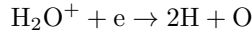
7. Cosmic-ray ionization, and cosmic-ray induced photodissociation of C and CO:



For $\text{cr} + \text{CO} \rightarrow \text{CO}^+ + e$, we assume that CO^+ reacts quickly with H/ H_2 to form HCO^+ , and implement the reaction as $\text{cr} + \text{CO} + \text{H} \rightarrow \text{HCO}^+ + e$ with the same rate. Similar to Clark & Glover (2015), the rates for these

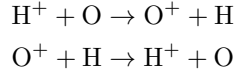
reactions are assumed to be proportional to the cosmic-ray ionization rate of atomic hydrogen ξ_{H} . The scaling factors for cosmic-ray ionization $\xi_{\text{C,CO}}/\xi_{\text{H}}$ are calculated with the rates in McElroy et al. (2013), and the scaling factors for cosmic-ray induced photo-ionization are adopted from Gredel et al. (1987). We also scale the cosmic-ray induced photo-ionization to the H_2 fraction $2n(\text{H}_2)/(2n(\text{H}_2) + 2n(\text{H}))$, because the ionizing photons come from the UV light induced by the primary ionization and excitation of H_2 , and would not be present in regions with only atomic hydrogen. We have also tested the inclusion of cosmic-ray induced photo-reactions of CH and OH using the rates in Gredel et al. (1989), but found they made very little difference for CO formation.

8. $\text{OH}_x + \text{O} \rightarrow 2\text{O} + \text{H}$. This reaction can be important for OH_x destruction in dense and shielded regions, where photodissociation of OH_x is less efficient. See OH_x pseudo-reactions in Appendix A.3.
9. $\text{He}^+ + \text{OH}_x \rightarrow \text{O}^+ + \text{He} + \text{H}$: This can be the major channel for He^+ destruction in shielded regions. See Appendix A.3.
10. $\text{C}^+ + \text{H}_2 + e \rightarrow \text{C} + 2\text{H}$. See the $\text{C}^+ + \text{H}_2$ reaction in Appendix A.2. Note that this is not a three-body reaction but a pseudo-reaction representing a two-body reaction followed by a recombination.
11. H_2O^+ destruction by reacting with electrons:



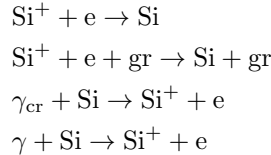
In regions where electron abundance is relatively high, this can be limiting for the abundance of OH_x species. This is applied implicitly as the branching ratio for OH_x formation in reactions 2-5 in Table 1. See Appendix A.3 for details.

12. O^+ species and reactions:



In high temperature regions, the first reaction has a higher rate than the second one (its reverse reaction). O^+ formed by charge exchange with H^+ can react with H_2 , and subsequently form OH^+ . See Appendix A.3.

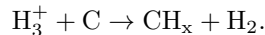
13. Si, Si^+ species and reactions:



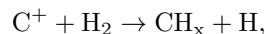
The NL99 network include species M to represent the metals besides C and O. However, the metal abundance they are using, $x_{\text{M,tot}} = 2 \times 10^{-7}$, is much lower than the observed abundances in the solar neighborhood: the most abundant gas-phase metals are S and Si, with $x_{\text{S,tot}} = 3.5 \times 10^{-6}$ (Jenkins 2009), and $x_{\text{Si,tot}} = 1.7 \times 10^{-6}$ (Cardelli et al. 1994). Because the dust-shielding factor $\gamma_{\text{Si}} < \gamma_{\text{C}}$ (see Equation (2) and Table 2), at $A_V \sim 1$, Si^+ can be the main agent for providing electrons where C is already shielded from photo-ionization (see e.g., Figure 14). Although the total abundance of S is higher than Si, we find that including S and S^+ has very little effect on the electron or CO abundances, since $\gamma_{\text{S}} \approx \gamma_{\text{C}}$. Therefore, we only include Si and Si^+ for the metals.

A.2. CH_x Pseudo-reactions

The pseudo-species CH_x includes CH, CH_2 , CH^+ , CH_2^+ , and CH_3^+ . The creation of CH_x is from two reactions. The first one is

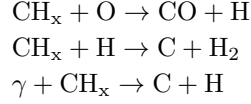


This represents the sum of two reactions: $\text{H}_3^+ + \text{C} \rightarrow \text{CH}^+ + \text{H}_2$, and $\text{H}_3^+ + \text{C} \rightarrow \text{CH}_2^+ + \text{H}$. We use the sum of both rates for this pseudo-reaction. CH^+ reacts with H_2 to form CH_2^+ and H, and CH_2^+ again reacts with H_2 to form CH_3^+ and H. The second one,



represents the reaction of $\text{C}^+ + \text{H}_2 \rightarrow \text{CH}_2^+$. CH_2^+ quickly reacts with H_2 and turns into CH_3^+ and H, which then reacts with an electron. 70% of the reaction $\text{CH}_3^+ + e$ gives CH or CH_2 , and 30% turns back into C. Therefore, we use the rate in Wakelam et al. (2010) multiplied by 0.7 for $\text{C}^+ + \text{H}_2 \rightarrow \text{CH}_x + \text{H}$, and by 0.3 for $\text{C}^+ + \text{H}_2 + e \rightarrow \text{C} + 2\text{H}$.

The recombinations of CH^+ , CH_2^+ , and CH_3^+ with electrons form CH and CH_2 , which can be destroyed in three pathways:



For the reaction $\text{CH}_x + \text{O} \rightarrow \text{CO} + \text{H}$, CH and CH_2 have similar rates. Here we use the rate of CH. For the reactions $\text{CH}_x + \text{H} \rightarrow \text{C} + \text{H}_2$ and $\gamma + \text{CH}_x \rightarrow \text{C} + \text{H}$, CH_2 will react with H to form CH and with a photon to form CH and CH_2^+ . Therefore, we again use the rate assuming CH_x are all in CH.

A.3. OH_x Pseudo-reactions

The pseudo-species OH_x represents OH, H_2O , OH^+ , H_2O^+ , H_3O^+ . The formation of OH_x is mainly through

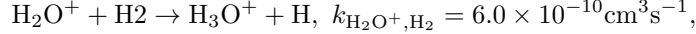


This represents two reactions, the formation of OH^+ and H_2O^+ . The sum of both rates gives the rate of this pseudo-reaction. Another channel for OH_x formation is

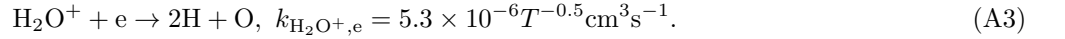


and this represents the reaction $\text{O}^+ + \text{H}_2 \rightarrow \text{OH}^+ + \text{H}$. O^+ mainly comes from the charge exchange $\text{O} + \text{H}^+ \rightarrow \text{O}^+ + \text{H}$.

OH^+ formed by the two channels above reacts with H_2 to form H_2O^+ . The H_2O^+ molecule has two fates: it can again react with H_2 to form H_3O^+ :

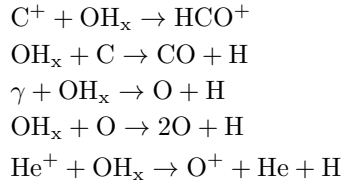


and then H_3O^+ combines with electrons, eventually forming more stable OH and H_2O . Or, the H_2O^+ molecule can be destroyed by electrons:



At low density and low A_V regions where H_2 abundance is low and electron abundance is high, H_2O^+ destruction by Equation (A3) can limit the formation of OH_x by Equations (A1) and (A2). Therefore, we multiply the reaction rates of Equations (A1) and (A2) by a branching factor $r = k_{\text{H}_2\text{O}^+, \text{H}_2} x_{\text{H}_2} / (k_{\text{H}_2\text{O}^+, \text{H}_2} x_{\text{H}_2} + k_{\text{H}_2\text{O}^+, e} x_e)$, and also add the reactions 3 and 5 in Table 1, which is equivalent to the combined reactions of Equations (A1) and (A2) with Equation (A3).

We assume most OH_x are in OH, and use the rate of OH reactions for the following pseudo-reactions of OH_x destruction:



For the reaction $\text{C}^+ + \text{OH}_x \rightarrow \text{HCO}^+$, we use the rate of $\text{C}^+ + \text{OH} \rightarrow \text{CO}^+ + \text{H}$, because CO^+ will quickly react with H_2 to form HCO^+ . We use the rate of reaction $\text{OH} + \text{O} \rightarrow \text{O}_2 + \text{H}$ for $\text{OH}_x + \text{O} \rightarrow 2\text{O} + \text{H}$, assuming most oxygen will be in the form of atomic O.

B. HEATING AND COOLING PROCESSES

A summary of all the heating and cooling processes is listed in Table 3.

B.1. *Heating*B.1.1. *Cosmic-Ray Ionization*

When the gas is ionized by cosmic rays, the primary and secondary electrons thermalize with and heat up the gas. The heating rate per H,

$$\Gamma_{\text{cr}} = \xi q_{\text{cr}}, \quad (\text{B1})$$

where $\xi = \xi_{\text{H}}x(\text{H}) + \xi_{\text{H}_2}x(\text{H}_2) + \xi_{\text{He}}x(\text{He})$, and q_{cr} is the energy added to the gas per primary ionization. We use the result fitted by Draine (2011) to the data of Dalgarno & McCray (1972) in atomic regions:

$$q_{\text{cr,H}} = 6.5 + 26.4 \left(\frac{x(\text{e})}{x(\text{e}) + 0.07} \right)^{0.5} \text{ eV}, \quad (\text{B2})$$

and the fit by Krumholz (2014) to the data of Glassgold et al. (2012) in molecular regions:

$$\frac{q_{\text{cr,H}_2}}{\text{eV}} = \begin{cases} 10, & \log n < 2 \\ 10 + \frac{3(\log n - 2)}{2}, & 2 \leq \log n < 4 \\ 13 + \frac{4(\log n - 4)}{3}, & 4 \leq \log n < 7 \\ 17 + \frac{\log n - 7}{3}, & 7 \leq \log n < 10 \\ 18, & \log n \geq 10 \end{cases}. \quad (\text{B3})$$

Similar to Krumholz (2014), we simply assume that the total heating rate can be calculated by summing the heating rates in the atomic and molecular regions weighted by their number fraction:

$$q_{\text{cr}} = x(\text{H})q_{\text{cr,H}} + 2x(\text{H}_2)q_{\text{cr,H}_2}. \quad (\text{B4})$$

B.1.2. *Photoelectric Effect on Dust Grains*

One main heating source in the ISM comes from the photoelectric effect on dust grains, where electrons ejected from dust grains by FUV radiation thermalize with the gas. We use the results in Weingartner & Draine (2001a) Equation (44) to calculate the heating from the photoelectric effect on dust grains. The rates are extracted from their Table 2, using the values for $R_v = 3.1$, $b_c = 4.0$, and radiation field with ISRF spectrum.

B.1.3. *H₂ Formation on Dust Grains, and UV Pumping of H₂*

We follow Hollenbach & McKee (1979), using their Equation (6.43) for heating from H₂ formation on dust grains and their Equation (6.46) for UV pumping of H₂. Both processes are more efficient at higher densities. The rate of H₂ formation on grains increases with density. For UV pumping, the energy is initially in the excited rotational/vibrational levels of H₂, and subsequently turns into heat by collisional de-excitation.

B.1.4. *H₂ Photodissociation*

The photodissociation of H₂ releases $\sim 0.4\text{eV}$ heat per reaction (Black & Dalgarno 1977; Hollenbach & McKee 1979).

B.2. *Cooling*B.2.1. *Atomic lines: C⁺, C, and O Fine Structure lines, and the Ly α line*

To calculate atomic line cooling, C⁺ and H (Ly α) are considered as two-level systems, and C and O as three-level systems. The calculation of level populations follows the standard procedure, including collisional excitation and de-excitation, photoabsorption, and spontaneous and stimulated emission (e.g. Draine 2011). The species considered for collisional excitation and de-excitation are listed in Table 3.

B.2.2. *CO Rotational Lines*

The CO rotational lines are often optically thick in regions where CO cooling is important. To calculate the cooling rate by CO rotational lines, we use the cooling functions in Omukai et al. (2010) (their Appendix C and Table B2). They use the large velocity gradient (LVG) approximation, similar to the approach by Neufeld & Kaufman (1993). The cooling rate per H is given by

$$\Gamma_{\text{CO}} = L_{\text{CO}}x(\text{CO})n_{\text{H}_2} \quad (\text{B5})$$

where L_{CO} is given in terms of n_{H_2} , $\tilde{N}(\text{CO})$, and T by Equation (B1) in Omukai et al. (2010). In Neufeld & Kaufman (1993) and Omukai et al. (2010), they assume H₂ is the only species responsible for the collisional excitation of the CO rotational levels, which is appropriate in fully molecular regions. To take into account of the collisional excitation

Table 1
List of Collisional Chemical Reactions

No.	Reaction	Rate Coefficient ^a	Notes	Reference ^b
1	$\text{H}_3^+ + \text{C} \rightarrow \text{CH}_x + \text{H}_2$	$1.04 \times 10^{-9} (300/T)^{0.00231} + T^{-3/2} \sum_{i=1}^4 c_i \exp(-T_i/T)$ $c_i = [3.40 \times 10^{-8}, 6.97 \times 10^{-9}, 1.31 \times 10^{-7}, 1.51 \times 10^{-4}]$ $T_i = [7.62, 1.38, 2.66 \times 10^1, 8.11 \times 10^3]$	$\text{H}_3^+ + \text{C} \rightarrow \text{CH}^+ + \text{H}_2$ and $\text{H}_3^+ + \text{C} \rightarrow \text{CH}_2^+ + \text{H}$	1
2	$\text{H}_3^+ + \text{O} \rightarrow \text{OH}_x + \text{H}_2$	$1.99 \times 10^{-9} T^{-0.190} \times r$		20
3	$\text{H}_3^+ + \text{O} + e \rightarrow \text{H}_2 + \text{O} + \text{H}$	$1.99 \times 10^{-9} T^{-0.190} \times (1-r)$	$\text{H}_2\text{O}^+ + e \rightarrow 2\text{H} + \text{O}$	20
4	$\text{O}^+ + \text{H}_2 \rightarrow \text{OH}_x + \text{H}$	$1.6 \times 10^{-9} \times r$		22
5	$\text{O}^+ + \text{H}_2 + e \rightarrow \text{O} + \text{H} + \text{H}$	$1.6 \times 10^{-9} \times (1-r)$ $r = k_{\text{H}_2\text{O}^+, \text{H}_2} x_{\text{H}_2} / (k_{\text{H}_2\text{O}^+, \text{H}_2} x_{\text{H}_2} + k_{\text{H}_2\text{O}^+, e} x_e)$ $k_{\text{H}_2\text{O}^+, \text{H}_2} = 6.0 \times 10^{-10}$ $k_{\text{H}_2\text{O}^+, e} = 5.3 \times 10^{-6} T^{-0.5}$	see Appendix A.3	22
6	$\text{H}_3^+ + \text{CO} \rightarrow \text{HCO}^+ + \text{H}_2$	1.7×10^{-9}		2
7	$\text{He}^+ + \text{H}_2 \rightarrow \text{H}^+ + \text{He} + \text{H}$	$1.26 \times 10^{-13} \exp(-\frac{22.5}{T})$		26
8	$\text{He}^+ + \text{CO} \rightarrow \text{C}^+ + \text{O} + \text{He}$	1.6×10^{-9}		4, 5
9	$\text{C}^+ + \text{H}_2 \rightarrow \text{CH}_x + \text{H}$	$2.31 \times 10^{-13} T^{-1.3} \exp(-\frac{23}{T})$	$\text{C}^+ + \text{H}_2 \rightarrow \text{CH}_2^+$	22
10	$\text{C}^+ + \text{H}_2 + e \rightarrow \text{C} + \text{H} + \text{H}$	$0.99 \times 10^{-13} T^{-1.3} \exp(-\frac{23}{T})$	$\text{C}^+ + \text{H}_2 \rightarrow \text{CH}_2^+$	22
11	$\text{C}^+ + \text{OH}_x \rightarrow \text{HCO}^+$	$9.15 \times 10^{-10} (0.62 + 45.41 T^{-1/2})$	$\text{C}^+ + \text{OH} \rightarrow \text{CO}^+ + \text{H}$	22
12	$\text{CH}_x + \text{O} \rightarrow \text{CO} + \text{H}$	7.7×10^{-11}	$\text{CH} + \text{O} \rightarrow \text{CO} + \text{H}$	22
13	$\text{OH}_x + \text{C} \rightarrow \text{CO} + \text{H}$	$7.95 \times 10^{-10} T^{-0.339} \exp(\frac{0.108}{T})$	$\text{OH} + \text{C} \rightarrow \text{CO} + \text{H}$	21, 22
14	$\text{He}^+ + e \rightarrow \text{He}$	$10^{-11} T^{-0.5} \times [11.19 - 1.676 \log T - 0.2852 (\log T)^2 + 0.04433 (\log T)^3]$	Case B	6, 7
15	$\text{H}_3^+ + e \rightarrow \text{H}_2 + \text{H}$	$4.54 \times 10^{-7} T^{-0.52}$		8
16	$\text{H}_3^+ + e \rightarrow 3\text{H}$	$8.46 \times 10^{-7} T^{-0.52}$		8
17	$\text{C}^+ + e \rightarrow \text{C}$	$k_{\text{rr}} = \frac{2.995 \times 10^{-9}}{\alpha(1.0+\alpha)^{1.0-\gamma} (1.0+\beta)^{1.0+\gamma}}$ $k_{\text{dr}} = T^{-3/2} \times [6.346 \times 10^{-9} \exp(-\frac{12.17}{T}) + 9.793 \times 10^{-9} \exp(-\frac{73.8}{T}) + 1.634 \times 10^{-6} \exp(-\frac{15230}{T})]$ $k = k_{\text{rr}} + k_{\text{dr}}, \alpha \equiv \sqrt{\frac{T}{6.670 \times 10^{-3}}}, \beta \equiv \sqrt{\frac{T}{1.943 \times 10^6}},$ $\gamma \equiv 0.7849 + 0.1597 \exp(-\frac{49550}{T})$	Radiative and dielectronic recombination	9, 23, 27
18	$\text{HCO}^+ + e \rightarrow \text{CO} + \text{H}$	$1.06 \times 10^{-5} T^{-0.64}$		10
19	$\text{H}_2^+ + \text{H}_2 \rightarrow \text{H}_3^+ + \text{H}$	$1.76 \times 10^{-9} T^{0.042} \exp(-\frac{T}{46600})$		7, 11
20	$\text{H}_2^+ + \text{H} \rightarrow \text{H}^+ + \text{H}_2$	6.4×10^{-10}		22
21	$\text{H}^+ + e \rightarrow \text{H}$	$2.753 \times 10^{-14} (\frac{315614}{T})^{1.500} [1.0 + (\frac{115188}{T})^{0.407}]^{-2.242}$	Case B	7, 12
22	$\text{H}_2 + \text{H} \rightarrow 3\text{H}$	$k_{16,l} = 6.67 \times 10^{-12} \sqrt{T} \exp[-(1.0 + \frac{63590}{T})]$ $k_{16,h} = 3.52 \times 10^{-9} \exp(-\frac{43900}{T})$ $n_{\text{cr,H}} = \text{dex}[3.0 - 0.416 \log T_4 - 0.327 (\log T_4)^2]$ $n_{\text{cr,H}_2} = \text{dex}[4.845 - 1.3 \log T_4 + 1.62 (\log T_4)^2]$	Density dependent, see Glover & Mac Low (2007)	13, 14 13, 15 13, 15, 16 13, 17
23	$\text{H}_2 + \text{H}_2 \rightarrow \text{H}_2 + 2\text{H}$	$k_{17,l} = \frac{5.996 \times 10^{-30} T^{4.1881}}{(1.0 + 6.761 \times 10^{-6} T)^{5.6881}} \exp(-\frac{54657.4}{T})$	Density dependent, see Glover & Mac Low (2007)	13, 18 13, 17
24	$\text{H} + e \rightarrow \text{H}^+ + 2e$	$k_{17,h} = 1.3 \times 10^{-9} \exp(-\frac{53300}{T})$ $\exp[-3.271396786 \times 10^1 + 1.35365560 \times 10^1 \ln T_e - 5.73932875 (\ln T_e)^2 + 1.56315498 (\ln T_e)^3 - 2.877056 \times 10^{-1} (\ln T_e)^4 + 3.48255977 \times 10^{-2} (\ln T_e)^5 - 2.63197617 \times 10^{-3} (\ln T_e)^6 + 1.11954395 \times 10^{-4} (\ln T_e)^7 - 2.03914985 \times 10^{-6} (\ln T_e)^8]$		19
25	$\text{He}^+ + \text{H}_2 \rightarrow \text{H}_2^+ + \text{He}$	7.20×10^{-15}		3, 4
26	$\text{CH}_x + \text{H} \rightarrow \text{H}_2 + \text{C}$	$2.81 \times 10^{-11} T^{0.26}$		22
27	$\text{OH}_x + \text{O} \rightarrow 2\text{O} + \text{H}$	3.5×10^{-11}	$\text{OH} + \text{O} \rightarrow \text{O}_2 + \text{H}$	24
28	$\text{Si}^+ + e \rightarrow \text{Si}$	$1.46 \times 10^{-10} T^{-0.62}$		4
29	$\text{He}^+ + \text{OH}_x \rightarrow \text{O}^+ + \text{He} + \text{H}$	$1.35 \times 10^{-9} (0.62 + 45.41 T^{-1/2})$		22
30	$\text{H}^+ + \text{O} \rightarrow \text{O}^+ + \text{H}$	$(1.1 \times 10^{-11} T^{0.517} + 4.0 \times 10^{-10} T^{0.00669}) \exp(-\frac{227}{T})$		25
31	$\text{O}^+ + \text{H} \rightarrow \text{H}^+ + \text{O}$	$4.99 \times 10^{-11} T^{0.405} + 7.5 \times 10^{-10} T^{-0.458}$		25

^aRate coefficients are in units of cm^3s^{-1} . The temperature T is in Kelvin, and $T_4 = T/(10^4\text{K})$. T_e is temperature in the unit of eV/k where k is the Boltzmann constant, i.e., $T_e = 8.6173 \times 10^{-5} T$. $x_i = n_i/n$ is the abundance of species i . χ is the flux of the incident radiation field in $6 - 13.6\text{eV}$ relative to the standard radiation field ($\chi = 1$, $J_{\text{FUV}} = 2.7 \times 10^{-3} \text{erg cm}^{-2}\text{s}^{-1}$) in Draine (1978) units. This field has a strength of $G_0 = 1.7$ in Habing (1968) units. A_V is the visual extinction.

^bReferences: (1)Vissapragada et al. (2016), (2)Kim et al. (1975), (3)Barlow (1984), (4)McElroy et al. (2013), (5)Anicich & Huntress (1986), (6)Hummer & Storey (1998), (7)Glover et al. (2010), (8)Fit by Woodall et al. (2007) to data from McCall et al. (2004), (9)Badnell et al. (2003) (Fitting coefficients are taken for $T \lesssim 10^4$ K from their website <http://amdpp.phys.strath.ac.uk/tamoc/DR/>), (10)Geppert et al. (2005), (11)Linder et al. (1995) (12)Ferland et al. (1992), (13)Glover & Mac Low (2007), (14)Mac Low & Shull (1986), (15)Lepp & Shull (1983), (16)Martin et al. (1996), (17)Shapiro & Kang (1987), (18)Martin et al. (1998), (19)Janev et al. (1987), (20)Fit to de Ruelle et al. (2015), accurate to $\sim 10\%$ at $T = 10 - 1000\text{K}$, (21)Zanchet et al. (2009), (22)Wakelam et al. (2010), (23)Badnell (2006), (24)Carty et al. (2006), (25)Stancil et al. (1999), (26)Fit to Schauer et al. (1989), (27)Bryans et al. (2009).

Table 2
List of Grain-assisted Reactions, Cosmic-ray Reactions, and Photodissociation Reactions

No.	Reaction	Rate coefficient ^a	Notes	Reference ^b
Grain-assisted reactions:				
1	H + H + gr → H ₂ + gr	3.0 × 10 ⁻¹⁷		1, 2
2	H ⁺ + e + gr → H + gr	12.25 × 10 ⁻¹⁴ [1 + 8.074 × 10 ⁻⁶ ψ ^{1.378} × (1 + 508.7T ^{0.01586} ψ ^{-0.4723} - 1.102 × 10 ⁻⁵ ln T)] ⁻¹		3, 4
3	C ⁺ + e + gr → C + gr	45.58 × 10 ⁻¹⁴ [1 + 6.089 × 10 ⁻³ ψ ^{1.128} × (1 + 433.1T ^{0.04845} ψ ^{-0.8120} - 1.333 × 10 ⁻⁴ ln T)] ⁻¹		3
4	He ⁺ + e + gr → He + gr	5.572 × 10 ⁻¹⁴ [1 + 3.185 × 10 ⁻⁷ ψ ^{1.512} × (1 + 5115T ^{3.903} × 10 ⁻⁷ ψ ^{-0.4956} - 5.494 × 10 ⁻⁷ ln T)] ⁻¹		3
5	Si ⁺ + e + gr → Si + gr	2.166 × 10 ⁻¹⁴ [1 + 5.678 × 10 ⁻⁸ ψ ^{1.874} × (1 + 43750T ^{1.635} × 10 ⁻⁶ ψ ^{-0.8964} - 7.538 × 10 ⁻⁵ ln T)] ⁻¹		3
Cosmic-ray ionization or cosmic-ray induced photodissociation:				
6	cr + H → H ⁺ + e	2.3x _{H₂} + 1.5x _H	primary and	8
7	cr + H ₂ → H ₂ ⁺ + e	2 × (2.3x _{H₂} + 1.5x _H)	secondary ionization	8
8	cr + He → He ⁺ + e	1.1		5, 6
9	cr + C → C ⁺ + e	3.85		5, 6
10	cr + CO + H → HCO ⁺ + e	6.52	cr + CO → CO ⁺ + e	5, 6
11	γ _{cr} + C → C ⁺ + e	560		7
12	γ _{cr} + CO → C + O	90		7
13	γ _{cr} + Si → Si ⁺ + e	8400		7
Photoionization and photodissociation reactions ^c :				
14	γ + C → C ⁺ + e	3.5 × 10 ⁻¹⁰ χ exp(-3.76A _V)f _{s,C} (N _C , N _{H₂})		7, 9
15	γ + CH _x → C + H	9.1 × 10 ⁻¹⁰ χ exp(-2.12A _V)	γ + CH → C + H	7
16	γ + CO → C + O	2.4 × 10 ⁻¹⁰ χ exp(-3.88A _V)f _{s,CO} (N _{CO} , N _{H₂})		7, 10
17	γ + OH _x → O + H	3.8 × 10 ⁻¹⁰ χ exp(-2.66A _V)	γ + OH → O + H	7
18	γ + Si → Si ⁺ + e	4.5 × 10 ⁻⁹ χ exp(-2.61A _V)		7
19	γ + H ₂ → H + H	5.7 × 10 ⁻¹¹ χ exp(-4.18A _V)f _{s,H₂} (N _{H₂})		7, 11

^aRate coefficients are in units of cm³s⁻¹Z_d⁻¹ for grain-assisted reactions, where Z_d is the dust abundance relative to the solar neighbourhood (the reaction rates for grain-assisted reactions are x_in_{gr}, where k_{gr} is the listed rate coefficient, and x_i = x_{H₂} for reaction 1 and x_i = x_{ion} for reactions 2-5); ξ_H for cosmic-ray ionization where ξ_H = 2.0 × 10⁻¹⁶s⁻¹H⁻¹ is the local primary cosmic-ray ionization rate for atomic H per H atom (Indriolo et al. 2007); and s⁻¹ for photoreactions. n_e is the number density of electrons. x_i = n_i/n is the abundance of species *i*. χ is the flux of the incident radiation field in 6 – 13.6eV relative to the standard radiation field (χ = 1, J_{FUV} = 2.7 × 10⁻³erg cm⁻²s⁻¹) in Draine (1978). This field has a strength of G₀ = 1.7 in Habing (1968) units. A_V is the visual extinction.

^bReferences: (1) Wolfire et al. (2008), (2)Hollenbach et al. (2012), (3)Weingartner & Draine (2001a), (4)Draine (2003), (5)Glover et al. (2010), (6)Le Teuff et al. (2000), (7)Heays et al. (2017), (8)Glassgold & Langer (1974), (9)Tielens & Hollenbach (1985), (10)Visser et al. (2009), (11)Draine & Bertoldi (1996).

^cThe self-shielding of H₂ and self-shielding plus shielding from H₂ of CO and C are included in the factors f_{s,H₂}(N_{H₂}), f_{s,CO}(N_{CO}, N_{H₂}), and f_{s,C}(N_C, N_{H₂}). This is described in detail in Section 2.1.2.

by atomic hydrogen and electrons, we replace n_{H₂} in Equation (B5) with an effective number density, following Yan (1997), Meijerink & Spaans (2005) and Glover et al. (2010):

$$n_{\text{eff,CO}} = n_{\text{H}_2} + \sqrt{2} \left(\frac{\sigma_{\text{H}}}{\sigma_{\text{H}_2}} \right) n + \left(\frac{1.3 \times 10^{-8} \text{ cm}^3 \text{ s}^{-1}}{\sigma_{\text{H}_2} v_e} \right) n_e, \quad (\text{B6})$$

where $\sigma_{\text{H}} = 2.3 \times 10^{-15} \text{ cm}^2$, $\sigma_{\text{H}_2} = 3.3 \times 10^{-16} (T/1000\text{K})^{-1/4} \text{ cm}^2$ and $v_e = 1.03 \times 10^4 (T/1\text{K})^{1/2} \text{ cm s}^{-1}$.

In LVG approximation, the escape probability of a photon emitted by CO is related to the effective column density parameter

$$\tilde{N}(\text{CO}) = \frac{n(\text{CO})}{|\nabla v|}, \quad (\text{B7})$$

where $n(\text{CO})$ is the local CO number density and ∇v is the local gas velocity gradient. In Omukai et al. (2010), they used the approximation $\tilde{N}(\text{CO}) = N(\text{CO})/\sqrt{2kT/m(\text{CO})}$, where T is the gas temperature, $N(\text{CO})$ the total CO column density, and $m(\text{CO})$ the mass of a single CO molecule. This assumes thermal motions dominate the velocity of CO molecules. However, in realistic molecular clouds, the gas velocity will be largely determined by the supersonic turbulence. For Milky Way molecular clouds, the observed turbulence spectrum obeys the line-width size relation (Larson 1981; Solomon et al. 1987; Heyer & Brunt 2004):

$$v(L) \sim 1 \text{ km/s} \left(\frac{L}{\text{pc}} \right)^{1/2}. \quad (\text{B8})$$

In our slab models, we use the velocity determined using Equation (B8) to calculate the effective CO column density parameter $\tilde{N}(\text{CO}) = N(\text{CO})/v(L)$, where $N(\text{CO})$ is the column density of CO from the local position to the edge of the one-sided slab. This assumes that for thicker clouds, the global turbulent velocity will be larger as implied

by Equation (B8). We have also tried using a constant velocity $v = 1\text{km/s}$ to calculate \tilde{N} , and the results for the equilibrium temperature in CO-dominated regions are very similar.

Care needs to be taken when the temperature $T < 10\text{K}$. Omukai et al. (2010) only gives fitting parameters down to $T = 10\text{K}$, and naive extrapolation may give a finite cooling rate even when the temperature is close to zero. Moreover, CO can freeze-out onto dust grains in regions with high density and $T \lesssim 10\text{K}$, leading to depleted CO abundance (Bergin et al. 1995; Acharyya et al. 2007). For simplicity, we artificially turn off CO cooling at temperatures below 10K. Omukai et al. (2010) also only gives fitting parameters up to $T = 2000\text{K}$. For $T > 2000\text{K}$, we simply use the CO cooling rate at $T = 2000\text{K}$. In reality, CO will likely be destroyed by collisional dissociation and ionization at such high temperatures.

B.2.3. H_2 Rotational and Vibrational Lines

We use the results in Glover & Abel (2008) to calculate cooling by H_2 rotational and vibrational lines. The cooling rate per H_2 molecule Λ_{H_2} is approximated by

$$\Lambda_{\text{H}_2} = \frac{\Lambda_{\text{H}_2,\text{LTE}}}{1 + \Lambda_{\text{H}_2,\text{LTE}}/\Lambda_{\text{H}_2,n \rightarrow 0}}, \quad (\text{B9})$$

where $\Lambda_{\text{H}_2,\text{LTE}}$ is the cooling rate at high densities when H_2 level populations are in local thermal equilibrium, and $\Lambda_{\text{H}_2,n \rightarrow 0}$ is the cooling rate in the low density limit. We use Equations (6.37) and (6.38) in Hollenbach & McKee (1979) to calculate $\Lambda_{\text{H}_2,\text{LTE}} = \Lambda_{\text{H}_2,\text{LTE,rot}} + \Lambda_{\text{H}_2,\text{LTE,vib}}$ for H_2 rotational and vibrational lines. $\Lambda_{\text{H}_2,n \rightarrow 0}$ is obtained by the fitting functions provided in Glover & Abel (2008), including collisional species H, H_2 , He, H^+ , and e. We use the fitting parameters in their Table 8, assuming a fixed ortho-to-para ratio of H_2 of 3:1. Glover & Abel (2008) only gives the fit for H_2 cooling in the temperature range $20\text{K} < T < 6000\text{K}$. Similar to the treatment in CO rotational line cooling, we artificially cut off H_2 cooling below 10K, and use the H_2 cooling rate at $T = 6000\text{K}$ for $T > 6000\text{K}$. In reality, H_2 cooling rate is likely to be negligible at $T < 10\text{K}$.

B.2.4. Dust Thermal Emission

By exchanging energy with dust via collision, gas can either heat or cool. The rate of gas–dust energy exchange is given by (Krumholz 2014):

$$\Psi_{\text{gd}} = \alpha_{\text{gd}} n Z_{\text{d}} T_{\text{g}}^{1/2} (T_{\text{d}} - T_{\text{g}}), \quad (\text{B10})$$

where Z_{d} is the dust abundance relative to the Milky Way, and α_{gd} the dust–gas coupling coefficient. Positive Ψ_{gd} means heating of the gas, and negative means cooling of the gas. In the realistic ISM, dust almost always acts to cool the ISM with $T_{\text{d}} < T_{\text{g}}$. We use $\alpha_{\text{gd}} = 3.2 \times 10^{-34} \text{erg s}^{-1} \text{cm}^3 \text{K}^{-3/2}$ for H_2 -dominated regions (Goldsmith 2001). α_{gd} is expected to be a factor ~ 3 higher in H-dominated regions (Krumholz et al. 2011), but dust cooling is likely to be only important in dense regions dominated by H_2 .

The dust temperature T_{d} necessary for evaluating Ψ_{gd} is determined by the total rate of change of dust specific energy per H nucleus (Krumholz 2014):

$$\frac{de_{\text{d,sp}}}{dt} = \Gamma_{\text{ISRF}} + \Gamma_{\text{d,line}} + \Gamma_{\text{d,CMB}} + \Gamma_{\text{d,IR}} - \Lambda_{\text{d}} - \Psi_{\text{gd}} \quad (\text{B11})$$

Because the dust specific heat is very small compared to the gas, we can always assume the dust temperature is in equilibrium, $de_{\text{d,sp}}/dt = 0$. Note that for very small dust with size $a \lesssim 10\text{\AA}$, they are not in thermal equilibrium, and can have temperature spikes (Draine 2011). Here we mainly consider bigger grains. In principle, given all the terms in Equation (B11), one can solve for T_{d} . However, because Equation (B11) is a non-linear function of T_{d} , this procedure will involve a costly root-finding algorithm. For the purposes of this paper, we assume a fixed dust temperature $T_{\text{d}} = 10\text{K}$. In the density range $n < 10^4 \text{cm}^{-3}$ that we consider, dust cooling is never important and contributes to less than $\sim 5\%$ of the total cooling rate.

B.2.5. Recombination of e on PAHs

At high temperatures $T \sim 10^3 - 10^4\text{K}$, cooling by electron recombination on PAHs can be important relative to the photoelectric heating on dust. Following Weingartner & Draine (2001a) Equation (45), we use the parameters in their Table 3 ($R_{\text{v}} = 3.1$, $b_{\text{c}} = 4.0$, ISRF) to calculate the cooling rate from electron recombination on PAHs.

B.2.6. Collisional Dissociation of H_2 and Collisional Ionization of H

The collisional dissociation of H_2 and ionization of H takes 4.48eV and 13.6eV energy per reaction (Grassi et al. 2014).

C. ADDITIONAL PLOTS AND DISCUSSIONS FOR CODE TEST AND COMPARISON

C.1. Chemistry with Constant Temperature

Here we show the comparison with the PDR code, our chemical network, and the NL99 network. The chemistry is evolved until it reaches equilibrium, and we fix the temperature at $T = 20\text{K}$. All independent species are shown between densities $n = 50 \text{cm}^{-3}$ and $n = 1000 \text{cm}^{-3}$, supplementing Figures 2 and 4. Figures 12 and 14 plot the abundances, and Figures 13 and 15 plot the integrated column densities of different species.

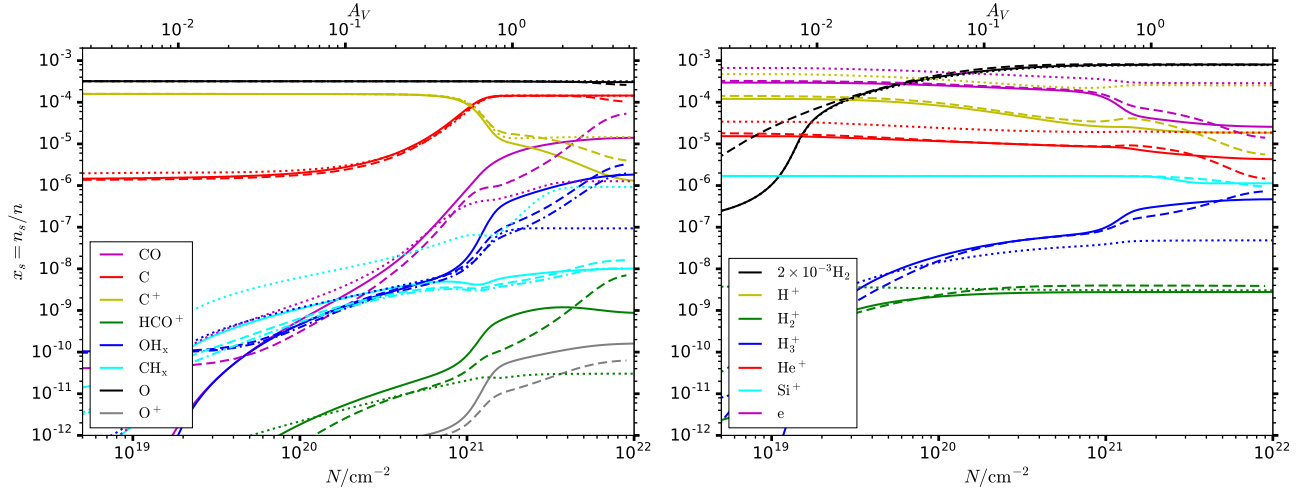
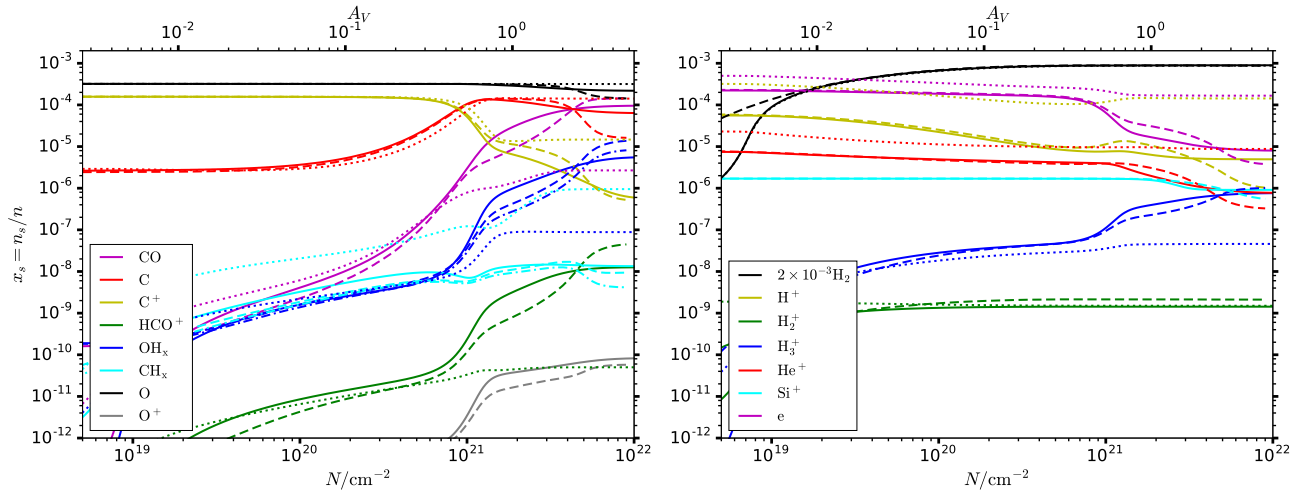
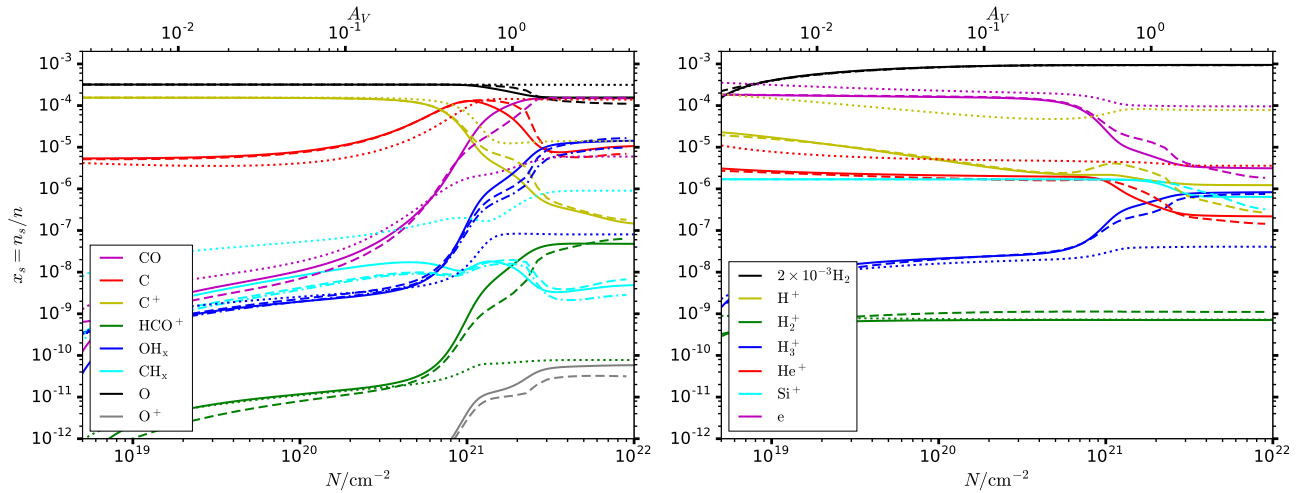
(a) $n = 50 \text{ cm}^{-3}$ (b) $n = 100 \text{ cm}^{-3}$ (c) $n = 200 \text{ cm}^{-3}$

Figure 12. Abundances of all independent species at densities $n = 50\text{--}200 \text{ cm}^{-3}$ in our network (solid), the PDR code (dashed), and the NL99 network (dotted), as a function of A_V/N . These figures are similar to Figure 2. Different species are represented by different colors as indicated in the legends. The abundance of H_2 is multiplied by a factor of 2×10^{-3} , i.e., if all hydrogen is in H_2 , the black line will be at 10^{-3} . We have also plotted the abundances of CH and OH species from PDR code (cyan and blue dash-dotted lines), in addition to the sum of all CH_x and OH_x species. The cosmic-ray ionization rate $\xi_{\text{H}} = 2 \times 10^{-16} \text{ s}^{-1} \text{ H}^{-1}$, and gas temperature is fixed at $T = 20 \text{ K}$.

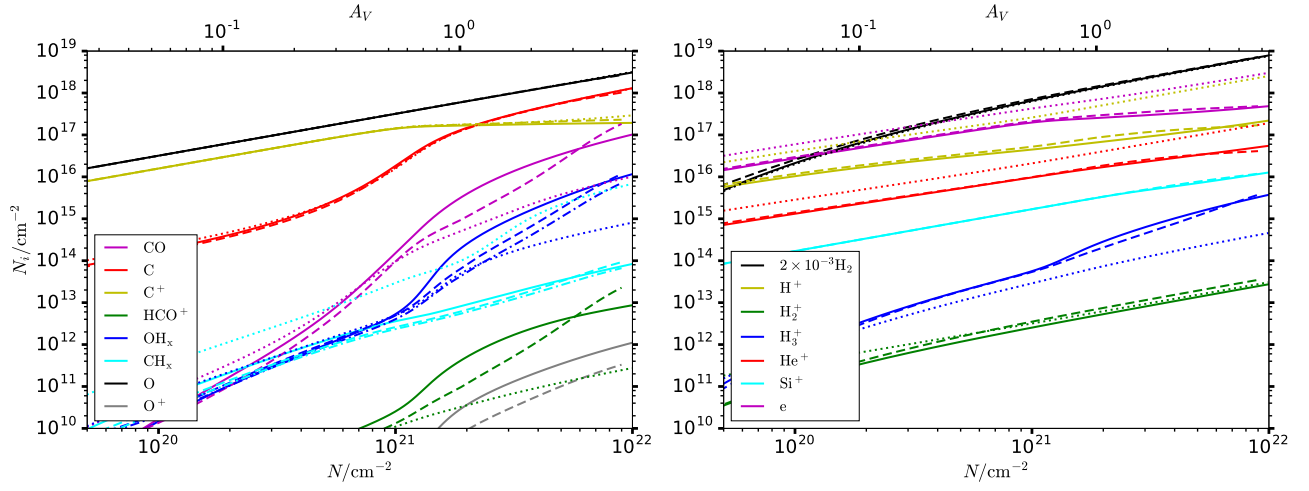
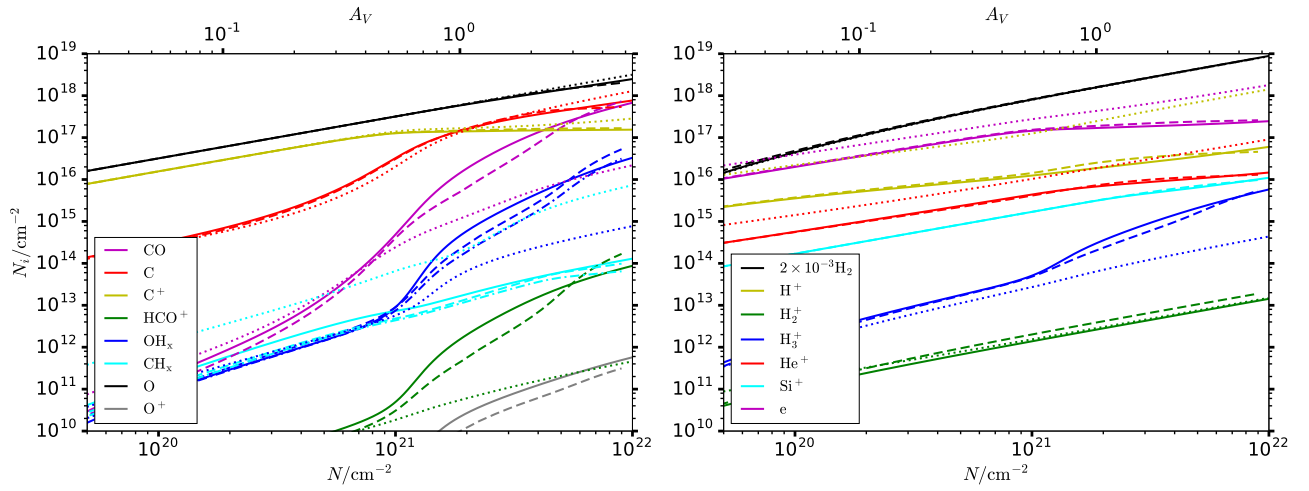
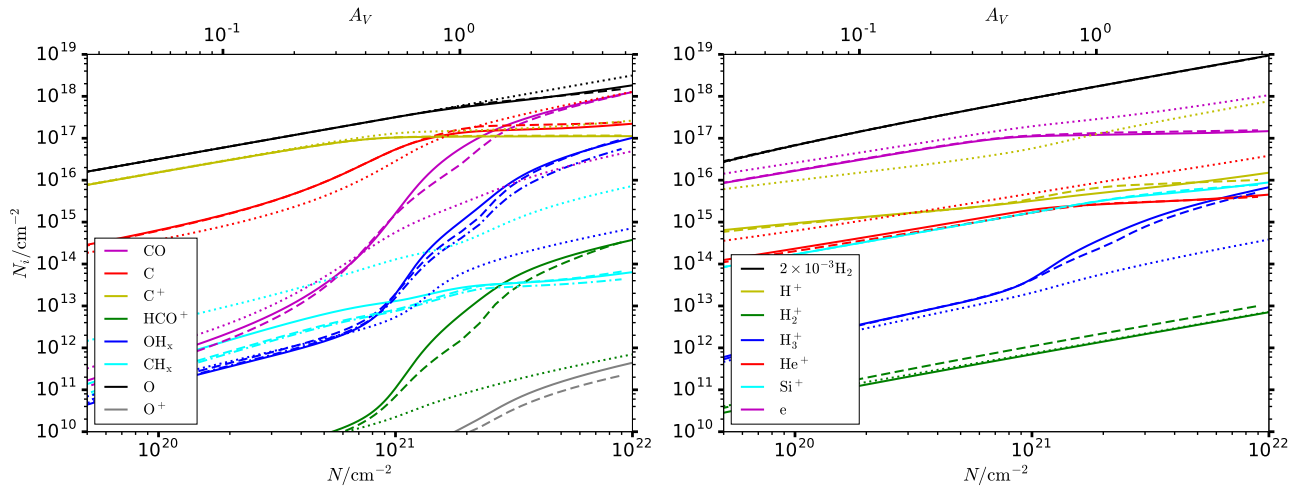
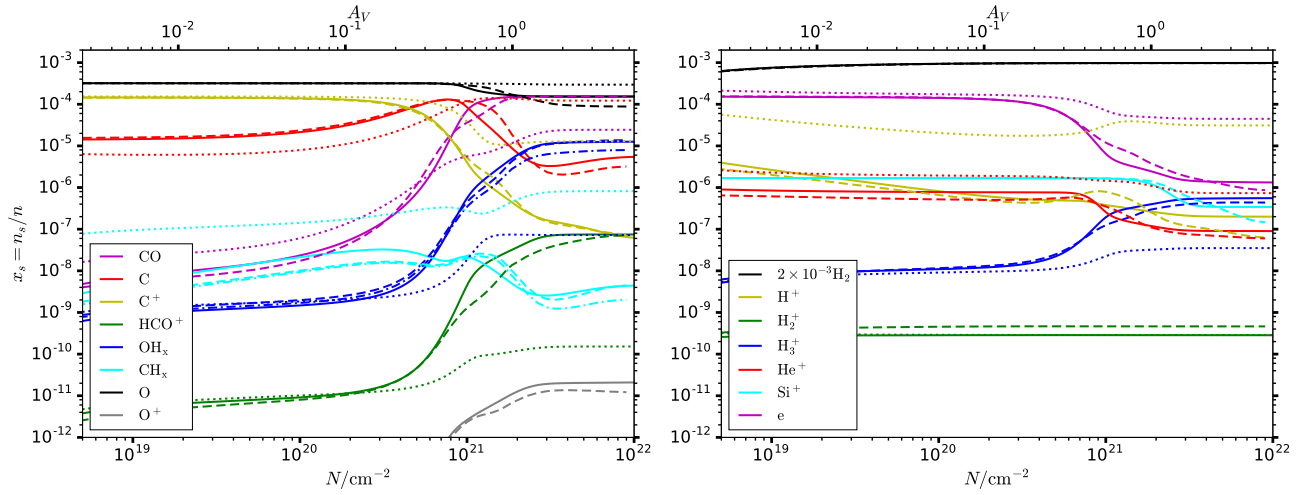
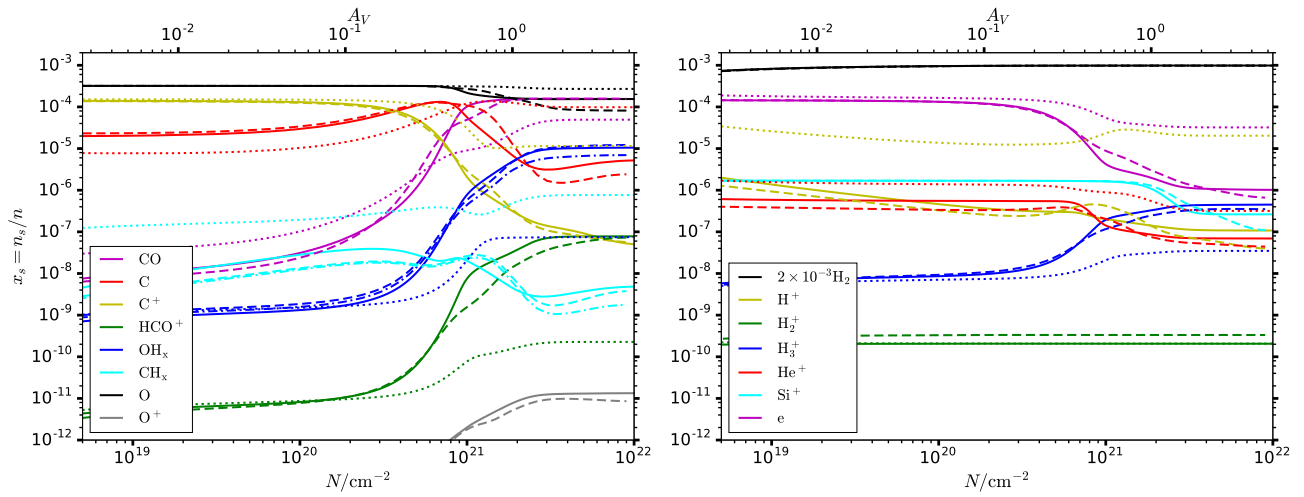
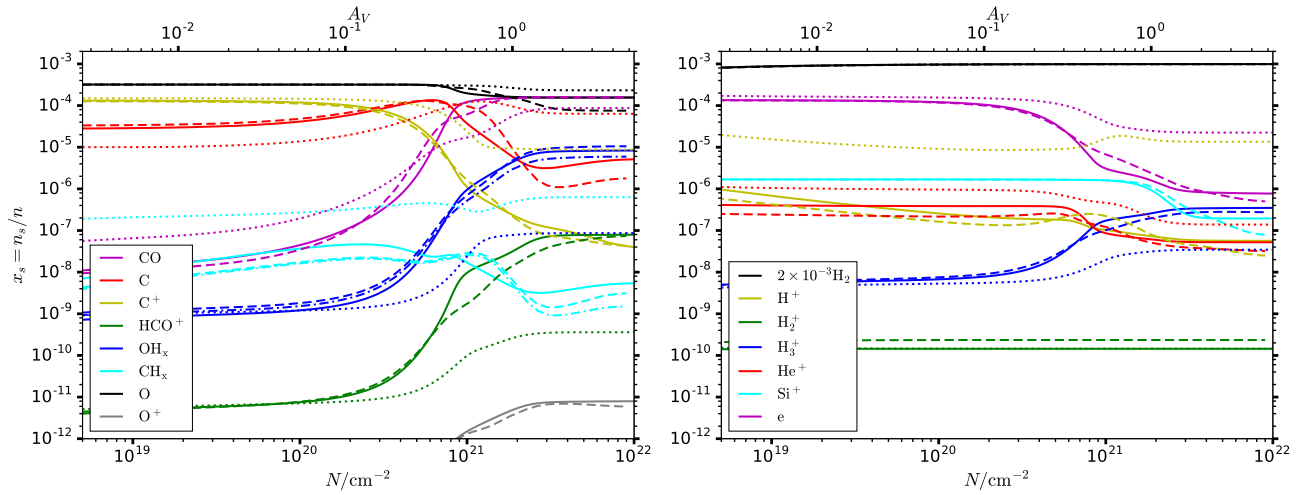
(a) $n = 50 \text{ cm}^{-3}$ (b) $n = 100 \text{ cm}^{-3}$ (c) $n = 200 \text{ cm}^{-3}$

Figure 13. Integrated column densities of all independent species at densities $n = 50 - 200 \text{ cm}^{-3}$ as a function of A_V/N , similar to Figure 4. Line colors and styles are the same as in Figure 12.

(a) $n = 500 \text{ cm}^{-3}$ (b) $n = 700 \text{ cm}^{-3}$ (c) $n = 1000 \text{ cm}^{-3}$ **Figure 14.** Abundances of all independent species at densities $n = 500 - 1000 \text{ cm}^{-3}$, similar to Figure 12.

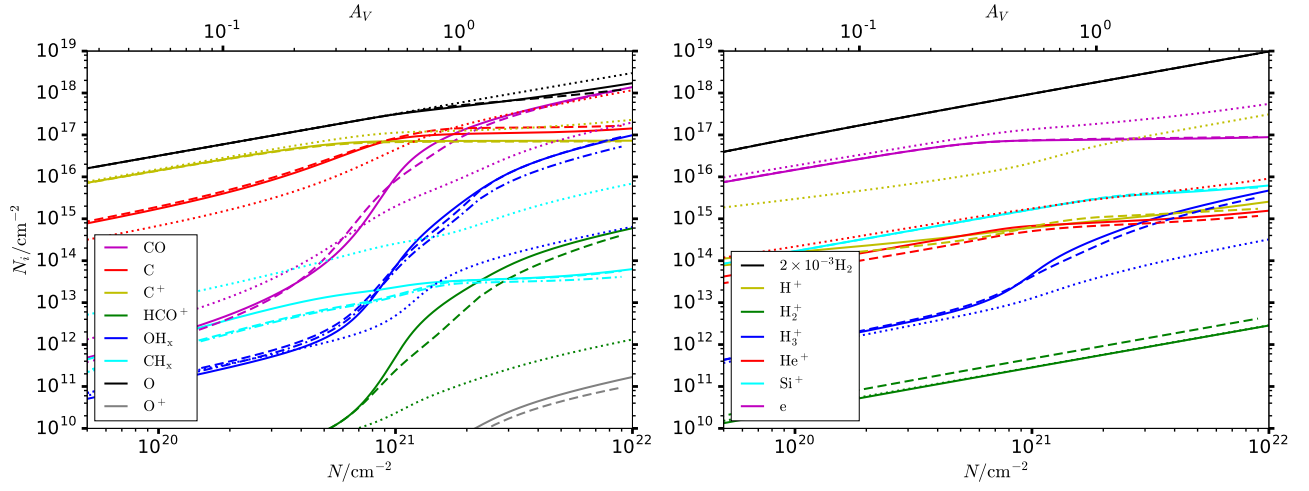
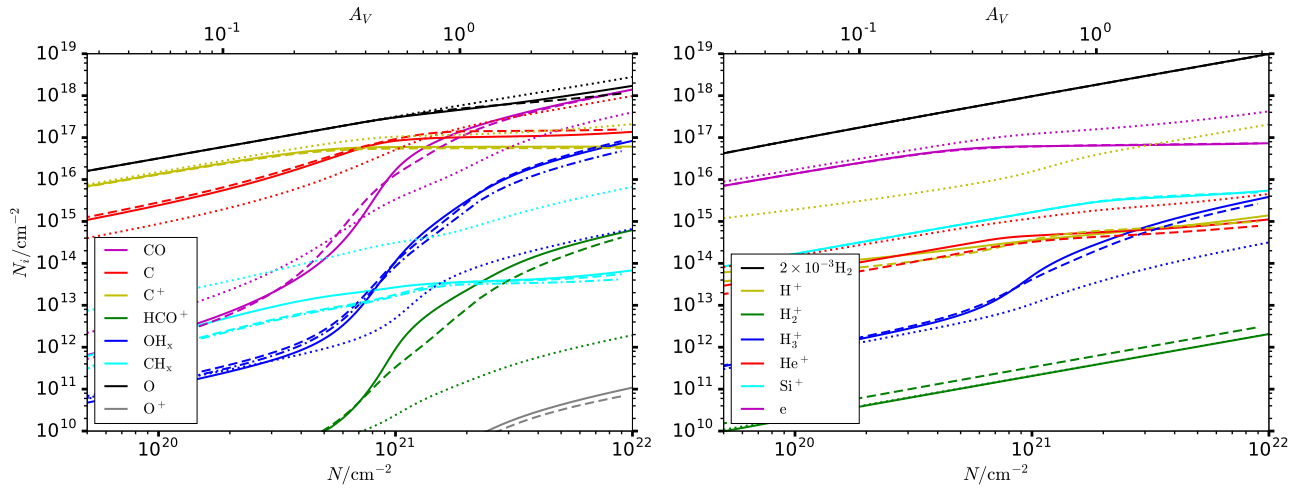
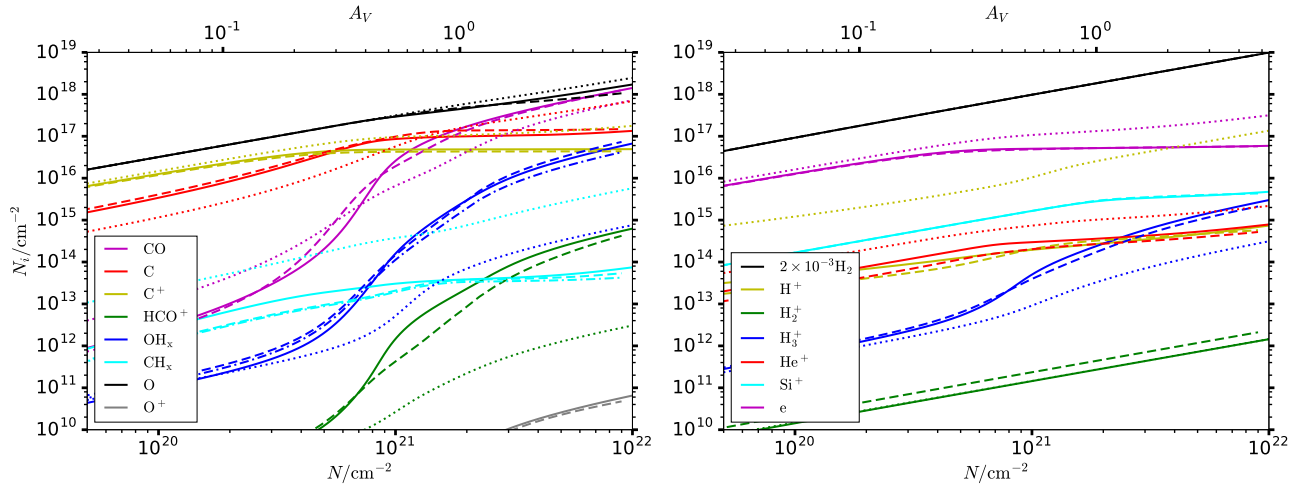
(a) $n = 500 \text{ cm}^{-3}$ (b) $n = 700 \text{ cm}^{-3}$ (c) $n = 1000 \text{ cm}^{-3}$

Figure 15. Integrated column densities of all independent species at densities $n = 500 - 1000 \text{ cm}^{-3}$, similar to Figure 13.

Table 3
List of Heating and Cooling Processes

Process	Reference
Heating:	
Cosmic-ray ionization of H, H ₂ and He	Cosmic-ray ionization rate – See Table 2 Heating rate per primary ionization in atomic region – Dalgarno & McCray (1972) Heating rate per primary ionization in molecular region – Glassgold et al. (2012)
Photoelectric effect on dust grains	Weingartner & Draine (2001b)
H ₂ formation on dust grains	Hollenbach & McKee (1979)
UV pumping of H ₂	Hollenbach & McKee (1979)
H ₂ photodissociation	Black & Dalgarno (1977); Hollenbach & McKee (1979)
Cooling:	
C ⁺ fine structure line	Atomic data – Silva & Viegas (2002) Collisional rates with H – Barinovs et al. (2005) Collisional rates with H ₂ – Wiesenfeld & Goldsmith (2014) ($T < 500\text{K}$), and Glover & Jappsen (2007) ($T > 500\text{K}$)
C fine structure line	Collisional rates with e – Keenan et al. (1986) Atomic data – Silva & Viegas (2002) Collisional rates with H – fit to Abrahamsson et al. (2007) by Draine (2011) Collisional rates with H ₂ – fit to Schroder et al. (1991) by Draine (2011)
O fine structure line	Collisional rates with e – Johnson et al. (1987) Atomic data – Silva & Viegas (2002) Collisional rates with H – fit to Abrahamsson et al. (2007) by Draine (2011) Collisional rates with H ₂ – fit to Jaquet et al. (1992) by Draine (2011)
Ly α line	Collisional rates with e – fit to Bell et al. (1998) Atomic data – Draine (2011) Collisional rates with e – fit to Vrinceanu et al. (2014)
CO rotational lines	Omukai et al. (2010)
H ₂ rotational and vibrational lines	Glover & Abel (2008); Hollenbach & McKee (1979)
Dust thermal emission	Krumholz (2014)
Recombination of e on PAHs	Weingartner & Draine (2001b)
Collisional dissociation of H ₂	Grassi et al. (2014)
Collisional ionization of H	Grassi et al. (2014)

C.2. Chemistry and Temperature

We carry out comparisons similar to Appendix C.1, but here we solve the chemistry and temperature simultaneously, until they both reach equilibrium. The results are shown in Figures 16 and 17. Again, our network agrees well with the PDR code, whereas the NL99 network shows significant disagreement. However, the equilibrium temperature in the NL99 network is very similar to that in our network. For example, at $n = 100 \text{ cm}^{-3}$ and $A_V > 1$, although there is much less CO in the NL99 network, C provides most cooling, resulting in similar equilibrium temperatures. As noted by Glover & Clark (2012a), temperature is insensitive to detailed chemistry, although shielding is important because it sets the photoelectric heating rate.

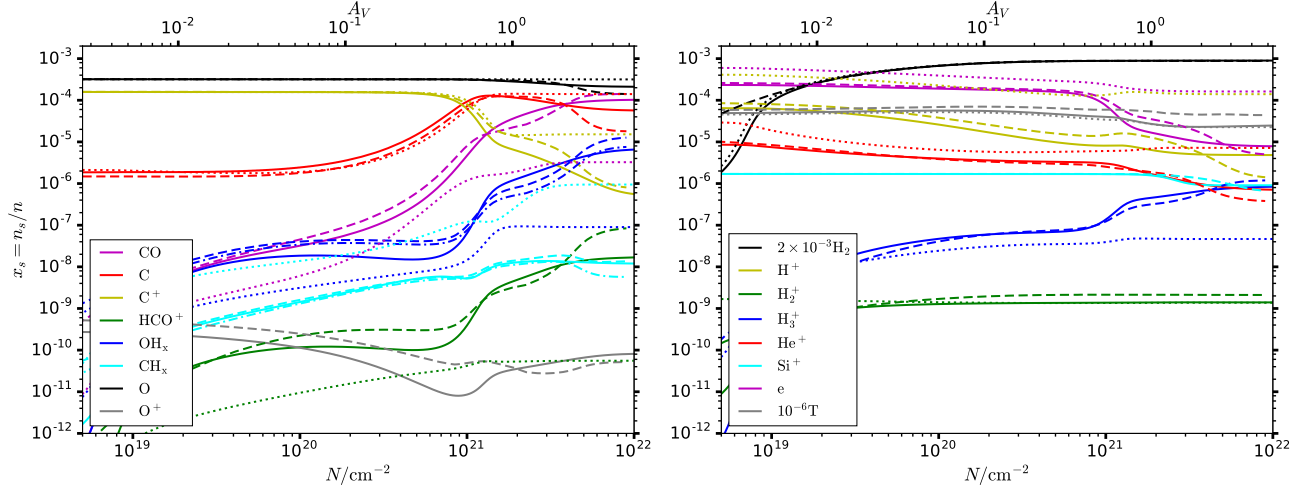
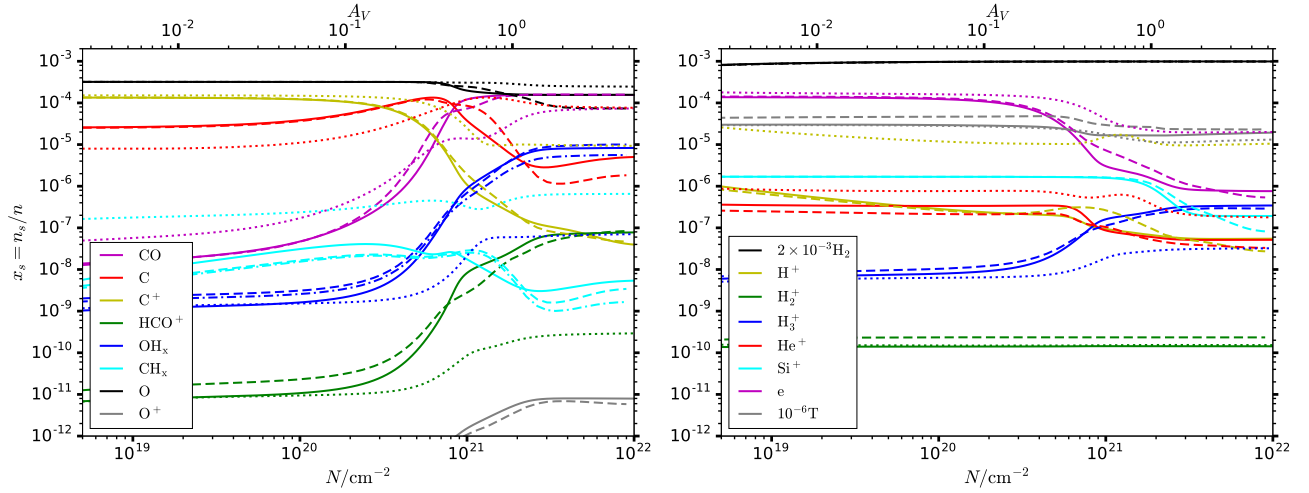
C.3. Comparison at Low Metallicity

Figures 18 and 19 plot comparisons at $Z = 0.1$ between our network and the PDR code. Overall, there is a good agreement. Comparing to $Z = 1$ cases, CO forms at a much higher density $n \gtrsim 1000 \text{ cm}^{-3}$. We note that at $n = 1000 \text{ cm}^{-3}$, our network overproduces CO in shielded regions. This is partly due to the difference in grain-assisted recombination rates, which is discussed in Appendix C.4.

C.4. Grain-assisted Recombination Rates

Ions such H⁺, C⁺, He⁺, and Si⁺ can recombine when they collide with PAHs. The recombination rate on dust grains is often higher than direct recombination with electrons, and therefore can have a major effect on chemistry. We use the results of Weingartner & Draine (2001a) for grain-assisted recombination rates in our network (see Table 2). In Weingartner & Draine (2001a), they assume a certain size distribution of PAHs and calculate the charge distribution on PAHs. The final grain-assisted recombination rates are obtained by averaging over the PAH population. The PDR code uses a slightly different approach in Wolfire et al. (2008). The PAHs are assumed to have a single size, and three charge states, PAH⁺, PAH⁻, and PAH⁰. By comparing with observations, Wolfire et al. (2008) calibrate their grain-assisted recombination rate of C⁺ with the parameter $\phi_{\text{PAH}} = 0.4$.

Figure 20 shows the comparison of the grain-assisted recombination rate of C⁺ between Wolfire et al. (2008) and Weingartner & Draine (2001a). The PAH populations in Wolfire et al. (2008) are assumed to be in charge equilibrium states with reactions described in Appendix C2 of Wolfire et al. (2003), and the total PAH abundance is $n_{\text{PAH}}/n = 2 \times 10^{-7}$. The reaction rate depends mainly on the parameter $\psi = 1.7\chi\sqrt{T}/n_e$, and only has a very weak dependence on temperature. As can be seen in Figure 20, the Wolfire et al. (2008) and Weingartner & Draine (2001a) rates can differ by a factor of ~ 2 . In the main part of this paper, we use 0.6 times the Weingartner & Draine (2001a) rates to match with Wolfire et al. (2008) at $\psi \sim 10^4$. Figure 21 and 22 show comparisons with the original Weingartner & Draine (2001a) rates. At $n = 100 \text{ cm}^{-3}$, The abundances of CO, OH_x, HCO⁺, and He⁺ can change by a factor of ~ 5 around $A_V \sim 1$, but the chemical abundances at higher density $n = 1000 \text{ cm}^{-3}$ are largely unaffected.

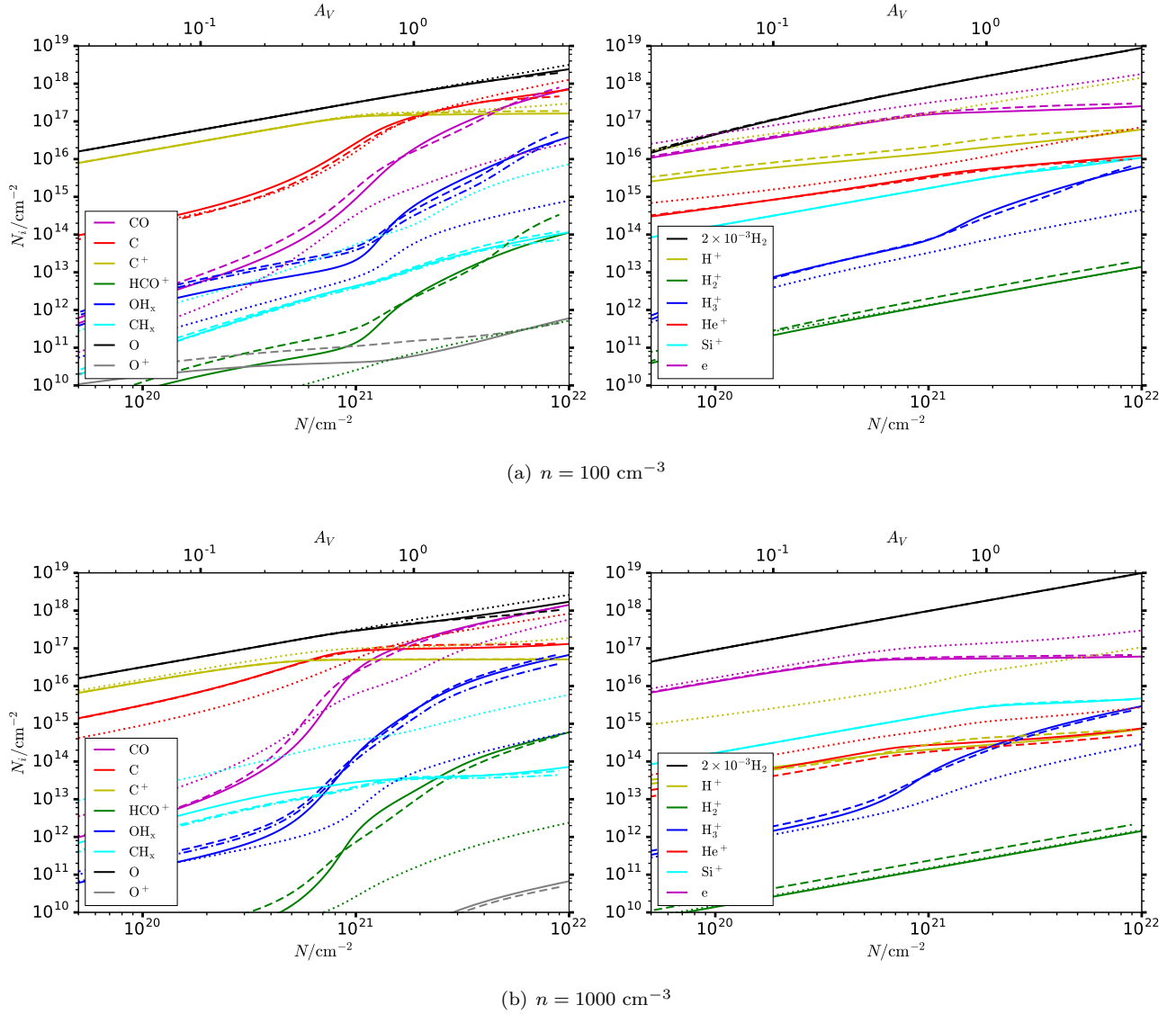
(a) $n = 100 \text{ cm}^{-3}$ (b) $n = 1000 \text{ cm}^{-3}$ **Figure 16.** Abundances of species, similar to Figure 12 and 14, but for temperature in thermal equilibrium.

C.5. Grain Surface Reactions

In addition to the grain-assisted recombinations, dust grains can also affect the gas-phase chemistry by grain surface reactions (Hollenbach et al. 2009). This includes the formation of OH and H₂O on the surface of dust grains, and the freeze-out of molecules such as CO and H₂O on dust grains in cold and shielded regions. Figures 23 and 24 show the comparisons of the chemical abundances with and without the grain surface reactions. The formation of OH and H₂O on grains results in a higher OH_x and CO abundances at $n = 1000 \text{ cm}^{-3}$ and $A_V < 1$. The freeze-out can greatly reduce the abundances of CO and other species at $A_V \gtrsim 2$. Since the CO abundance is still low in regions that are affected by the formation of OH and H₂O on grains, and the freeze-out depends on the grain size distribution, which is very uncertain in dense and shielded clouds, we do not include grain surface reaction in our network. Ideally, the effect of freeze-out on carbon bearing species should be calibrated with observations of diffuse and dense clouds as was done with oxygen-bearing species in Hollenbach et al. (2009, 2012) and Sonnentrucker et al. (2015).

C.6. Comparison with the PyPDR code

Figure 25 shows a comparison between our chemical network and the *PyPDR* code. We disabled the grain-assisted recombination of ions in our network to make a direct comparison with *PyPDR*, which does not have these reactions. We also updated the reaction rates in the *PyPDR* code, to be consistent with the reaction rates in this paper (Tables 1 and 2). Note that *PyPDR* does not include metals such as Si, which is in our network. Figure 25 shows that our chemical network (without grain-assisted recombination) agrees very well with the results from the *PyPDR* code.

(a) $n = 100 \text{ cm}^{-3}$ (b) $n = 1000 \text{ cm}^{-3}$ **Figure 17.** Integrated column densities of species in Figure 16.

D. CHARACTERISTIC DENSITY IN SLAB AND SPHERICAL TURBULENT CLOUDS

Define $s \equiv \ln(\rho/\rho_0)$, where $\rho_0 = M/V = \langle \rho \rangle_V$ is the volume-weighted density. Both the volume- and the mass-weighted density obey the log-normal distribution

$$f_{V,M}(s)ds = \frac{1}{\sigma_s \sqrt{2\pi}} \exp\left[-\frac{(s - \mu_{V,M})^2}{2\sigma_s^2}\right] ds, \quad (\text{D1})$$

where $\mu_V = -\sigma_s^2/2$ and $\mu_M = \sigma_s^2/2$ are the volume- and mass-weighted means of the parameter s . Both observations of molecular clouds and numerical simulations show that the variance σ_s is related to the turbulence Mach number \mathcal{M} (e.g., Padoan et al. 1997; Lemaster & Stone 2008; Brunt 2010; Kainulainen & Tan 2013)

$$\sigma_s \approx \ln(1 + b^2 \mathcal{M}^2), \quad (\text{D2})$$

with $b \approx 1/2 - 1/3$. Thus, the mass-weighted mean density is

$$\left\langle \frac{\rho}{\rho_0} \right\rangle_M = \int \frac{\rho}{\rho_0} f_M(s) ds = \int e^s f(s) ds = e^{\sigma_s^2} \approx 1 + b^2 \mathcal{M}^2. \quad (\text{D3})$$

For slab clouds, the balance of the gas self-gravity with the mid-plane pressure P (assumed to be primarily from turbulence) gives

$$P = \frac{\pi G \Sigma^2}{2}, \quad (\text{D4})$$

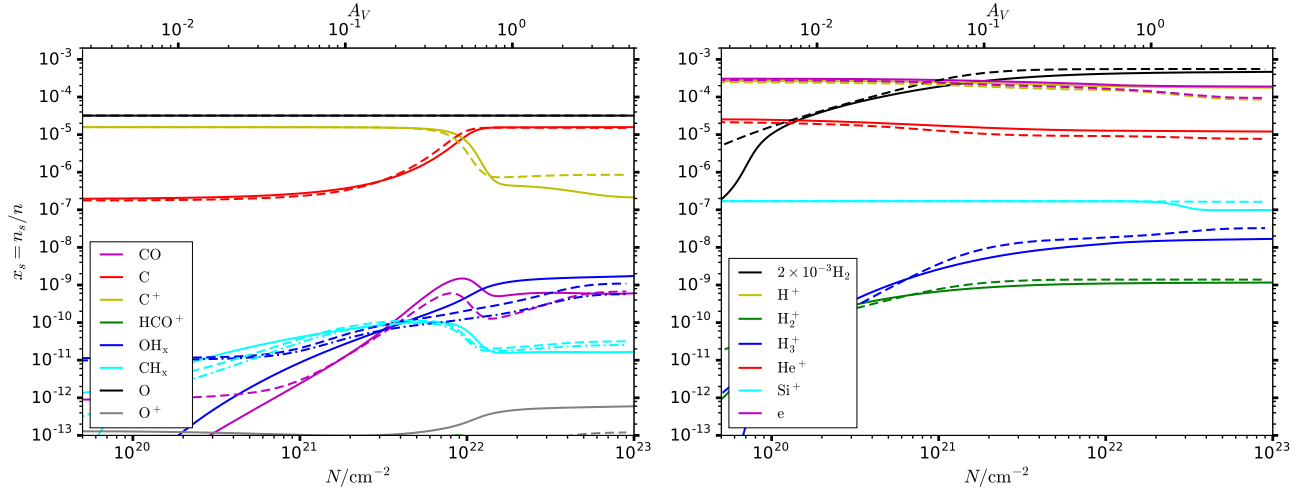
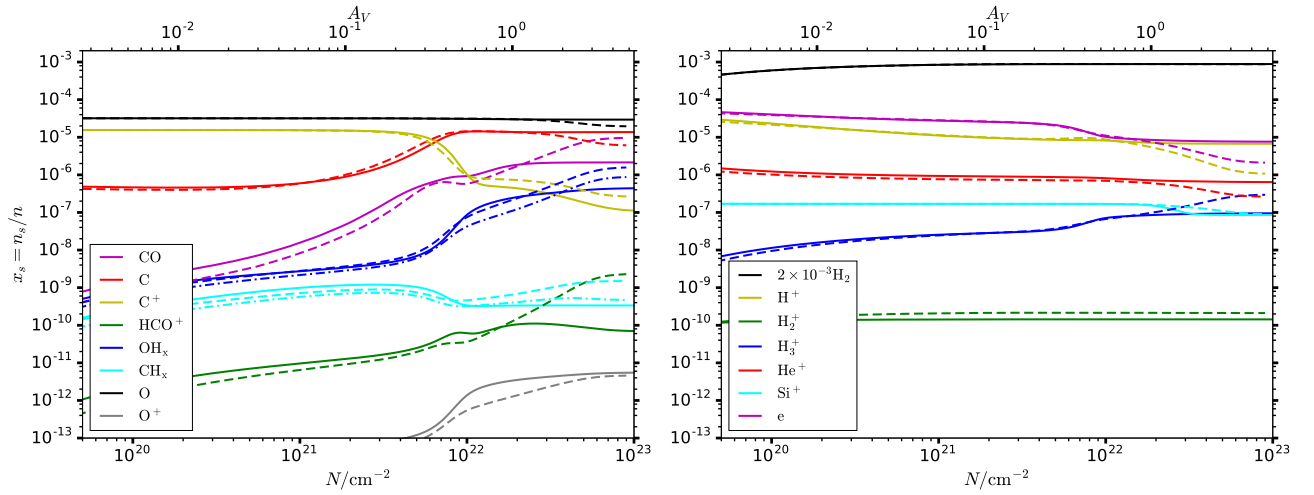
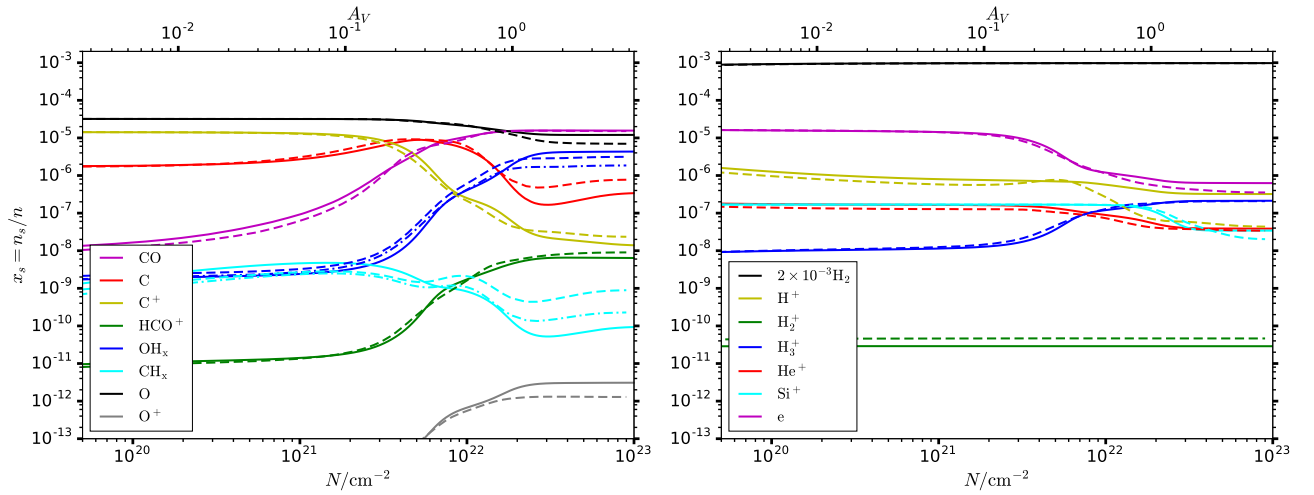
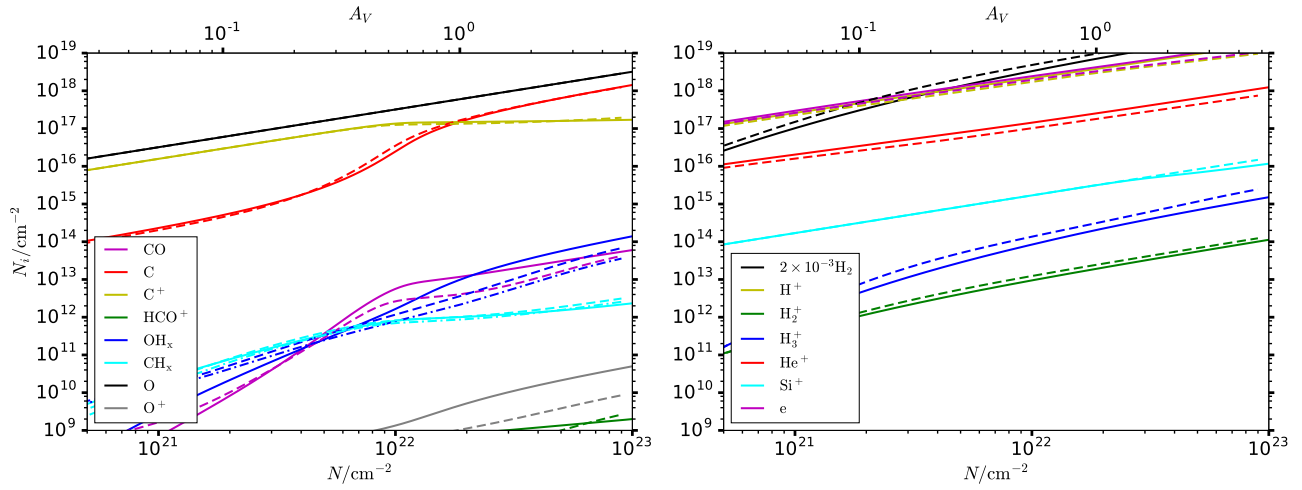
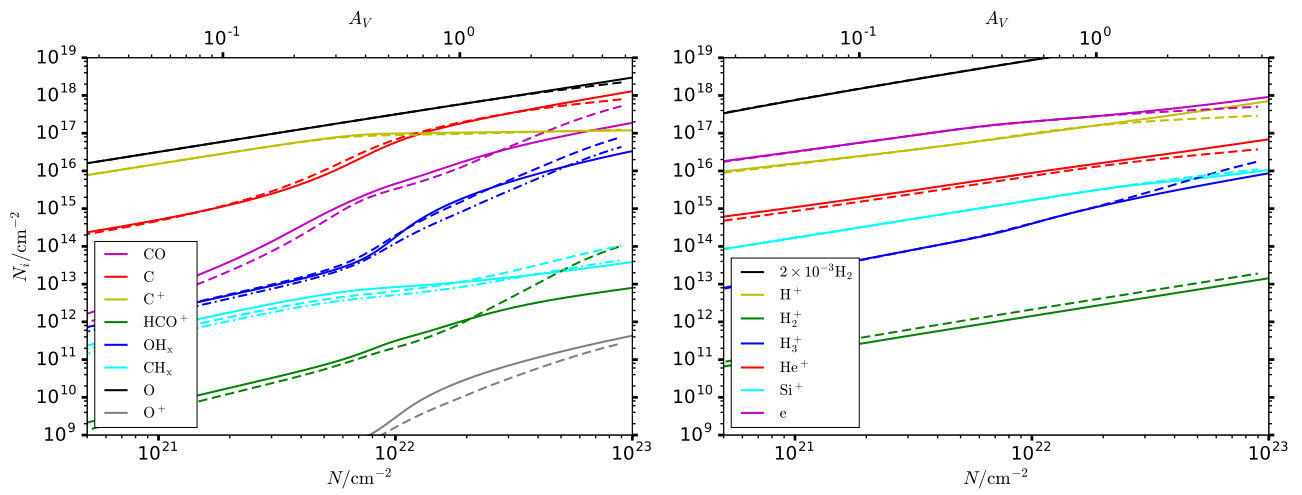
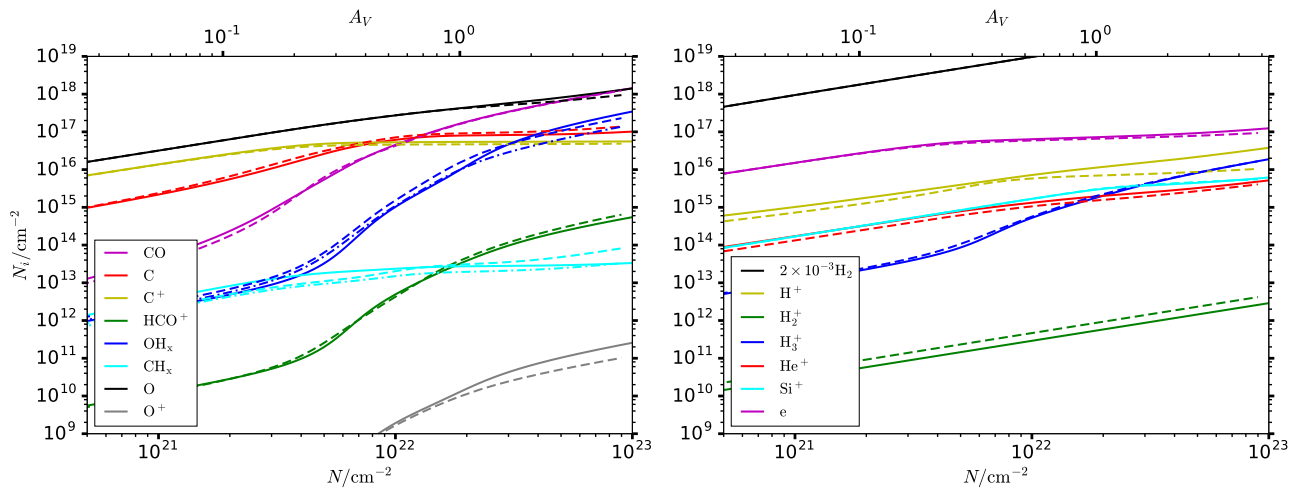
(a) $n = 100 \text{ cm}^{-3}$ (b) $n = 1000 \text{ cm}^{-3}$ (c) $n = 5000 \text{ cm}^{-3}$

Figure 18. Abundances of species, similar to Figures 12 and 14, but for $Z = 0.1$. Note that the NL99 network is not shown here.

(a) $n = 100 \text{ cm}^{-3}$ (b) $n = 1000 \text{ cm}^{-3}$ (c) $n = 5000 \text{ cm}^{-3}$ **Figure 19.** Integrated column densities of species in Figure 18.

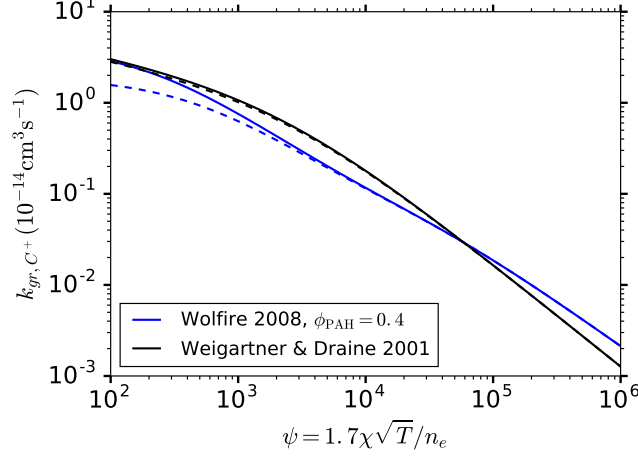


Figure 20. Comparison of the grain-assisted recombination rate of C^+ between Wolfire et al. (2008) (blue) and Weingartner & Draine (2001a) (black). The solid and dashed lines are results with $T = 20$ K and $T = 100$ K. The temperature T is in Kelvin, and the electron density n_e is in cm^{-3} in ψ .

where Σ is the gas surface density. The average volume-weighted density is then $\rho_0 \equiv P/\sigma_{1D}^2 = \pi G \Sigma^2 / (2\sigma_{1D}^2)$, where σ_{1D} is the one-dimensional velocity dispersion of the cloud-scale turbulence. The Mach number squared

$$\mathcal{M}^2 = \frac{\sigma_{3D}^2}{c_s^2} = \frac{3\pi G \Sigma^2}{2\rho_0 c_s^2}, \quad (\text{D5})$$

where c_s is the sound speed. Therefore, according to Equation (D3), the mass-weighted mean density of the slab cloud can be written as

$$\langle \rho \rangle_{M,\text{slab}} = \rho_0 + b^2 \mathcal{M}^2 \rho_0 = \rho_0 + 3b^2 \left(\frac{\pi G \Sigma^2}{2c_s^2} \right). \quad (\text{D6})$$

For uniform spherical clouds, the virial parameter

$$\alpha_{\text{vir}} \equiv \frac{2E_k}{|E_G|} = \frac{5\sigma_{1D}^2 R}{GM}, \quad (\text{D7})$$

where E_k is the kinetic energy of the cloud from turbulence and E_G is the gravitational energy. A virialized cloud has $\alpha_{\text{vir}} = 1$, and marginally gravitationally bound cloud has $\alpha_{\text{vir}} = 2$. The Mach number squared can be written as

$$\mathcal{M}^2 = \frac{\sigma_{3D}^2}{c_s^2} = \frac{3\sigma_{1D}^2}{c_s^2} = \frac{3\alpha_{\text{vir}} GM}{5Rc_s^2} = \frac{1}{\rho_0} \alpha_{\text{vir}} \frac{9}{10} \left(\frac{\pi G \Sigma^2}{2c_s^2} \right). \quad (\text{D8})$$

Here we define the average cloud density $\rho_0 \equiv M / (\frac{4\pi}{3} R^3)$, and the average cloud surface density $\Sigma \equiv M / (\pi R^2)$. Similar to Equation (D6), the mass-weighted mean density of the spherical cloud is given by

$$\langle \rho \rangle_{M,\text{sphere}} = \rho_0 + b^2 \mathcal{M}^2 \rho_0 = \rho_0 + \left(\frac{9}{10} \alpha_{\text{vir}} \right) b^2 \left(\frac{\pi G \Sigma^2}{2c_s^2} \right). \quad (\text{D9})$$

Equations (D6) and (D9) can be written together as

$$\langle \rho \rangle_M = \rho_0 + ab^2 \left(\frac{\pi G \Sigma^2}{2c_s^2} \right), \quad (\text{D10})$$

where $a = 3$ for slab clouds and $a = 9\alpha_{\text{vir}}/10$ for spherical clouds. Using the relations $\rho = 1.4m_{\text{H}}n$ and $\Sigma = 1.4m_{\text{H}}N$, where $m_{\text{H}} = 1.67 \times 10^{-24}$ g is the mass of a hydrogen atom, and the factor 1.4 comes from helium, Equation (D10) gives

$$\langle n \rangle_M = \langle n \rangle_V + 1.4m_{\text{H}}ab^2 \left(\frac{\pi GN^2}{2c_s^2} \right). \quad (\text{D11})$$

E. ADDITIONAL PLOTS FOR COMPARISON WITH OBSERVATIONS OF DIFFUSE AND TRANSLUCENT CLOUDS

Figure 26 shows a detailed comparison between observations and our slab model with no grain-assisted recombination, and depletion of carbon abundance.

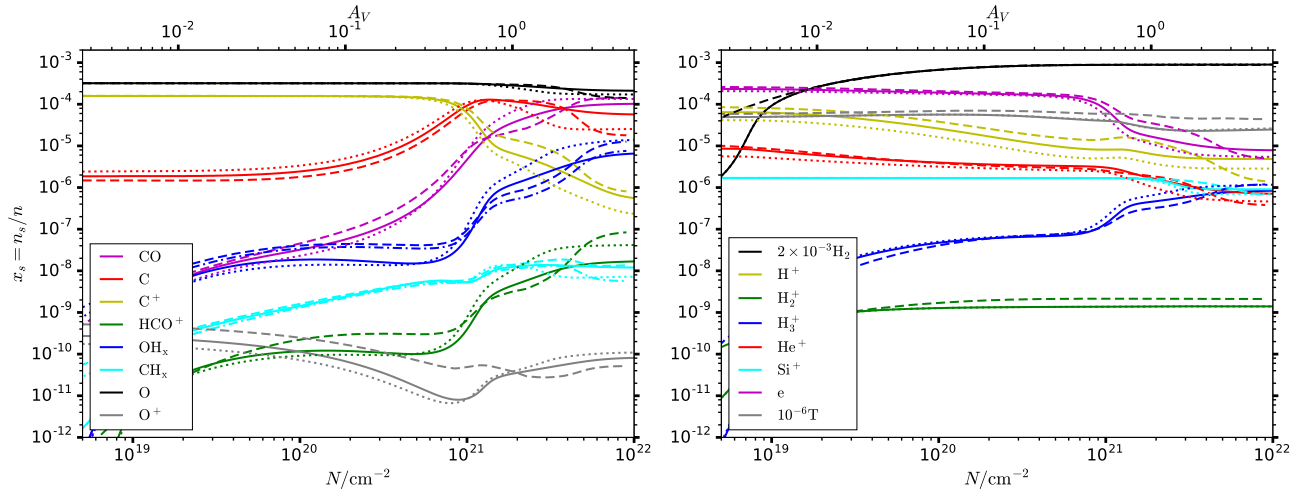
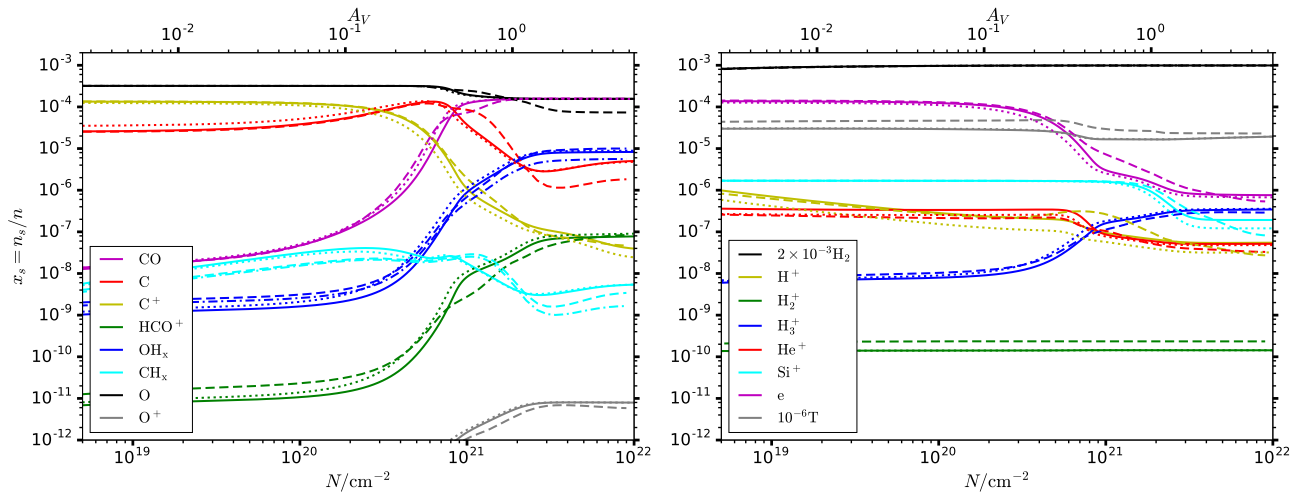
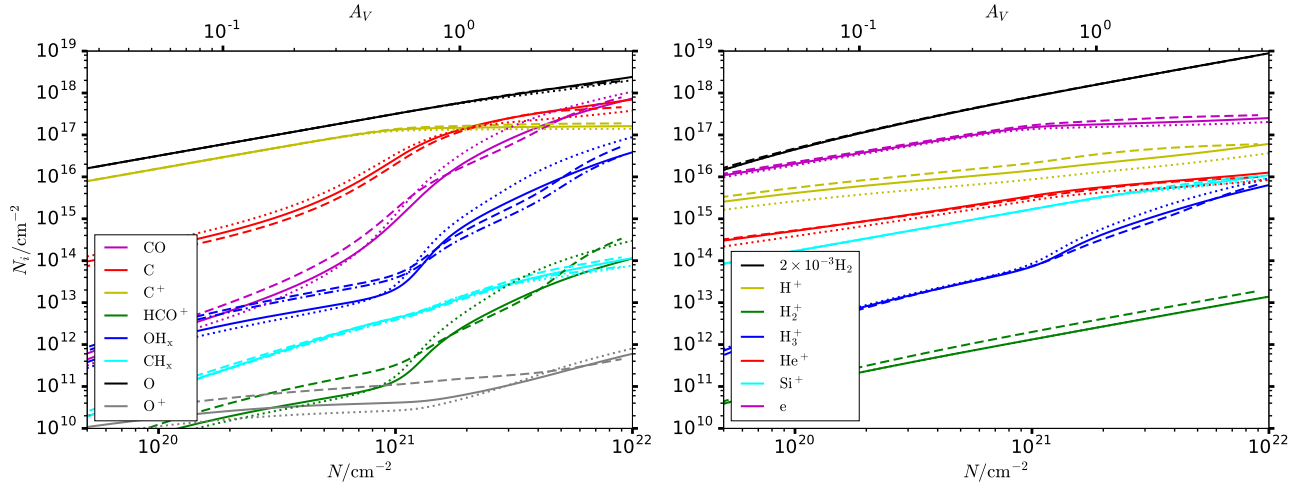
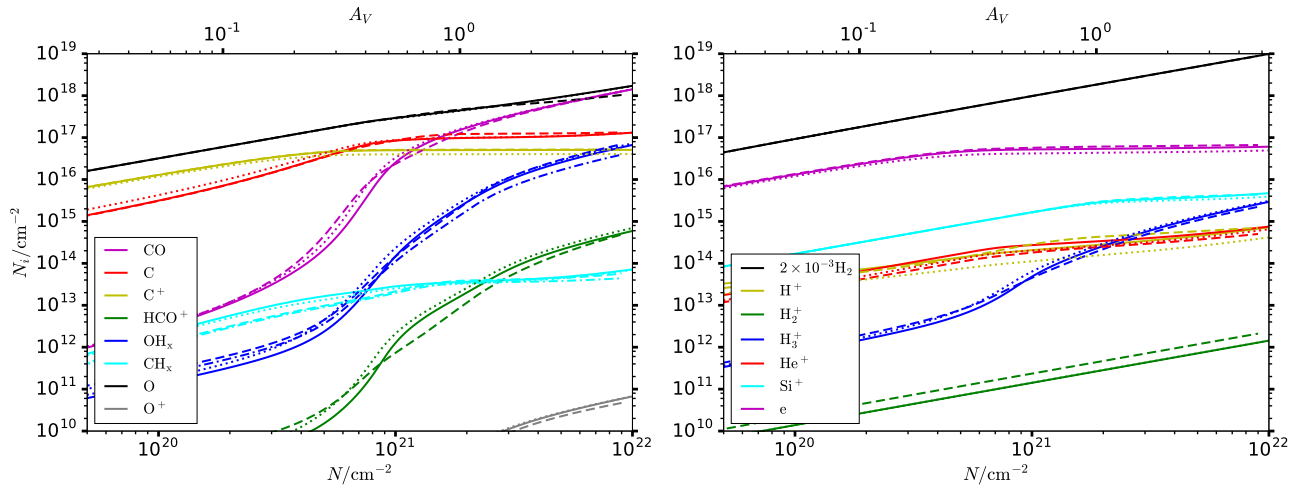
(a) $n = 100 \text{ cm}^{-3}$ (b) $n = 1000 \text{ cm}^{-3}$

Figure 21. Comparison of chemical abundances in our network with 0.6 times the grain-assisted recombination rates in Weingartner & Draine (2001a) (solid), the original Weingartner & Draine (2001a) rates (dotted), and the PDR code (dashed). The temperature is in thermal equilibrium.

(a) $n = 100 \text{ cm}^{-3}$ (b) $n = 1000 \text{ cm}^{-3}$ **Figure 22.** Integrated column densities of species in Figure 21.

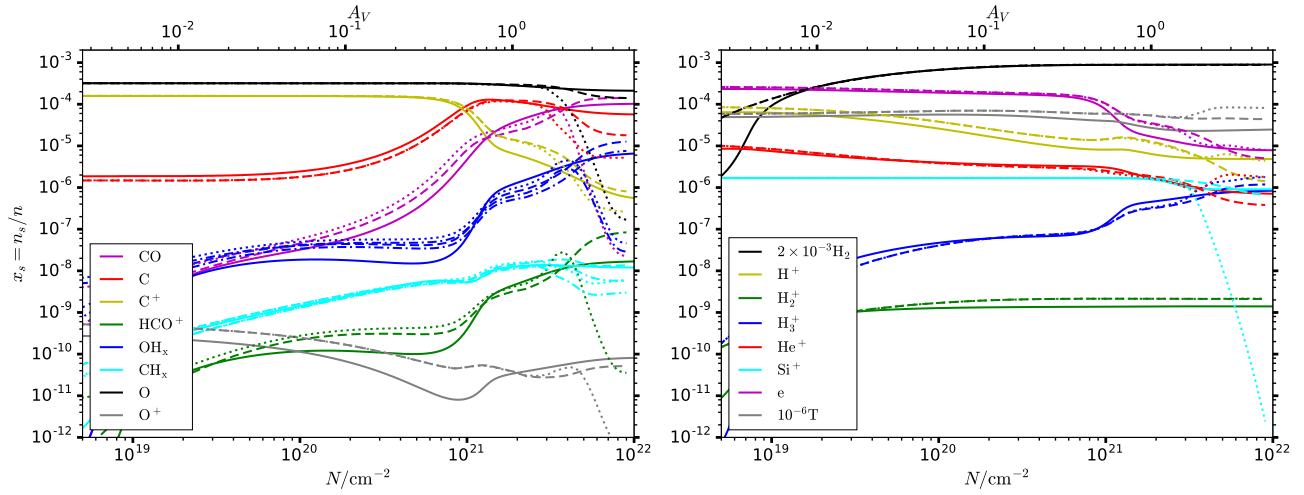
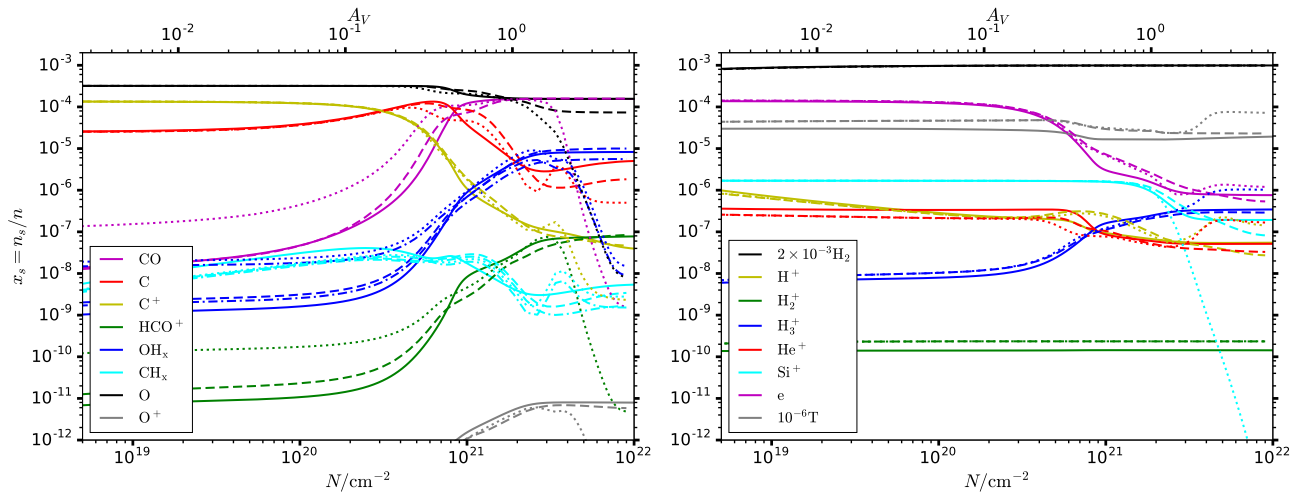
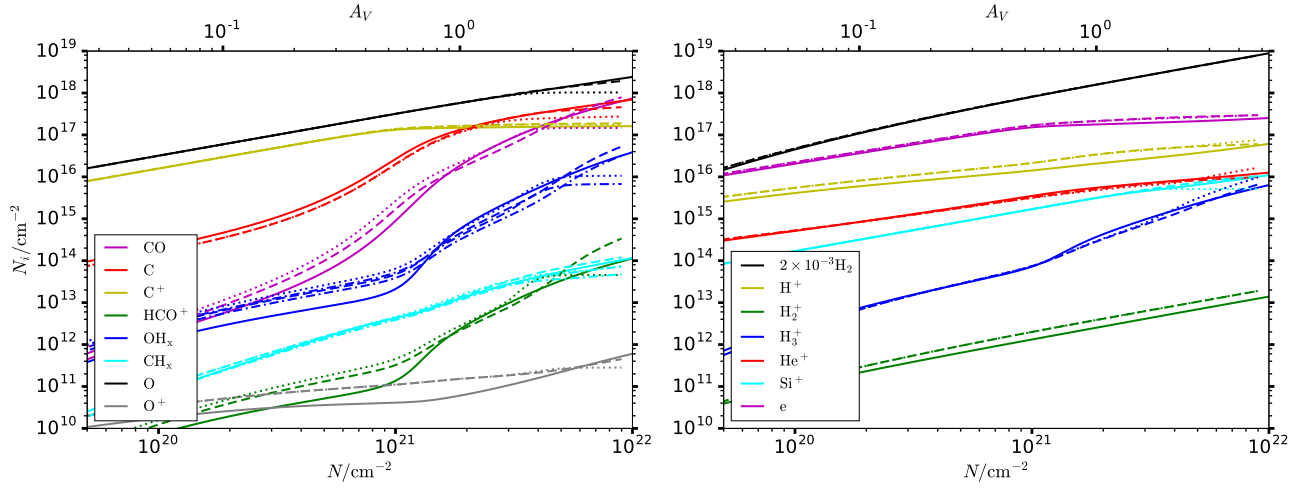
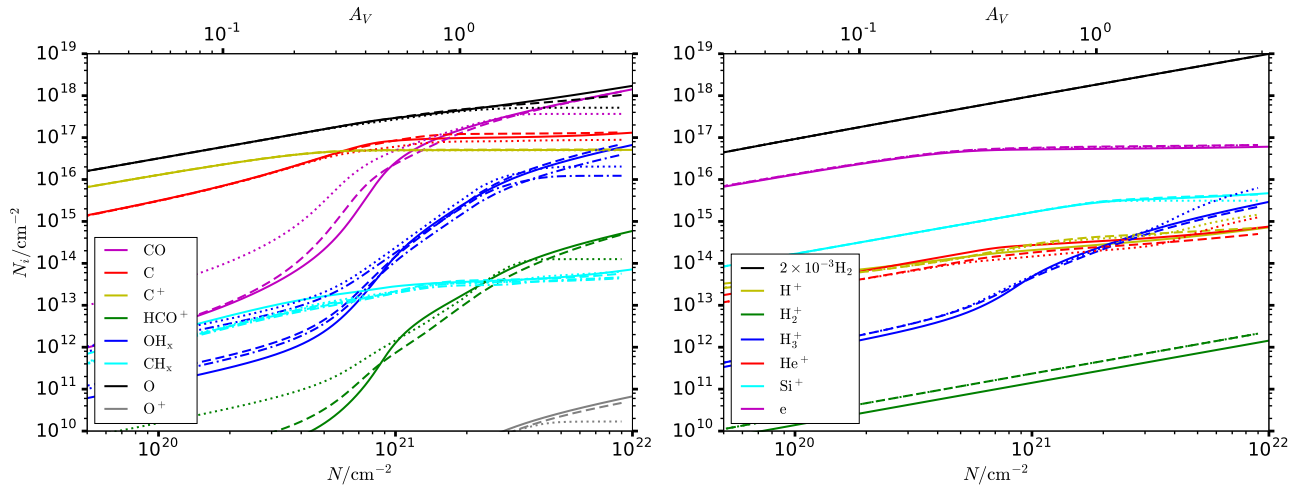
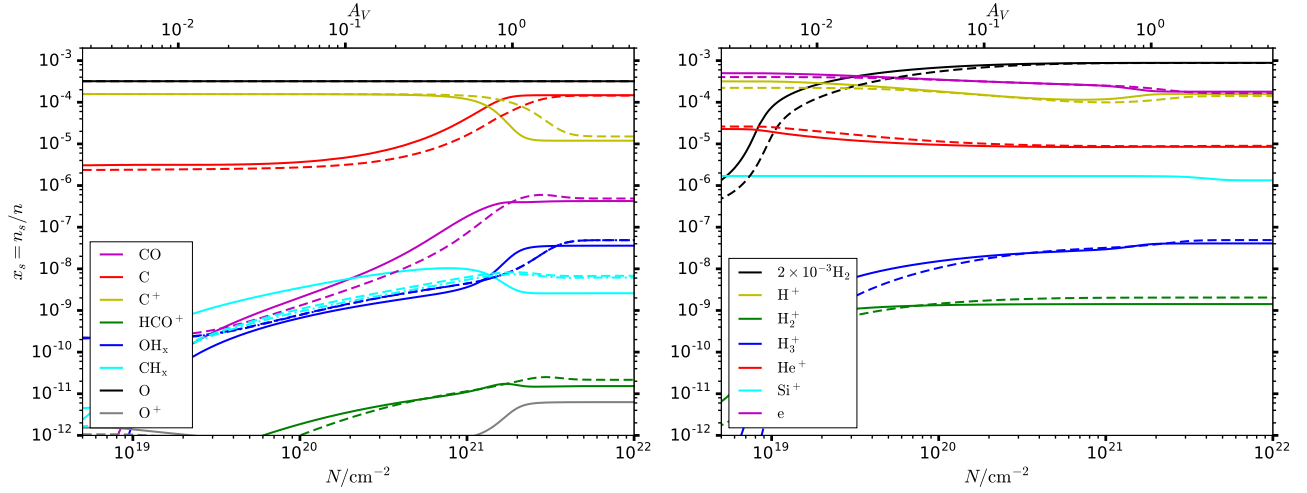
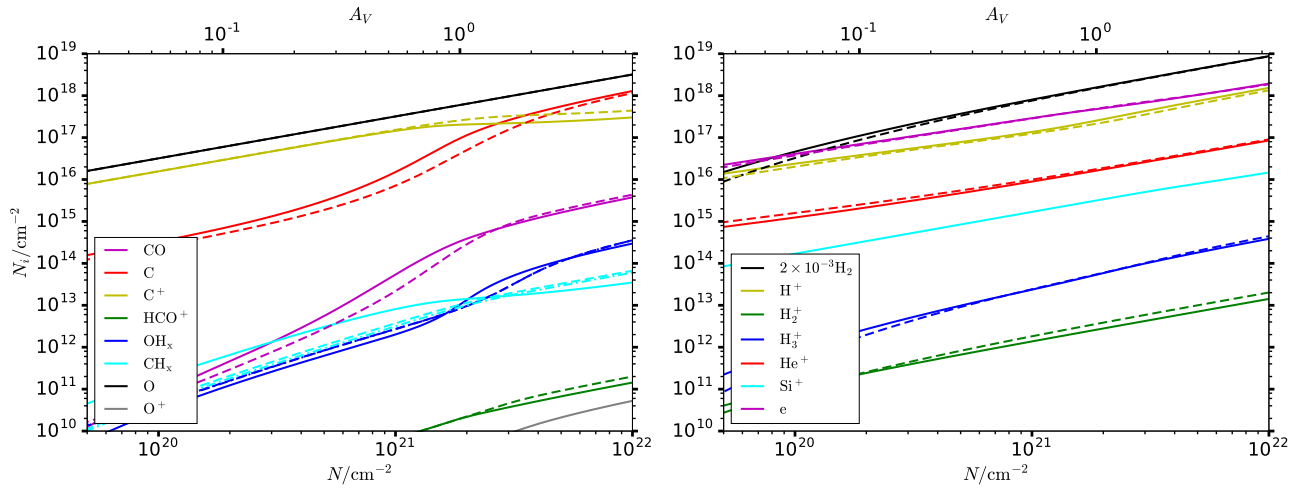
(a) $n = 100 \text{ cm}^{-3}$ (b) $n = 1000 \text{ cm}^{-3}$

Figure 23. Comparison of chemical abundances in our network (solid), the PDR code (dashed), and the PDR code with grain surface reactions in Hollenbach et al. (2009) (dotted). The temperature is in thermal equilibrium.

(a) $n = 100 \text{ cm}^{-3}$ (b) $n = 1000 \text{ cm}^{-3}$ **Figure 24.** Integrated column densities of species in Figure 23.



(a) Abundances



(b) Column densities

Figure 25. Abundances and column densities of species at density $n = 100 \text{ cm}^{-3}$ in our network (solid), and the *PyPDR* code (dashed), as a function of A_V/N . This is similar to Figures 12 and 13, but with the dashed lines showing the *PyPDR* code instead of the *Wolfire PDR* code. We have also plotted the abundances of CH and OH species from the *PyPDR* code (cyan and blue dash-dotted lines), in addition to the sum of all CH_x and OH_x species. The cosmic-ray ionization rate $\xi_{\text{H}} = 2 \times 10^{-16} \text{ s}^{-1} \text{H}^{-1}$, and gas temperature is fixed at $T = 20 \text{ K}$. The reactions of grain-assisted recombination of ions are excluded in our network to be consistent with *PyPDR*.

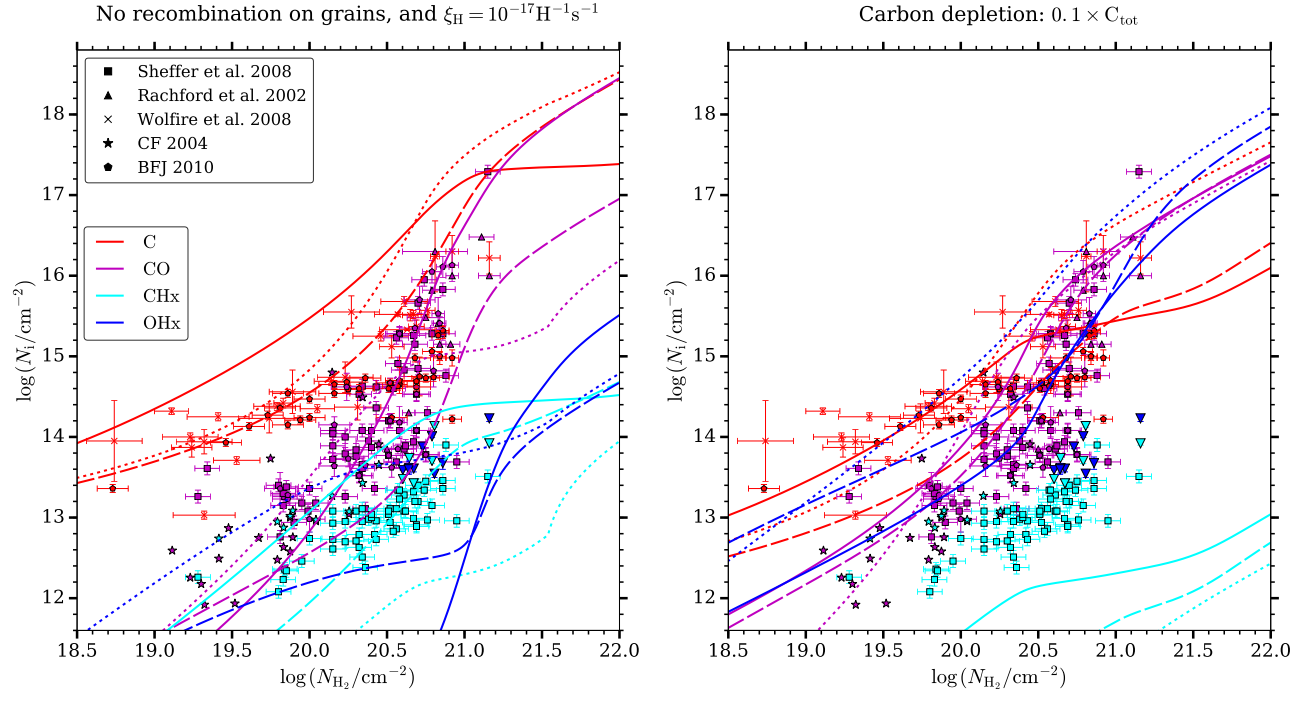


Figure 26. Similar to the right panel of Figure 10, but with no grain-assisted recombination of ions (*left*), or depletion of gas-phase carbon abundance by a factor of 10 (*right*).

REFERENCES

- Abrahamsson, E., Krems, R. V., & Dalgarno, A. 2007, *ApJ*, 654, 1171
- Acharyya, K., Fuchs, G. W., Fraser, H. J., van Dishoeck, E. F., & Linnartz, H. 2007, *A&A*, 466, 1005
- Anicich, V. G., & Huntress, Jr., W. T. 1986, *ApJS*, 62, 553
- Ao, Y., Henkel, C., Menten, K. M., et al. 2013, *A&A*, 550, A135
- Badnell, N. R. 2006, *ApJS*, 167, 334
- Badnell, N. R., O’Mullane, M. G., Summers, H. P., et al. 2003, *A&A*, 406, 1151
- Bally, J., & Hi-GAL Team. 2014, in *IAU Symposium*, Vol. 303, *The Galactic Center: Feeding and Feedback in a Normal Galactic Nucleus*, ed. L. O. Sjouwerman, C. C. Lang, & J. Ott, 1–14
- Barinova, G., van Hemert, M. C., Krems, R., & Dalgarno, A. 2005, *ApJ*, 620, 537
- Barlow, S. E. 1984, PhD thesis, UNIVERSITY OF COLORADO AT BOULDER.
- Bell, K. L., Berrington, K. A., & Thomas, M. R. J. 1998, *MNRAS*, 293, L83
- Bensch, F., Leuhenhagen, U., Stutzki, J., & Schieder, R. 2003, *ApJ*, 591, 1013
- Bergin, E. A., Langer, W. D., & Goldsmith, P. F. 1995, *ApJ*, 441, 222
- Bialy, S., Bihl, S., Beuther, H., Henning, T., & Sternberg, A. 2017, *ApJ*, 835, 126
- Bialy, S., & Sternberg, A. 2016, *ApJ*, 822, 83
- Bialy, S., Sternberg, A., Lee, M.-Y., Le Petit, F., & Roueff, E. 2015, *ApJ*, 809, 122
- Bigiel, F., Leroy, A., Walter, F., et al. 2008, *AJ*, 136, 2846
- Bigiel, F., Leroy, A. K., Walter, F., et al. 2011, *ApJ*, 730, L13
- Bisbas, T. G., Papadopoulos, P. P., & Viti, S. 2015, *ApJ*, 803, 37
- Black, J. H., & Dalgarno, A. 1977, *ApJS*, 34, 405
- Bohlin, R. C., Savage, B. D., & Drake, J. F. 1978, *ApJ*, 224, 132
- Bolatto, A. D., Leroy, A. K., Rosolowsky, E., Walter, F., & Blitz, L. 2008, *ApJ*, 686, 948
- Bolatto, A. D., Wolfire, M., & Leroy, A. K. 2013, *ARA&A*, 51, 207
- Bonnor, W. B. 1956, *MNRAS*, 116, 351
- Brunt, C. M. 2010, *A&A*, 513, A67
- Bryans, P., Kreckel, H., Roueff, E., Wakelam, V., & Savin, D. W. 2009, *ApJ*, 694, 286
- Burgh, E. B., France, K., & Jenkins, E. B. 2010, *ApJ*, 708, 334
- Burgh, E. B., France, K., & McCandliss, S. R. 2007, *ApJ*, 658, 446
- Burton, M. G., Ashley, M. C. B., Braiding, C., et al. 2015, *ApJ*, 811, 13
- Cardelli, J. A., Sofia, U. J., Savage, B. D., Keenan, F. P., & Dufton, P. L. 1994, *ApJ*, 420, L29
- Carty, D., Goddard, A., Köhler, S. P. K., Sims, I. R., & Smith, I. W. M. 2006, *The Journal of Physical Chemistry A*, 110, 3101, pMID: 16509632
- Clark, P. C., & Glover, S. C. O. 2015, *MNRAS*, 452, 2057
- Cohen, S. D., Hindmarsh, A. C., & Dubois, P. F. 1996, *Computers in Physics*, 10
- Crenny, T., & Federman, S. R. 2004, *ApJ*, 605, 278
- Dalgarno, A., & McCray, R. A. 1972, *ARA&A*, 10, 375
- Dalgarno, A., Yan, M., & Liu, W. 1999, *ApJS*, 125, 237
- de Ruetete, N., Miller, K. A., O’Connor, A. P., et al. 2015, *ArXiv e-prints*, arXiv:1508.07882
- Dobbs, C. L., Krumholz, M. R., Ballesteros-Paredes, J., et al. 2014, *Protostars and Planets VI*, 3
- Draine, B. T. 1978, *ApJS*, 36, 595
- . 2003, *ApJ*, 598, 1017
- . 2011, *Physics of the Interstellar and Intergalactic Medium*
- Draine, B. T., & Bertoldi, F. 1996, *ApJ*, 468, 269
- Ebert, R. 1955, *ZAp*, 37, 217
- Elmegreen, B. G. 1993, *ApJ*, 411, 170
- Ferland, G. J., Peterson, B. M., Horne, K., Welsh, W. F., & Nahar, S. N. 1992, *ApJ*, 387, 95
- Genzel, R., Tacconi, L. J., Gracia-Carpio, J., et al. 2010, *MNRAS*, 407, 2091
- Geppert, W. D., Thomas, R. D., Ehlerding, A., et al. 2005, *Journal of Physics Conference Series*, 4, 26
- Girichidis, P., Walch, S., Naab, T., et al. 2016, *MNRAS*, 456, 3432
- Glassgold, A. E., Galli, D., & Padovani, M. 2012, *ApJ*, 756, 157
- Glassgold, A. E., & Langer, W. D. 1974, *ApJ*, 193, 73
- Glover, S. C. O., & Abel, T. 2008, *MNRAS*, 388, 1627
- Glover, S. C. O., & Clark, P. C. 2012a, *MNRAS*, 421, 116
- . 2012b, *MNRAS*, 421, 9
- . 2012c, *MNRAS*, 426, 377
- . 2016, *MNRAS*, 456, 3596
- Glover, S. C. O., Federrath, C., Mac Low, M.-M., & Klessen, R. S. 2010, *MNRAS*, 404, 2
- Glover, S. C. O., & Jappsen, A.-K. 2007, *ApJ*, 666, 1
- Glover, S. C. O., & Mac Low, M.-M. 2007, *ApJS*, 169, 239
- Godard, B., Falgarone, E., & Pineau des Forêts, G. 2014, *A&A*, 570, A27
- Goldsmith, P. F. 2001, *ApJ*, 557, 736
- . 2013, *ApJ*, 774, 134
- Goldsmith, P. F., & Langer, W. D. 1978, *ApJ*, 222, 881
- Grassi, T., Bovino, S., Schleicher, D. R. G., et al. 2014, *MNRAS*, 439, 2386
- Gredel, R., Lepp, S., & Dalgarno, A. 1987, *ApJ*, 323, L137
- Gredel, R., Lepp, S., Dalgarno, A., & Herbst, E. 1989, *ApJ*, 347, 289
- Güsten, R., & Philipp, S. D. 2004, in *The Dense Interstellar Medium in Galaxies*, ed. S. Pfalzner, C. Kramer, C. Staubmeier, & A. Heithausen, Vol. 91, 253
- Habing, H. J. 1968, *Bull. Astron. Inst. Netherlands*, 19, 421
- Heays, A. N., Bosman, A. D., & van Dishoeck, E. F. 2017, *ArXiv e-prints*, arXiv:1701.04459
- Heiles, C., & Troland, T. H. 2003, *ApJ*, 586, 1067
- Heyer, M., & Dame, T. M. 2015, *ARA&A*, 53, 583
- Heyer, M. H., & Brunt, C. M. 2004, *ApJ*, 615, L45
- Hollenbach, D., Kaufman, M. J., Bergin, E. A., & Melnick, G. J. 2009, *ApJ*, 690, 1497
- Hollenbach, D., Kaufman, M. J., Neufeld, D., Wolfire, M., & Goicoechea, J. R. 2012, *ApJ*, 754, 105
- Hollenbach, D., & McKee, C. F. 1979, *ApJS*, 41, 555
- Hummer, D. G., & Storey, P. J. 1998, *MNRAS*, 297, 1073
- Hunt, L. K., García-Burillo, S., Casasola, V., et al. 2015, *A&A*, 583, A114
- Indriolo, N., Geballe, T. R., Oka, T., & McCall, B. J. 2007, *ApJ*, 671, 1736
- Indriolo, N., Neufeld, D. A., Gerin, M., et al. 2015, *ApJ*, 800, 40
- Jameson, K. E., Bolatto, A. D., Leroy, A. K., et al. 2015, *ArXiv e-prints*, arXiv:1510.08084
- Janev, R. K., Langer, W. D., & Evans, K. 1987, *Elementary processes in Hydrogen-Helium plasmas - Cross sections and reaction rate coefficients*
- Jaquet, R., Staemmler, V., Smith, M. D., & Flower, D. R. 1992, *Journal of Physics B Atomic Molecular Physics*, 25, 285
- Jenkins, E. B. 2009, *ApJ*, 700, 1299
- Jenkins, E. B., & Tripp, T. M. 2011, *ApJ*, 734, 65
- Johnson, C. T., Burke, P. G., & Kingston, A. E. 1987, *Journal of Physics B Atomic Molecular Physics*, 20, 2553
- Kainulainen, J., & Tan, J. C. 2013, *A&A*, 549, A53
- Kaufman, M. J., Wolfire, M. G., & Hollenbach, D. J. 2006, *ApJ*, 644, 283
- Kaufman, M. J., Wolfire, M. G., Hollenbach, D. J., & Luhman, M. L. 1999, *ApJ*, 527, 795
- Keenan, F. P., Lennon, D. J., Johnson, C. T., & Kingston, A. E. 1986, *MNRAS*, 220, 571
- Kennicutt, R. C., & Evans, N. J. 2012, *ARA&A*, 50, 531
- Keto, E., & Caselli, P. 2008, *ApJ*, 683, 238
- Kim, C.-G., Kim, W.-T., & Ostriker, E. C. 2011, *ApJ*, 743, 25
- Kim, C.-G., Ostriker, E. C., & Kim, W.-T. 2013, *ApJ*, 776, 1
- Kim, J. K., Theard, L. P., & Huntress, Jr., W. T. 1975, *Chemical Physics Letters*, 32, 610
- Krumholz, M. R. 2014, *MNRAS*, 437, 1662
- Krumholz, M. R., Leroy, A. K., & McKee, C. F. 2011, *ApJ*, 731, 25
- Krumholz, M. R., McKee, C. F., & Tumlinson, J. 2009, *ApJ*, 693, 216
- Larson, R. B. 1981, *MNRAS*, 194, 809
- Le Petit, F., Nehmé, C., Le Bourlot, J., & Roueff, E. 2006, *ApJS*, 164, 506
- Le Teuff, Y. H., Millar, T. J., & Markwick, A. J. 2000, *A&AS*, 146, 157
- Lee, M.-Y., Stanimirović, S., Wolfire, M. G., et al. 2014, *ApJ*, 784, 80
- Lemaster, M. N., & Stone, J. M. 2008, *ApJ*, 682, L97
- Lepp, S., & Shull, J. M. 1983, *ApJ*, 270, 578

- Leroy, A., Cannon, J., Walter, F., Bolatto, A., & Weiss, A. 2007, *ApJ*, 663, 990
- Leroy, A. K., Walter, F., Brinks, E., et al. 2008, *AJ*, 136, 2782
- Leung, C. M., Herbst, E., & Huebner, W. F. 1984, *ApJS*, 56, 231
- Linder, F., Janev, R. K., & Botero, J. 1995, in *Atomic and Molecular Processes in Fusion Edge Plasmas*, ed. R. K. Janev, 397
- Liszt, H. S. 2011, *A&A*, 527, A45
- Mac Low, M.-M., & Klessen, R. S. 2004, *Reviews of Modern Physics*, 76, 125
- Mac Low, M.-M., & Shull, J. M. 1986, *ApJ*, 302, 585
- Magnani, L., Blitz, L., & Mundy, L. 1985, *ApJ*, 295, 402
- Martin, P. G., Keogh, W. J., & Mandy, M. E. 1998, *ApJ*, 499, 793
- Martin, P. G., Schwarz, D. H., & Mandy, M. E. 1996, *ApJ*, 461, 265
- McCall, B. J., Huneycutt, A. J., Saykally, R. J., et al. 2004, *Phys. Rev. A*, 70, 052716
- McElroy, D., Walsh, C., Markwick, A. J., et al. 2013, *A&A*, 550, A36
- Meijerink, R., & Spaans, M. 2005, *A&A*, 436, 397
- Nelson, R. P., & Langer, W. D. 1997, *ApJ*, 482, 796
- 1999, *ApJ*, 524, 923
- Neufeld, D. A., & Kaufman, M. J. 1993, *ApJ*, 418, 263
- Neufeld, D. A., Lepp, S., & Melnick, G. J. 1995, *ApJS*, 100, 132
- Neufeld, D. A., & Wolfire, M. G. 2009, *ApJ*, 706, 1594
- 2016, *ApJ*, 826, 183
- Omukai, K., Hosokawa, T., & Yoshida, N. 2010, *ApJ*, 722, 1793
- Ostriker, E. C., McKee, C. F., & Leroy, A. K. 2010, *ApJ*, 721, 975
- Ostriker, E. C., & Shetty, R. 2011, *ApJ*, 731, 41
- Padoan, P., Jones, B. J. T., & Nordlund, Å. P. 1997, *ApJ*, 474, 730
- Papadopoulos, P. P., Thi, W.-F., & Viti, S. 2004, *MNRAS*, 351, 147
- Papadopoulos, P. P., van der Werf, P. P., Xilouris, E. M., et al. 2012, *MNRAS*, 426, 2601
- Parvathi, V. S., Sofia, U. J., Murthy, J., & Babu, B. R. S. 2012, *ApJ*, 760, 36
- Rachford, B. L., Snow, T. P., Tumlinson, J., et al. 2002, *ApJ*, 577, 221
- Rachford, B. L., Snow, T. P., Destree, J. D., et al. 2009, *ApJS*, 180, 125
- Richings, A. J., & Schaye, J. 2016a, *MNRAS*, 460, 2297
- 2016b, *MNRAS*, 458, 270
- Richings, A. J., Schaye, J., & Oppenheimer, B. D. 2014, *MNRAS*, 440, 3349
- Röllig, M., Abel, N. P., Bell, T., et al. 2007, *A&A*, 467, 187
- Roman-Duval, J., Jackson, J. M., Heyer, M., Rathborne, J., & Simon, R. 2010, *ApJ*, 723, 492
- Saintonge, A., Kauffmann, G., Kramer, C., et al. 2011a, *MNRAS*, 415, 32
- Saintonge, A., Kauffmann, G., Wang, J., et al. 2011b, *MNRAS*, 415, 61
- Savage, B. D., & Sembach, K. R. 1996, *ARA&A*, 34, 279
- Schauer, M. M., Jefferts, S. R., Barlow, S. E., & Dunn, G. H. 1989, *The Journal of Chemical Physics*, 91
- Schroder, K., Staemmler, V., Smith, M. D., Flower, D. R., & Jaquet, R. 1991, *Journal of Physics B Atomic Molecular Physics*, 24, 2487
- Schruba, A., Leroy, A. K., Walter, F., et al. 2011, *AJ*, 142, 37
- 2012, *AJ*, 143, 138
- Shapiro, P. R., & Kang, H. 1987, *ApJ*, 318, 32
- Sheffer, Y., Rogers, M., Federman, S. R., et al. 2008, *ApJ*, 687, 1075
- Sheffer, Y., Wolfire, M. G., Hollenbach, D. J., Kaufman, M. J., & Cordier, M. 2011, *ApJ*, 741, 45
- Silva, A. L., & Viegas, S. M. 2002, *MNRAS*, 329, 135
- Sofia, U. J., Lauroesch, J. T., Meyer, D. M., & Cartledge, S. I. B. 2004, *ApJ*, 605, 272
- Sofia, U. J., Parvathi, V. S., Babu, B. R. S., & Murthy, J. 2011, *AJ*, 141, 22
- Solomon, P. M., Rivolo, A. R., Barrett, J., & Yahil, A. 1987, *ApJ*, 319, 730
- Sonnentrucker, P., Wolfire, M., Neufeld, D. A., et al. 2015, *ApJ*, 806, 49
- Stacey, G. J., Hailey-Dunsheath, S., Ferkinhoff, C., et al. 2010, *ApJ*, 724, 957
- Stancil, P. C., Schultz, D. R., Kimura, M., et al. 1999, *A&AS*, 140, 225
- Sternberg, A., Le Petit, F., Roueff, E., & Le Bourlot, J. 2014, *ApJ*, 790, 10
- Stoerzer, H., Stutzki, J., & Sternberg, A. 1996, *A&A*, 310, 592
- Tacconi, L. J., Neri, R., Genzel, R., et al. 2013, *ApJ*, 768, 74
- Taylor, C. L., Kobulnicky, H. A., & Skillman, E. D. 1998, *AJ*, 116, 2746
- Tielens, A. G. G. M., & Hollenbach, D. 1985, *ApJ*, 291, 722
- Tomida, K., Tomisaka, K., Matsumoto, T., et al. 2013, *ApJ*, 763, 6
- van Dishoeck, E. F., & Black, J. H. 1988, *ApJ*, 334, 771
- Vissapragada, S., Buzard, C. F., Miller, K. A., et al. 2016, *ApJ*, 832, 31
- Visser, R., van Dishoeck, E. F., & Black, J. H. 2009, *A&A*, 503, 323
- Vrinceanu, D., Onofrio, R., & Sadeghpour, H. R. 2014, *ApJ*, 780, 2
- Wakelam, V., Smith, I. W. M., Herbst, E., et al. 2010, *Space Sci. Rev.*, 156, 13
- Walch, S., Girichidis, P., Naab, T., et al. 2015, *MNRAS*, 454, 238
- Weingartner, J. C., & Draine, B. T. 2001a, *ApJ*, 563, 842
- 2001b, *ApJS*, 134, 263
- Weselak, T., Galazutdinov, G., Beletsky, Y., & Krelowski, J. 2009, *A&A*, 499, 783
- Weselak, T., Galazutdinov, G. A., Beletsky, Y., & Krelowski, J. 2010, *MNRAS*, 402, 1991
- Wiesenfeld, L., & Goldsmith, P. F. 2014, *ApJ*, 780, 183
- Wolfire, M. G., Hollenbach, D., & McKee, C. F. 2010, *ApJ*, 716, 1191
- Wolfire, M. G., Hollenbach, D., McKee, C. F., Tielens, A. G. G. M., & Bakes, E. L. O. 1995, *ApJ*, 443, 152
- Wolfire, M. G., Hollenbach, D., & Tielens, A. G. G. M. 1993, *ApJ*, 402, 195
- Wolfire, M. G., McKee, C. F., Hollenbach, D., & Tielens, A. G. G. M. 2003, *ApJ*, 587, 278
- Wolfire, M. G., Tielens, A. G. G. M., Hollenbach, D., & Kaufman, M. J. 2008, *ApJ*, 680, 384
- Woodall, J., Agúndez, M., Markwick-Kemper, A. J., & Millar, T. J. 2007, *A&A*, 466, 1197
- Yan, M. 1997, PhD thesis, HARVARD UNIVERSITY
- Zanchet, A., Bussery-Honvault, B., Jorfi, M., & Honvault, P. 2009, *Physical Chemistry Chemical Physics*, 11, 61826191